The Development of a Near Infrared Time Resolved Imaging System and the Assessment of the Methodology for Breast Imaging

David Jonathan Hall, B.Sc.

Thesis submitted for the degree of
Doctor of Philosophy (Ph.D.)
at the University of London

Department of Medical Physics and Bioengineering,
University College London.

September 1996

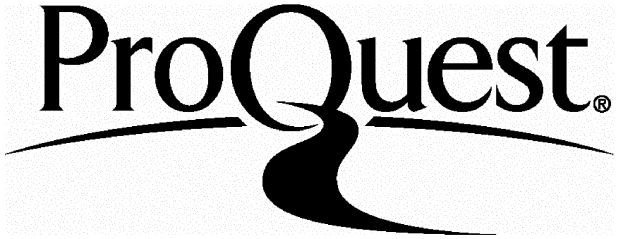

ABSTRACT

The aim of my Ph.D. research was the development and assessment of a time resolved near infrared (NIR) system for imaging through highly scattering media, with a view to its potential as a future breast imaging modality. This was motivated by the desire to produce a breast imaging system using harmless doses of NIR radiation as a more effective, less expensive and safer alternative to x-ray mammography.

The principal components of the time resolved NIR system are a picosecond pulse laser and a streak camera to record transmitted intensity as a function of time. My Ph.D. research has involved the development of an automation program to control the system, including two-dimensional translation of the object being imaged, data collection, and laser power monitoring. The implementation of the automation program increased the data acquisition rate by approximately a factor of ten. This enabled experiments to be performed which had previously been prohibited by time constraints.

Several different phantoms have been manufactured and imaged in order to assess the breast imaging potential of the approach. These have included phantoms with optical properties similar to breast tissue, edge-phantoms to evaluate the achievable spatial resolution, and phantoms with several embedded inhomogeneities of differing optical properties to evaluate the achievable contrast. Data processing software was also developed to produce images of the phantoms.

The time-gating principle has been employed to generate images which are superior to previous conventional CW transillumination methods. Further improvement in the images has been obtained by using a novel technique known as temporal extrapolation.

Overall, the research has demonstrated the success of the time resolved methodology to obtain images of breast-like phantoms. Furthermore, as a consequence of the research a clinical time resolved breast imaging system is currently being constructed at UCL.

ACKNOWLEDGEMENTS

I would particularly like to thank my supervisor, Dr. Jeremy Hebden, for his continuous encouragement and guidance throughout the research. Furthermore, I am extremely grateful to him for proof-reading my thesis. Special thanks must also be given to my colleague, Dr. Michael Firbank, for his invaluable advice on breast-like phantom manufacture. Other members of the department with whom I had very helpful discussions include Professor David Delpy and Dr. Martin Schweiger.

Finally, I would especially like to thank my family who have encouraged and supported me throughout all my student years and to whom I dedicate this thesis.

CONTENTS

CHAPTER 5

THE TIME RESOLVED NIR IMAGING SYSTEM 59

CHAPTER 6

EXPERIMENTAL STUDIES 67

LIST OF FIGURES

CHAPTER 1

INTRODUCTION

1.1 AIMS

The last decade has seen a dramatic growth in the field of biomedical optics[1,2] accompanied by significant technological advancements. One of the major objectives of this expanding discipline is the development of a new non-invasive diagnostic imaging modality using harmless doses of near infrared (NIR) radiation. The work has been motivated by a number of clinical applications, with arguably the ultimate goal being the production of a more effective, less expensive and safer alternative to x-ray mammography.[3] The main aim of my Ph.D. research was the development and assessment of a time resolved near infrared system for imaging through highly scattering media, with a view to its potential as a future breast imaging modality. This thesis presents a general introduction to the field of optical imaging followed by a description of the research that I have conducted in this area.

1.2 CLINICAL BACKGROUND

Breast cancer is the most common form of cancer to affect women in Europe and the USA, causing more than 15 000 deaths each year in the UK alone.[4] Unfortunately, the cause of breast cancer is still unknown and a means of primary prevention is not available. However, there are several factors which have been correlated with an increased risk of breast cancer development. These include a family history of breast cancer, not having a child before approximately 34 years of age, excessive fat and alcohol intake, exposure to ionising radiation and cigarette smoking, particularly in postmenopausal women.[5] The disease is known to originate in the milk-producing cells and cells lining the small milk ducts. These malignant cells then spread outside the ducts and penetrate the vessel walls of the circulatory and lymphatic systems. The malignant

tumour promotes this process by inducing its own blood supply (angiogenesis) to facilitate its survival. The malignant cells are then carried in the circulating fluids until they lodge or adhere in downstream capillary beds or lymph nodes. The cells then invade the vessel wall in an active process leaving the circulation. Once outside the circulation, the cells proliferate forming secondary tumours that repeat the process again which ultimately proves fatal.[6] The term "metastasis", coined by Joseph Claude Recaimer in 1829, is used to describe this spreading of malignant cells throughout the body that induces the secondary tumours. Treatment of the disease may involve hormone therapy, chemotherapy, lumpectomy (removal of just the primary tumour and immediate surrounding tissue), a modified or radical mastectomy, or a combination of these. A radical mastectomy involves removal of the affected breast along with the underlying pectoral muscles and the axillary lymph nodes. Radiation treatment and chemotherapy may follow the surgery to try and ensure the destruction of any stray cancer cells.[5] Unfortunately, once metastasis has occurred treatment of the disease becomes more difficult, usually limited to chemotherapy, and survival is less likely.[6] A reduction in the mortality rate thus relies on the early detection of the primary tumour before metastasis occurs. Therefore it is generally accepted that the routine breast screening of asymptomatic women could substantially improve the survivability rate. At present, x-ray mammography is the most widely used non-invasive screening technique for breast cancer.[7-10] However, it is far from infallible and there is a strong necessity for more effective, less expensive and safer alternatives.[11]

1.3 NON-INVASIVE BREAST IMAGING TECHNIQUES

1.3.1 X-RAY MAMMOGRAPHY

X-ray mammography is by far the most widely used non-invasive breast screening technique to date. The technique is based on the observation that different tissue types absorb different amounts of x-ray radiation and that x-rays are negligibly scattered by soft tissues. The former observation generates the image contrast and the latter leads to high spatial resolution. In general, tumours absorb x-rays more strongly than the surrounding healthy breast tissue since they are more dense and 40% of them contain microcalcifications.[12] In practice, the x-ray source is placed on one side of the breast and a photographic plate detects the transmitted x-rays on the other. The breast is compressed to increase image detail, decrease blurring and reduce the radiation dosage. Usually two images are taken of each breast, one from the top (supero-inferior projection) and one from the side (medio-lateral projection). The resulting two-dimensional shadow image or "mammogram" is capable of achieving a spatial resolution of approximately 0.1 mm and is widely used by clinicians to diagnose 93% of tumours.[13] However, x-ray mammography still fails to identify a few percent of tumours during routine screening and the use of highly ionising radiation has led to a perceived risk associated with the technique and its subsequent under use.[14] Although the risk from x-ray mammography is negligible, (for every million forty year old women examined, 10 will go on to develop radiation induced cancer, as opposed to 800 who will have tumours detected), the relative risk does increase in younger women due to both the reduced occurrence of natural cancer and an increased risk of radiation induced cancer.[11] Furthermore, x-ray mammography can only be repeated on the same patient at a limited frequency to stay within x-ray exposure safety levels. Therefore breast screening would clearly benefit from a technique using safe NIR radiation with improved diagnostic capabilities.

1.3.2 MAGNETIC RESONANCE IMAGING (MRI)

MRI is a relatively new imaging modality which offers high spatial resolution and has no known side effects or risks. The region of interest is placed in a magnet which causes the magnetic moment of certain nuclei to precess around the magnetic field vector, B_0. Generally, hydrogen nuclei are chosen because of the body's large water content. The angular frequency of the precession, w, known as the Larmor frequency, is dependent upon B_0 and the gyromagnetic properties of the nucleus. In equilibrium the magnetic moments of the hydrogen atoms produce a net magnetisation vector M which is parallel to B_0. By applying a short pulse of an external radiofrequency field of frequency w, whose magnetic field component is generally perpendicular to B_0, the magnetisation vector, M, can be rotated through 90 degrees into the plane perpendicular to B_0, so that M precesses around B_0 at frequency w. This rotating magnetic field can induce a radiofrequency current to flow in a detecting coil. This detected signal than decays due to two mechanisms. One is due to the dephasing of the transverse spins (characterised by the transverse relaxation time T_2) and the other being the return of the spins to the orientation parallel to B_0 (characterised by the longitudinal relaxation time T_1). These relaxation times are tissue dependent and can be measured by applying suitable sequences of RF pulses. It is also possible to produce an image of the nuclei density, generally resulting in a hydrogen density map. Clinical research trials[15] have demonstrated breast tumour detection using MRI with a spatial resolution of approximately 0.7 mm. Characterisation and enhanced detection of the tumour may also be aided by the incorporation of a paramagnetic contrast media such as Gd-DTPA,[16,17] although the technique then becomes invasive. Unfortunately, the use of MRI as a routine breast scanning method has been hindered by the exceptionally high cost associated with the technique, the large size of the equipment, and the requirement for the patient to remain motionless for approximately 30 minutes during the measurement. These factors have resulted in the lack of development of appropriate MRI breast imaging systems.

1.3.3 ULTRASOUND

Ultrasound is a technique which involves transmitting high frequency sound waves into the body and detecting the reflected signal. Sound waves are mainly reflected at the interface between body tissues of different acoustic impedance, but also within tissues due to small scale inhomogeneities. The time-delay between the transmitted and reflected sound pulses indicates the boundary distance from the source. Different tissue types can be distinguished by the intensity of the sound wave they reflect. In medical applications frequencies ranging from 1 to 10 MHz are employed and the reflected pulses are detected and used to generate an image. At present, there is no clear evidence that diagnostic doses of ultrasound produces harmful effects in humans, although there are limits to the intensity and exposure time which can be used. One procedure for breast imaging is performed whilst the patient lies on her stomach in a specially designed hospital bed with her breast immersed in a tank of water to reduce impedance mismatch.[18] The ultrasonic probe is then passed horizontally beneath the patient and the reflected wave is detected. Although ultrasound can neither detect microcalcifications nor tumours less than approximately 1 cm in diameter, it can be used to determine whether a large lump is a benign cyst or a malignant tumour. Therefore, ultrasound has limited use as a breast screening technique because detection of tumours approximately 1 cm or greater in diameter is generally too late as metastasis will have already occurred.

1.3.4 THERMOGRAPHY

Thermography involves viewing the patient with an infrared camera and interpreting variations in the temperature at the surface of the skin. In 1956 Lawson observed that the skin over a malignant tumour in the breast was slightly hotter (1-3 degrees centigrade) than the corresponding area in the unaffected breast.[19] This temperature change is determined by the heat generated from the tumour itself and by the usually associated hypervascularisation. Therefore, thermography appeared to be the ideal breast screening method because it was simple, non-invasive and cheap. However, the surface temperature pattern associated with the tumour is determined by the heat conduction

path through adjacent tissues and the arrangement of blood vessels and lymphatics which drain the area. It is therefore evident that there is only a limited capability of the technique for detection of deep tumours and there are no clear discriminating features which can uniquely define the specific nature of a tumour.[18] Therefore initial hopes for thermography were not realised and the technique is restricted to detecting tumours close to the skin surface.

1.3.5 OPTICAL IMAGING - CONVENTIONAL TRANSILLUMINATION

Optical imaging in medicine is a rapidly growing research area[1,2] and it is within this field that my Ph.D. research has been conducted. The possibility of using optical radiation for imaging arises because different tissue types have different optical characteristics.[20] Therefore optical imaging can provide information that cannot be obtained by alternative techniques and which may potentially have improved diagnostic capabilities. Furthermore, optical imaging techniques are non-invasive and employ harmless doses of optical radiation. Using optical radiation for breast cancer diagnosis was first suggested by James Ewing and Frank Adair of the Breast Clinic at Memorial Hospital in New York. Their co-worker, Max Cutler, reported the first clinical results in 1929 where he described illumination of the breast with visible light from an electric lamp and direct observation of the transmitted light by eye in a darkened room.[21] He reported a noticeable difference in the transmission of light through normal tissue compared to pathological tissue, which produced darker shadows. However, he was unable to detect any differences in the shadows cast by benign and malignant tumours. In 1972, Gros et al (referenced from Profio et al)[22] reported that they were able to distinguish benign from malignant tumours using visible light and coined the term "diaphanography" to describe the transillumination process. This improvement was achieved by removing heat from the light source by water cooling, thus permitting a higher power source to be used and hence greater transmission through the breast. Spectroscopic measurements[23] had revealed that the transmission of optical radiation through biological tissue was maximised at near infrared wavelengths where the overall tissue attenuation was a minimum. This observation led Ohlsson et al[24] to demonstrate that photographing the transilluminated breast with an infrared sensitive film

considerably improved their ability to identify benign from malignant tumours. In 1982, Carlsen[25] modified this technique by eliminating all illumination wavelengths except for visible red and near infrared and viewing the breast in real-time with an infrared sensitive vidicon tube. He called this process "light scanning" and reported high accuracy in detecting breast cancers of all sizes. However, many other researchers have not been able to achieve these favourable results. Several clinical trials have compared light scanning and x-ray mammography and concluded that light scanning does not have adequate sensitivity or specificity to be used for breast screening. Light scanning was found to be particularly poor at identifying small, nonpalpable and deep tumours.[26-30]

The optical imaging techniques described above have subsequently been classified as conventional transillumination techniques and are characterised by the use of a continuous wave (CW) light source to illuminate the breast and detection of the transmitted light intensity. Unfortunately, initial hopes for conventional transillumination as a breast imaging technique were not realised as it suffers from the highly scattering optical properties of breast tissue. The presence in the transmission image of highly scattered photons which have travelled unknown paths through the tissue severely limits the achievable spatial resolution. In practice, conventional transillumination of the breast has a limiting spatial resolution of approximately 2 cm and is not adequate for a breast screening method.[27] The results obtained from conventional transillumination of the breast have shown that large, well-developed tumours generally appear darker than the surrounding healthy tissue indicating greater attenuation. Oxygenated haemoglobin has been conjectured as the origin of this contrast, since tumours are usually hypervascular.[31] However, since perfectly healthy vascular tissue can appear similarly dark in a conventional transillumination image, it is likely that in order to identify tumours an effective system may have to rely as much upon detecting morphological differences as upon differences in contrast, and thus the necessity for better spatial resolution. Fortunately, the advent of new optical technologies during the past ten years has provoked an interest in new techniques to improve the spatial resolution of images obtained through highly scattering media. A more detailed discussion of the various optical imaging techniques currently being investigated is given in Chapter 4.

CHAPTER 2

ABSORPTION AND SCATTERING OF LIGHT

In order to develop an optical imaging technique it is essential to understand the interaction of light and tissue. This chapter describes the basic optical interactions of absorption and scattering, and summarises the measured values of their associated coefficients for breast tissue.

2.1 ABSORPTION

2.1.1 LAMBERT-BOUGUER LAW

In 1729 Bouguer[32-34] derived the first relationship between the attenuation of light and the thickness of a material. Lambert later expressed Bouguer's relationship mathematically.[34,35] This is commonly called the Lambert-Bouguer law and states that the fraction, dI/I, of collimated radiation transmitted through a layer of purely absorbing medium depends exclusively on the layer thickness, dl, and a material constant, μ_a, called the absorption coefficient. This may be expressed as $dI/I = -\mu_a dl$. Hence for an incident intensity I_0, the transmitted intensity I after a distance l is given by

$$I = I_0 \, e^{-\mu_a l} \quad . \tag{2.1}$$

The reciprocal of the absorption coefficient is known as the absorption length, and represents the mean free path travelled by a photon before being absorbed.[36]

Eq.(2.1) can also be expressed in base 10:

$$I = I_0 \, 10^{-\kappa l} \quad . \tag{2.2}$$

The constant κ is called the extinction coefficient. By taking the logarithm of Eq.(2.2)

the absorbance A_B can be defined as

$$A_B = \log_{10}\left[\frac{I_0}{I}\right] = \kappa l \quad . \tag{2.3}$$

2.1.2 BEER-LAMBERT LAW

In 1852 Beer[37,38] derived a similar absorption relationship which states that the absorption coefficient is proportional to the concentration of the absorber:

$$\mu_a = \alpha C \quad . \tag{2.4}$$

The constant of proportionality, α, is called the specific absorption coefficient. By combining Eq.(2.1) and Eq.(2.4) we obtain the Beer-Lambert law:

$$I = I_0\, e^{-\alpha c l} \quad . \tag{2.5}$$

Eq.(2.5) can also be expressed in base 10:

$$I = I_0\, 10^{-\varepsilon c l} \quad , \tag{2.6}$$

where ε is defined as the specific extinction coefficient.

For a non-absorbing solution containing a mixture of absorbing compounds the individual extinction coefficients are additive. Therefore the total absorbance is given by

$$\begin{aligned} A_B &= (\kappa_1 + \kappa_2 + \ldots \kappa_n) l \\ &= (\varepsilon_1 c_1 + \varepsilon_2 c_2 + \ldots \varepsilon_n c_n) l \end{aligned} \quad . \tag{2.7}$$

The equations described above must be used with caution as they are only valid for non-scattering media.

2.2 SCATTERING

2.2.1 INTRODUCTION TO SCATTERING THEORY

The principal interaction of optical radiation in biological tissue is scatter. There are two main types of scattering which are known as inelastic and elastic scattering. For inelastic scattering the scattered photon has a lower energy than the incident photon due to energy absorption by the absorbing particle. The re-emission of the scattered photon can be either instantaneous or delayed depending on the exact nature of the scattering mechanism. For elastic scattering the energy of the scattered photon is the same as the incident wave, i.e. there is no energy loss. In biological tissue, at NIR wavelengths, the main type of scattering is elastic. By analogy with the absorption coefficient we can define another optical parameter, the scattering coefficient,[34] μ_s:

$$I = I_0 \, e^{-\mu_s l} \quad , \tag{2.8}$$

where I is the intensity of the transmitted unscattered light in a non-absorbing sample. The reciprocal of the scattering coefficient, known as the scattering length, is the mean free path of a photon between consecutive scatters. It is useful to define the optical thickness of a medium as its physical thickness, d, expressed in units of the scattering length. Therefore optical thickness is a dimensionless quantity equal to $\mu_s d$. A thin, low scattering media will have a low optical thickness, whereas a thick, highly scattering media will have a high optical thickness.

In practice both absorption and scattering occur in tissues and we can define a total attenuation coefficient μ_t as follows:

$$I = I_o \, e^{-\mu_t l} \quad , \tag{2.9}$$

where $\mu_t = \mu_a + \mu_s$ and I is the intensity of the transmitted unscattered light.

The reciprocal of the total attenuation coefficient known as the attenuation length is the mean free path travelled by a photon before encountering either an absorption or

scattering event.

The attenuation, A, (units of Optical Density (OD)), is simply defined as the log to base 10 of the ratio of the input and transmitted light intensities.[39] The transmittance T is simply the ratio of the transmitted light I, to the input light I_0. Thus:

$$A = \log_{10}\left(\frac{I_0}{I}\right) = \log_{10}\left(\frac{1}{T}\right) \quad . \tag{2.10}$$

If I represents the intensity of the unscattered transmitted light, then attenuation may be expressed as

$$A = \mu_t \, l \, \log_{10} e \quad . \tag{2.11}$$

Note that the attenuation due to an absorbing, non-scattering media simply reduces to the total absorbance as defined in Eq.(2.7).

The development of single scattering mechanisms is essential if one is to understand the interaction of light with tissue. In the scattering process[36] a photon propagating in direction Ω' is scattered by a particle into direction Ω. In general the new direction of the particle, Ω, does not occur with equal probability and can be described by the differential scattering coefficient, $d\mu_s(\Omega' \rightarrow \Omega)$. The total scattering coefficient is given by the integral over the solid angle,

$$\mu_s = \int_{4\pi} d\mu_s(\Omega' \rightarrow \Omega) d\Omega \quad . \tag{2.12}$$

It is customary to assume that the differential scattering coefficient is independent of the incident photon direction so that it becomes $d\mu_s(\Omega'.\Omega)$. In other words, the differential scattering coefficient will only depend on the scattering angle, θ, between the unscattered and scattered light. This assumption is probably valid for randomly organised soft tissues but may not be true for highly structured tissues such as muscle.

2.2.2 PHASE FUNCTION

In radiative transfer theory a normalised version of the differential scattering coefficient called the phase function is used. This probability density function, $f(\Omega'.\Omega)$, is defined as

$$f(\Omega'.\Omega) = f(\cos(\theta)) = \frac{1}{\mu_s} d\mu_s(\Omega'.\Omega) \quad , \tag{2.13}$$

so that

$$\int_{4\pi} f(\Omega'.\Omega) d\Omega = 1 \quad . \tag{2.14}$$

The mean cosine of the scattering angle θ, (sometimes called the anisotropy factor) is the first moment of $f(\Omega'.\Omega)$ and is denoted by g. Note that for isotropic scattering $g = 0$ and that $g \rightarrow 1$ as the scattering becomes forward peaked. For biological tissues at NIR wavelengths the g-value has been reported[20] to range from 0.69 to 0.99 implying that the scattering is highly forward peaked.

This description of the phase function can be extended to include higher moments of $f(\Omega'.\Omega)$ by expanding the phase function in Legendre polynomials.[40] A commonly used analytic expression for the phase function when modelling low absorbing, highly scattering media is the Henyey-Greenstein[41] phase function. This function gives a good approximation to the predictions of Mie theory (see Sec.(2.2.5)) and its coefficients in the Legendre polynomial expansion are simple functions of g.

Alternatively, the phase function of a sample can be measured experimentally using a goniometer turntable,[42] or a diaphragm technique[43] when the scattering is highly forward peaked.

2.2.3 TRANSPORT COEFFICIENTS

In diffusion theory, where isotropic scattering is assumed, it is useful to define a quantity μ_s', the transport scattering coefficient:

$$\mu_s' = \mu_s (1-g) \quad . \tag{2.15}$$

The transport scattering coefficient is therefore a scaled version of the scattering coefficient which enables anisotropic scattering to be treated as "effectively" isotropic scattering for diffusion theory. Note that for isotropic scattering, where g = 0, μ_s' is equal to μ_s.

The reciprocal of the transport scattering coefficient, known as the transport scattering length, is the path travelled by a collimated beam of light before becoming "effectively" isotropic.

It is possible to also define[36] a transport attenuation coefficient, μ_{tr} ,

$$\mu_{tr} = \mu_a + \mu_s (1-g) = \mu_a + \mu_s' \quad . \tag{2.16}$$

The reciprocal of the transport attenuation coefficient, known as the transport attenuation length, is the mean free distance travelled by a photon before becoming either absorbed or "effectively" isotropically scattered. The transport attenuation length can therefore be considered as the mean free path of a photon in diffusion theory.

2.2.4 RAYLEIGH THEORY

Rayleigh theory[44] describes the scattering of light by particles which are much smaller than the wavelength of the incident light. The theory can be derived from dimensional analysis by considering the volume V of the particle, the distance r at which observations are made and the wavelength λ of the incident light I_i. The intensity of the scattered light I_s is given as,

$$I_s \propto I_i \frac{V^2}{r^2 \lambda^4} \quad . \tag{2.17}$$

However, Rayleigh scattering is of limited relevance to optical imaging of biological tissue as it is restricted to very small particle sizes.

2.2.5 MIE THEORY

Attributed to Gustav Mie (1908), this theory provides exact solutions of the Maxwell equations for the scattering of a plane electromagnetic wave by an isotropic homogeneous spherical particle of arbitrary size.[44] For very small particle sizes the Mie solutions converge towards the Rayleigh equations. At large particle sizes the scattering characteristic becomes highly non-isotropic and strongly forward peaked. Additionally, the angular intensity distribution shows overlying oscillations as a result of interference effects. The ability of Mie theory to handle particles of arbitrary size has led to its widespread use in the field of light scattering in tissue.

2.3 ABSORPTION AND SCATTERING PROPERTIES OF TISSUE

2.3.1 ABSORPTION BY TISSUE

Absorption of light in biological tissues is dominated by several principal chromophores. The description given here will be limited to water, lipids, and haemoglobin.

Water

The primary component of most soft tissues is water, although it only makes up 21% of adipose tissue[45] which is a main constituent of the female breast. The absorption spectrum of water,[46] Fig.(2.1), is therefore significant when considering the use of NIR for breast imaging. The absorption spectrum has a minimum at about 500 nm forming an effective "transmission water window" from UV to near infrared (200 nm to 1000 nm) where the absorption coefficient is low.

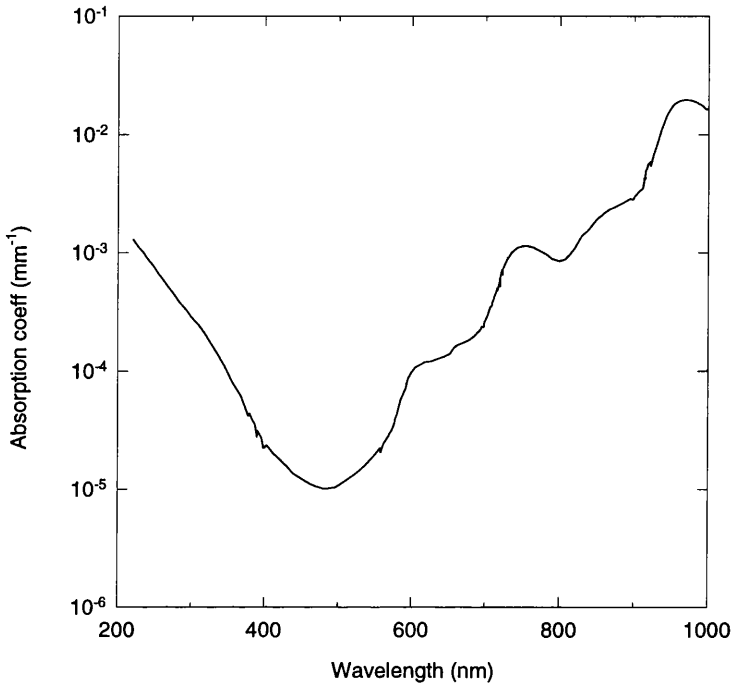

Figure 2.1 *The absorption spectrum of water.*

Lipids

Absorption spectra of human lipids are uncommon in the literature, although the absorption spectrum of pork fat has been measured by Conway et al[47] and is given in Fig.(2.2). There is an effective "transmission lipid window" in the range of 600-900 nm where the absorption is low. For the breast, which is mainly composed of adipose tissue, itself consisting of 75% lipid,[45] the NIR absorption by lipids must be considered.

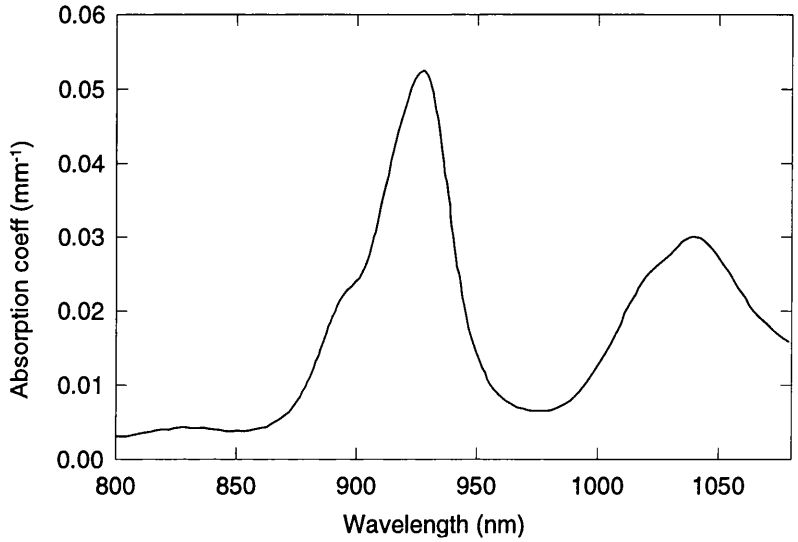

Figure 2.2 *The absorption spectrum of pork fat.*

Haemoglobin

Haemoglobin is found in red blood cells and is responsible for oxygen transport in blood. Its absorption spectrum[39] depends upon its oxygenation state, either oxygenated haemoglobin (HbO_2) or deoxygenated haemoglobin (Hb). From Fig.(2.3) it can be seen that both states are highly absorbing below 600 nm, although there is a drop in absorption coefficients above 700 nm. Combined with the previous chromophores, light transmission through thick tissue is limited to between 700 nm and 1000 nm, i.e. NIR radiation. The difference in the absorption spectra between the oxygenated and deoxygenated states is already being utilised in the closely related field of near infrared spectroscopy (NIRS) to evaluate tissue oxygenation in the brain.[48-50] Due to the generally high vascularisation of tumours, absorption by haemoglobin may also be a useful indicator in breast cancer diagnosis.

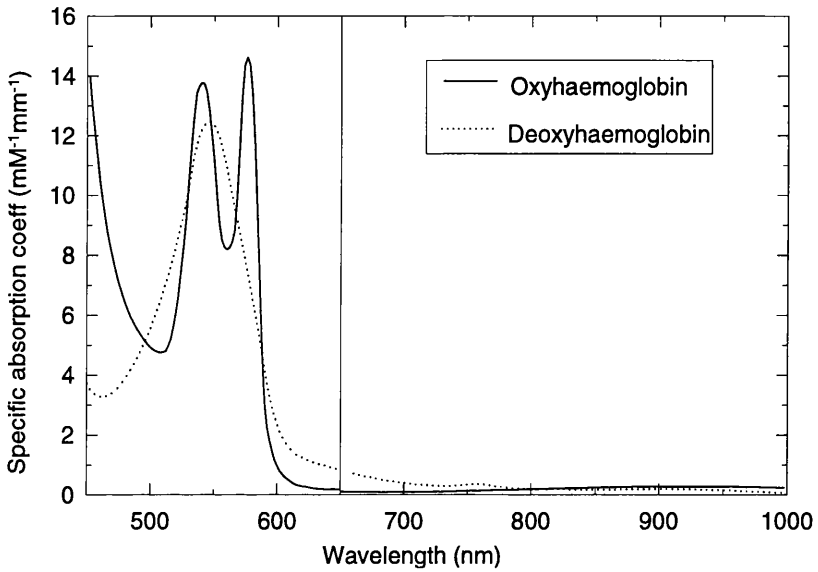

Figure 2.3 *The absorption spectra of haemoglobin in both oxygenated and deoxygenated states.*

Additional chromophores affecting tissue absorption include myoglobin, cytochrome and other haem proteins, but have negligible effect on the overall tissue spectra.

The previous absorption spectra are obtained via attenuation measurements of the pure chromophores and the application of the Beer-Lambert law to calculate μ_a. The basic assumption made is that the attenuation by the pure chromophores are absorption dominated and that scattering is negligible. These pure absorption spectra are widely used in NIRS techniques which are generally concerned with measuring changes in the optical properties of large tissue volumes.

Unfortunately, the attenuation of light by biological tissue is scatter dominated and so application of the Beer-Lambert law is not adequate to calculate their absorption coefficients. However, there are more sophisticated techniques employed in NIRS which attempt to account for scatter.[51] The range of absorption coefficients which have been reported for breast tissue are stated in Table (2.1).

2.3.2 SCATTERING BY TISSUE

Light scattering in tissue is due to the variations in the refractive index of its components. On the large scale this is due to overall changes in refractive index at the boundaries between one type of tissue and another. On the smaller scale, it is caused by small variations in refractive index within cells and the extracellular fluid. Scattering in tissue is therefore a highly complex problem due to its intricate structure. The variation in refractive index in biological tissues ranges from 1.33 (water) to 1.55 (fat). However, in many mathematical light transport models the internal refraction is often omitted for simplicity and a uniform refractive index is assumed. When modelling light transport in tissue it is not essential to fully incorporate the origin of the scattering, so long as its overall effect can be represented.

The scattering coefficient of a sample can be obtained directly with simple collimated attenuation measurements. However, thin samples must be used so that single scattering of light can be assumed. Eq.(2.9) can then be solved, employing *a priori* information of μ_a, to obtain μ_s. Unfortunately, the optical properties of *in vivo* tissue can be radically altered during the preparation of thin, *in vitro* tissue samples. Therefore, for thick, multiply scattering samples, such as the breast, the more sophisticated techniques of NIRS are employed.[51] The range of transport scattering coefficients which have been reported for breast tissue are presented in Table (2.1).

2.3.3 OPTICAL PROPERTIES OF BREAST TISSUE

The following table summarizes the ranges of optical properties that have been reported in the literature for breast tissue, both *in vivo* and *in vitro*, for wavelengths ranging from 700 nm to 900 nm.

Breast Tissue Type	μ_a (mm^{-1})	μ_s' (mm^{-1})	g-value
Healthy (*In Vitro*)	0.005 - 0.075	0.53 - 1.42	0.92 - 0.985
Healthy (*In Vivo*)	0.0017 - 0.0078	0.63 - 1.22	Not available
Carcinoma (*In Vitro*)	0.002 - 0.05	0.5 - 1.8	0.88 - 0.985

Table 2.1 *The reported optical properties of breast tissue.*

The study by Peters et al[52] on various *in vitro* healthy breast tissues suggested that at NIR wavelengths (700 nm to 900 nm) the optical coefficients are typically in the range $\mu_s' = 0.53 - 1.42\ mm^{-1}$, $\mu_a = 0.022 - 0.075\ mm^{-1}$ and $g = 0.945 - 0.985$. Another study of *in vitro* healthy breast tissues by Key et al[53] reported $\mu_s' = 1.2 - 1.3\ mm^{-1}$ at 700 nm, $\mu_a = 0.01 - 0.05\ mm^{-1}$ at 850 nm (assuming $\mu_s' = 0.75\ mm^{-1}$) and $g = 0.92 - 0.95$ at 700 nm. A further study by Troy et al[54] reported $\mu_s' = 0.73 - 0.97$ and $\mu_a = 0.005 - 0.018\ mm^{-1}$ over the wavelength range 749 - 836 nm. However, because of the possible chemical and structural changes during the preparation of these *in vitro* samples, there is naturally some concern that such measurements may not be representative of living breast tissues. Recently, however, estimates from *in vivo* measurements have become available. A study of the mean optical properties from six volunteers by Mitic et al[55] confirm a similar range in μ_s' at 800 nm of 0.72 - 1.22 mm^{-1}, but suggest a significantly lower absorption coefficient in the range $\mu_a = 0.0017 - 0.0032\ mm^{-1}$. Meanwhile a smaller study by Suzuki et al,[56] provide values which suggest a strong dependence on age. Two volunteers, aged 30 and 58, yielded values of $\mu_s' = 1.13$ and $0.76\ mm^{-1}$ and $\mu_a = 0.0068$ and $0.0028\ mm^{-1}$ respectively at a wavelength of 753 nm. Another study by Suzuki et al[57] on thirty Japanese women reported $\mu_s' = 0.63 - 1.08\ mm^{-1}$ and $\mu_a = 0.0024 - 0.0078$ at 753 nm. As the broad variation in published values illustrates, every human breast cannot be simply characterised by a single set of optical coefficients. First, breast tissue varies depending on the age of the women. Second, the breast can be highly

inhomogeneous, containing distinct regions of adipose, glandular and fibrocystic tissue etc.

Obtaining values for the optical properties of breast tumours poses an even greater problem. There are many manifestations of breast disease and a tumour may have optical characteristics which vary during its development. Diseased tissues generally show some wavelength dependent differences in optical characteristics compared to healthy tissues. However, the study by Peters et al[52] reported optical properties for *in vitro* carcinoma (μ_s' = 0.89 -1.18 mm^{-1}, μ_a = 0.045 - 0.050 and g = 0.945 - 0.985 for a wavelength range 700-900 nm) which fall within the range of values stated for *in vitro* healthy tissues. Whereas, the study by Key et al[53] have reported carcinoma values of μ_s' = 1.8 mm^{-1} (g = 0.88) at 700 nm which is higher than healthy tissue values, but μ_a = 0.005 and 0.015 mm^{-1} at 850 nm (assuming μ_s' = 0.75 mm^{-1}) which falls within the range of healthy tissue values. Meanwhile, the study by Troy et al[54] yielded carcinoma values of μ_s' = 0.5 - 1.3 mm^{-1} and μ_a = 0.002 - 0.026 mm^{-1} over the wavelength range 749 - 836 nm. They reported that the study indicated no overall statistical difference in the optical properties of healthy or diseased breast tissue. However, for a given patient the values for μ_s' were generally greater in the diseased tissue than the healthy tissue. Although for a given patient the values for μ_a were still similar, they suggest that their *in vitro* values for diseased tissue may underestimate the *in vivo* values because of the blood drainage that occurs during excision. Unfortunately, there are no reliable estimates of tumour properties obtained from *in vivo* measurements to date.

This Ph.D. research has employed optical coefficients for breast tissue within the ranges stated in Table (2.1). It is encouraging for optical imaging that the absorption coefficients for the more realistic *in vivo* measurements are significantly lower than previous *in vitro* measurements, as this implies greater light transmission through the breast. However, more optical measurements on *in vivo* breast tissues are clearly required in order to improve current estimates of their optical coefficients.

CHAPTER 3

LIGHT PROPAGATION MODELS

This chapter outlines the principal models of photon migration that have been used to describe the propagation of optical radiation in tissue.

3.1 MAXWELL'S EQUATIONS

Light propagation in tissue can, in principle, be described using electromagnetic theory.[36] Tissue could be considered as a random medium whose permittivity $\varepsilon(r)$ fluctuates with position about some mean value $\varepsilon_{(1)}$ as follows:

$$\varepsilon(r) = \varepsilon_{(1)} + \varepsilon_{(2)}(r) \quad , \tag{3.1}$$

where $\varepsilon_{(2)}(r)$ is governed by a random process whose characteristics (ie variance) are known. The statistical behaviour of the electric-field can then be described using Maxwell's equations. While physically appealing, this formalism has yet to find application in tissue optics because of its complexity, the lack of readily applied solutions, and the lack of information about $\varepsilon_{(2)}(r)$.

3.2 TRANSPORT THEORY

Most of the recent advancements in describing the nature of light in tissue are based upon transport theory.[36] The main approach of transport theory is to ignore the wave nature of light and simply consider the flow of energy within the medium.

The general differential equation in transport theory is known as the Boltzmann or the radiative transfer equation, Eq.(3.2). For a photon source q, the photon intensity I (units of photons m^{-3} sr^{-1}), at position r and time t in direction Ω is given by,

$$\frac{1}{c}\frac{d}{dt}I(r,t,\Omega) + \Omega\nabla I(r,t,\Omega) + \mu_t I(r,t,\Omega) = \mu_s \int_{4\pi} f(\Omega',\Omega) I(r,t,\Omega')d^2\Omega' + q(r,t,\Omega) \quad (3.2)$$

Eq.(3.2) can be considered as an energy balance equation describing the flow of photons, with velocity c, in a given volume element. The first term represents the rate of change of the intensity with time; the second term is the net change due to energy flow; the third term is the intensity lost due to absorption and scatter; the fourth term is the gain in intensity from photons scattered into direction Ω from all other directions; and the last term is the source term.

Note that for this radiative transfer equation the optical properties of the media are assumed to be both spatially and temporally independent which is only true for homogeneous media. For inhomogeneous media it is necessary to include spatial and temporal dependence terms for the media properties which greatly complicates the mathematics.

Unfortunately a general solution of the radiative transfer equation has not yet been obtained and so in practice approximate solutions or numerical methods must be used.

3.3 APPROXIMATE SOLUTIONS TO TRANSPORT THEORY

3.3.1 DISCRETE ORDINATE METHODS

The discrete ordinate methods[36] enable the time independent radiative transfer equation to be converted to a series of linear algebraic equations suitable for numeric solution. This is achieved by representing the intensity by its value at discrete values of the independent variables. The operations of differentiation and integration are replaced by their discrete counterparts, finite differences and summation. This set of equations are known as the S_N equations and this approach has also been called the N-flux method.

2-Flux model

Kubelka and Munk[36,58,59] formulated a basic 2-flux model which considers the forward diffusive flux F, and the reverse diffusive flux R propagating in an infinite slab of thickness d. It is possible to derive expressions for the total diffusive reflectance, R_{td}, and the total diffusive transmittance, T_{td}, as,

$$R_{td} = \frac{R(x=d)}{I_0} = \frac{\sinh(bSd)}{a\,\sinh(bSd) + b\,\cosh(bSd)}$$

$$T_{td} = \frac{F(x=0)}{I_0} = \frac{b}{a\,\sinh(bSd) + b\,\cosh(bSd)} \quad , \tag{3.3}$$

where a and b are defined as

$$a = \frac{S + K}{S} \quad , \quad b = (a^2-1)^{\frac{1}{2}} \quad , \tag{3.4}$$

and x = 0 at the unilluminated face of the slab, I_0 is the incident forward flux, and S and K are the Kubelka Munk scattering and absorption coefficients respectively. Therefore by the direct measurement of R_{td} and T_{td} it is possible to calculate S and K. However, S and K are not directly equivalent to μ_s and μ_a and no simple general relationship exists. Furthermore, some assumptions made in Kubelka Munk (KM) theory are generally unrealistic which results in an inappropriate light propagation model. Various modifications have been applied to KM theory to incorporate the effects of collimated beams, anisotropic scatter and reflections at the slab boundaries. These modified KM theories all reduce to a simple relationship between S and K and μ_s and μ_a for the case when $\mu_a << (1-g)\,\mu_s$ as given by

$$K = 2\mu_a \quad , \quad S = \frac{3}{4}(1-g)\mu_s \quad . \tag{3.5}$$

However, as absorption increases the radiance becomes more anisotropic and a 2-flux model may be inadequate. Therefore, several researchers[60,61] have advocated the use of more complex higher flux models which should give better predictions of R_{td} and T_{td}.

3.3.2 FUNCTIONAL EXPANSION METHODS

An alternative to discrete ordinate methods, where a number of discrete directions of the intensity are considered, are functional expansion methods where the angular dependence of the intensity may be approximated by a finite series expansion of orthogonal functions.

To solve the time dependent radiative transfer equation one can use spherical harmonics to expand the intensity, source and phase functions in Legendre polynomials. This expansion, described in more detail by Kaltenbach and Kaschke,[40] leads to a set of coupled linear differential equations, known as the Boltzmann Hierarchy, which is completely equivalent to the Boltzmann equation. Therefore the Boltzmann Hierarchy is, without further assumptions, not any simpler to solve than the Boltzmann equation itself. This is evident from the first two equations of the Boltzmann Hierarchy below:

$$\frac{1}{c}\frac{d}{dt}\Phi(r,t) + \mu_a\Phi(r,t) + \frac{1}{c}\nabla .\ J(r,t) = q_0(r,t) \quad , \tag{3.6}$$

$$\frac{1}{c}\frac{d}{dt}J(r,t) + \frac{J(r,t)}{3D} + \frac{c}{3}\nabla\Phi(r,t) + \frac{1}{c}\nabla .T_0(r,t) = q_1(r,t) \quad . \tag{3.7}$$

The zeroth moment of the intensity, $\Phi(r,t)$, is commonly called the photon density and has units of photons m^{-3}. The first moment of the intensity, $J(r,t)$, is commonly called the photon current density, and has units of photons $m^{-2}s^{-1}$. The second moment of the intensity, $T_0(r,t)$, has no direct physical meaning and has units of photons $m^{-1}s^{-2}$. Note that these first two equations cannot be solved directly as Eq.(3.6) for $\Phi(r,t)$ contains the $J(r,t)$ term and similarly Eq.(3.7) for $J(r,t)$ contains the $T_0(r,t)$ term.

The parameter D is known as the diffusion coefficient, and defined as

$$D = \frac{1}{3[\mu_a + (1 - g)\mu_s]} = \frac{1}{3\mu_{tr}} \quad . \tag{3.8}$$

It is worth noting that the diffusion coefficient, equal to one third of the transport attenuation pathlength, increases as g tends from zero to 1. In other words, as the phase function becomes more forward peaked, (g tends to 1), the diffusion coefficient increases.

The advantage of this Boltzmann Hierarchy is that it is now easier to define approximations and hence acquire approximate solutions to the Boltzmann equation .

The Diffusion approximation

The basic assumption in the diffusion approximation is that the photon current density is proportional to the gradient of the photon density as follows:

$$J(r,t) = constant.\nabla\Phi(r,t) \quad . \tag{3.9}$$

This approximation is only considered to be valid if r is not near boundaries or sources and the media is scatter dominated ($\mu_a << (1-g)\mu_s$).

By comparing Eq.(3.6), Eq.(3.7) and Eq.(3.9), the Boltzmann Hierarchy equations are therefore reduced to

$$\frac{1}{c}\frac{d}{dt}\Phi(r,t) + \mu_a\Phi(r,t) - D\nabla^2\Phi(r,t) = q_o(r,t) \quad , \tag{3.10}$$

and

$$J(r,t) = - Dc\nabla\Phi(r,t) \quad . \tag{3.11}$$

Eq.(3.11) is Fick's law for photon diffusion and so it is valid to refer to Eq.(3.10) as the time dependent diffusion equation. Note that the diffusion approximation is only valid for an isotropic source, q_0, and that no account is made for anisotropic sources. However, it is possible to incorporate an anisotropic source term into the diffusion equation under certain boundary conditions.

Higher order approximations

The diffusion approximation effectively truncates the Boltzmann Hierarchy to only the first two equations. By applying less severe assumptions to the Boltzmann Hierarchy it is possible to include higher order equations. However, as more of the Boltzmann Hierarchy equations are included the mathematics becomes more complicated.

3.4 SOLUTIONS OF THE DIFFUSION EQUATION

3.4.1 TIME INDEPENDENT

The solution of the time independent diffusion equation,[49] obtained by neglecting the first term in Eq.(3.10), for the case of an isotropic point source in an infinite medium is the Green's function as follows:

$$\Phi(r) = \frac{(2\pi)^{-\frac{3}{2}}}{rcD} \exp\left(-\left(\frac{\mu_a}{D}\right)^{\frac{1}{2}} r\right) \quad . \tag{3.12}$$

Therefore the diffusion equation predicts an exponential fall-off of $\Phi(r)$ away from the isotropic point source. Thus, it is useful to define an effective attenuation coefficient,[62] μ_{eff}, given by

$$\mu_{eff} = \left(\frac{\mu_a}{D}\right)^{\frac{1}{2}} = (3\mu_a(\mu_a + \mu_s'))^{\frac{1}{2}} \quad . \tag{3.13}$$

The reciprocal of the effective attenuation coefficient is sometimes known as the diffusion length. The time independent solution of the diffusion equation is particularly useful in an NIRS technique known as Spatially Resolved Spectroscopy.[63]

3.4.2 TIME DEPENDENT

The solution of the diffusion equation[64] for the case of an infinitely short pulse from an isotropic point source in an infinite medium is the Green's function as follows:

$$\Phi(r,t) = c(4\pi Dct)^{-\frac{3}{2}} \exp\left(-\frac{r^2}{4Dct} - \mu_a ct\right) \quad . \tag{3.14}$$

Semi-infinite slab geometry

The diffusion equation has been solved for various simple geometries.[65] For laboratory experiments involving phantoms, and ultimately for imaging the compressed human breast, the geometry will be approximated to a semi-infinite slab illuminated on the surface by a collimated laser source. By making some further assumptions, the Green's Function, Eq.(3.14), can be used to solve the diffusion equation for this geometry.[64] First, it is assumed that all the incident photons from the collimated laser pulse create an "effective" isotropic photon source at a depth z_0 below the slab surface, where z_0 equals the transport scattering length, $(\mu_s')^{-1}$. Second, an assumption is made that the photon density at both surfaces of the slab is zero. It is by no means clear that this is an appropriate assumption to make, however it does simplify the mathematics considerably. This boundary condition can be stated in cylindrical co-ordinates as follows,

$$\begin{aligned} \Phi(\rho,0,t) &= 0 \\ \Phi(\rho,d,t) &= 0 \end{aligned} \quad , \tag{3.15}$$

where d is the thickness of the slab and ρ is the distance from the optical axis on the surface of the slab. The boundary condition can be met by adding an infinite series of dipole photon sources which is known as the mirror charge method.[64] The time dependent distribution of the photon current density, T(ρ,r,t), detected at a distance ρ from the optical axis on the surface of a semi-infinite homogeneous slab of thickness d when illuminated by an infinitely short pulse of light on the opposite surface can then be derived [64,65] and is given by,

$$T(\rho,d,t) = (4\pi Dc)^{-\frac{3}{2}} t^{-\frac{5}{2}} \exp(-\mu_a ct)\ \exp\left(-\frac{\rho^2}{4Dct}\right) Q(d,t) \quad , \qquad \textbf{(3.16)}$$

where Q(d,t) is the dipole source term given by

$$Q(d,t) = \sum_{n=1,\ k=2n-1}^{n=\infty} \left[(kd - z_0)\exp\left(-\frac{(kd - z_0)^2}{4Dct}\right) - (kd + z_0)\exp\left(\frac{-(kd + z_0)^2}{4Dct}\right)\right] . \qquad \textbf{(3.17)}$$

The quantity T(ρ,r,t) is essentially equivalent to that which is measured by a physical detector and is commonly referred to as the transmitted intensity.

Several authors have used a more complex approach which assumes that the photon density falls to zero at an extrapolated boundary beyond the physical boundary by considering the impedance mismatch at the physical boundary.[66,67]

As mentioned earlier, the diffusion approximation may only be considered valid for cases where $\mu_a << (1-g)\mu_s$ and the detector is far from sources and boundaries. The first condition is generally true for soft tissues. However, the second condition is violated in calculating the transmitted intensity at the slab surface, although comparison with Monte Carlo simulations[64] have shown that accurate estimates of the relative, rather than the absolute, transmitted intensity can be obtained.

The incorporation of inhomogeneous regions into transport theory involves more complicated mathematics and at present analytical solutions only exist for a few simple cases such as for point-like absorbers.[68,69] To model light propagation in more complex inhomogeneous media there are several numerical methods available which are described below.

3.5 NUMERICAL METHODS

3.5.1 MONTE CARLO METHOD

The term Monte Carlo refers to numerical evaluations or simulations based on random sampling from appropriate probability distributions.[36] The two most common applications are particle transport simulation and numerical integration. While numerical integration could be used to evaluate the fourth term in the radiative transfer equation for both homogeneous and inhomogeneous media, particle simulations represent the great majority of Monte Carlo applications in transport theory, even though they do not actually give a direct solution to the radiative transfer equation.

In its simplest form, known as analog Monte Carlo particle simulation, the photons are injected one by one into the medium and their history is traced until they are either absorbed or permanently scattered out of the medium.

Parameters such as the pathlength between interactions and the scattering angle are randomly sampled from probability distributions based on the known physics of the problem and useful quantities, such as the absorbed energy, are stored at desired locations. The parameters required for the model are identical to those used in the radiative transfer equation, namely μ_a, μ_s and the scattering phase function (often a Henyey-Greenstein approximation is used). It is also possible to calculate quantities such as the temporally resolved transmitted intensity and reflected intensity by keeping track of the total pathlengths of photon trajectories.

This method has the advantages of being conceptually simple and allows direct handling of complex geometries, optical inhomogeneities and variations in refractive index. The significant disadvantage of this method is that it is extremely computationally expensive and the accuracy of the useful quantities only increases with the square root of the number of photon histories. Techniques to improve the accuracy of Monte Carlo simulations, for a given computation time, are known as variance reduction methods.[36] However, these should be applied with caution and initially checked against analog

Monte Carlo results.

A particular variance reduction method suited to highly scattering media is survival weighting. In this method, the photons are never totally absorbed, but rather are transported through the media with an associated weight. At each interaction a fraction, μ_a / μ_t , of a photons weight represents deposited energy while the remaining fraction, μ_s / μ_t , is the factor by which the photons weight is reduced.

Another variance reduction method generally used in conjunction with survival weighting is known as Russian roulette. It involves random sampling that terminates a low weight photon with a probability 1-v, where ($0<v<1$), so that the photon survival probability of v is accompanied by a compensating weight increase factor of v^{-1}.

Although variation reduction techniques reduce the computation time, Monte Carlo is still the most computationally expensive of all light propagation modelling methods. Therefore faster techniques, such as those incorporating diffusion theory, despite their approximations, are the currently preferred methods used in practical imaging experiments.

3.5.2 FINITE ELEMENT METHOD (FEM)

FEM is a numerical approach which may be used to describe light propagation in inhomogeneous media. It involves dividing the media into a large number of smaller volumes or elements which each have a single set of optical properties. This arrangement can also be considered as a mesh consisting of many nodes. The photon density at each individual node can be obtained by finding a solution to the diffusion approximation for all the nodes simultaneously via complex matrix manipulation. For each element a matrix equation is obtained for its unknown node values. These element matrix equations are then assembled into a single system matrix equation which can be solved. Interpolation functions are then used to approximately evaluate the photon density distribution within each element from its nodal values. Finally, the piecewise assembly of the individual elements provides a continuous map of the radiation

distribution within the media. The FEM model has been shown to be in good agreement with the predictions of Monte Carlo simulations and the analytical solutions of the diffusion approximation for simple geometries.[70] For simplicity and reduced computation time the FEM study by Arridge et al[70] was limited to a two-dimensional mesh and employed a linear interpolation function. FEM has the advantage of being applicable to any geometry and it is significantly faster than Monte Carlo. However, the technique is still computationally expensive, particularly when it is extended into 3-dimensions. Note that a higher order approximation to the Boltzmann equation could be used to improve the model, although this would increase the complexity of finding a solution and hence the computation time.

3.5.3 RANDOM WALK

In the Random Walk approach[36,71,72] the media is again divided into smaller volumes, or voxels, and the photon can either move into an adjacent voxel or be absorbed depending upon the optical properties of the voxel. Initially this method assumed equal probability in any direction, equivalent to isotropic scatter, although later models have incorporated different probabilities for photon propagation direction, equivalent to anisotropic scatter. Random walk theory can derive useful expressions such as the probability of finding a particular photon at position r after N steps for a given lattice arrangement. Unfortunately, the mathematics becomes very complex for small N and can only be solved numerically. However, for a large number of steps, (ie $N >> r/l$ where l is the step size), it is possible to derive analytic solutions. It should be noted that a large number of steps corresponds physically to a low probability of absorption (ie $\mu_a << \mu_s$) which is also described successfully by diffusion theory. It is not clear at present if there is any advantage in using one approach over the other.

CHAPTER 4

OPTICAL IMAGING

This chapter provides a general introduction to the various techniques which have been proposed and investigated as a means of imaging through highly scattering media in general, and human tissues in particular. As discussed in Sec.(1.3.5) conventional transillumination of the breast was hindered by highly scattered photons which travel unknown paths through the breast and degrade the spatial resolution. Fortunately, the introduction of new technologies during the past ten years has provoked a revival of optical imaging in medicine.[73] The various technologies are reviewed, followed by a description of the imaging methods being pursued at UCL.

4.1 OPTICAL IMAGING TECHNIQUES

4.1.1 COLLIMATED TRANSILLUMINATION

An approach to improve the spatial resolution has been based on the detection of photons which have travelled directly through a scattering medium between a source and detector along the line of sight. These unscattered photons, or ballistic photons, are only influenced by the optical properties along the line of sight and hence contain the highest spatial resolution information. Therefore, several methods have been developed to detect ballistic photons, whilst disregarding the transmitted scattered photons.

Perhaps the simplest method of discriminating between ballistic and scattered photons is collimated transillumination. The principle of the method relies on the preferential detection of ballistic photons which are transmitted through a scattering medium undeviated, whereas scattered photons emerge from the surface at all angles. This is generally achieved using a collimated CW light source and a coaxial collimated detector which only permits the detection of photons emitted over a small acceptance angle to

the line of sight. Jarry et al[74] developed a scanning collimated transillumination system and reported a significant improvement in the spatial resolution compared to conventional transillumination. They imaged small metal objects embedded in 15 mm thick samples of mammalian tissue. Although 3 mm wide blades could be observed deep inside the sample, 1 mm diameter needles could only be observed near the surface. Several other authors[75,76] have also achieved gains in spatial resolution using similar systems when imaging through media of low optical thickness. Jackson et al[76] developed a sophisticated computerised tomographic method based on collimated transillumination to obtain slice images. They observed two opaque rods, each 12 mm in diameter, embedded in a paraffin wax cone of 80 mm diameter. As expected, the rod embedded 15 mm from the surface was relatively well resolved compared to the rod embedded at 20 mm below the surface. Kaneko et al[77] developed a laser scanning system, employing a degree of collimated detection, for breast imaging studies. Despite enthusiastic claims of some utility to detect certain tumours,[31] the spatial resolution and the demonstrated specificity were both poor.

The spatial resolution achieved by collimated transillumination is hindered by the detection of scattered photons which are scattered back along the line of sight. For a medium of low optical thickness the ballistic photons are dominant over the detected scattered photons and hence the improvement in spatial resolution. However, as the optical thickness of the medium increases the probability of detecting scattered photons which have strayed further from the line of sight increases. Furthermore, as the scattering coefficient of the medium increases the number of ballistic photons decreases. Therefore, for media of high optical thickness the detected scattered photons are dominant over the ballistic photons and there is negligible improvement in spatial resolution. Collimated transillumination is therefore limited to imaging through media of low optical thickness.

The transmission of ballistic photons through the breast may be easily evaluated by substituting typical breast optical properties ($\mu_s = 30$ mm^{-1}, $\mu_a = 0.005$ mm^{-1} and $d = 50$ mm) into Eq.(2.9) and Eq.(2.10) which gives a transmission probability of approximately e^{-1500} (effectively zero). Therefore collimated transillumination of the breast only detects

highly scattered photons and so there is no improvement in spatial resolution compared to conventional transillumination.

A similar approach to collimated transillumination, known as spatial Fourier filtering, has been suggested by Wang et al.[78] Their technique uses a lens, focal length f, to focus the photons emitted from the surface of a scattering medium to a position in the focal plane dependent upon the angle at which they were emitted. By placing a small aperture at the centre of the focal plane only light emitted normal to the surface will be transmitted. A second lens, focal length f, is placed at a distance 2f from the first which forms an image using the light passing through the aperture. Therefore, the technique provides an image generated only from photons which are emitted normal to the medium's surface. However, spatial fourier filtering is still subject to the same limitations of collimated transillumination and is therefore limited to imaging through media of low optical thickness.

4.1.2 COHERENT IMAGING

Attempts have been made to discriminate between ballistic and scattered photons interferometrically using coherent sources. Whereas ballistic photons retain the coherent properties of the incident light, multiply scattered photons are effectively rendered incoherent. There have been several different coherent detection methods developed.

Several authors[79-83] have successfully demonstrated holography as an effective way of detecting the transmitted coherent light through scattering media. Abramson and Spears[80] developed the use of a pulsed light-in-flight (LIF) holographic technique. This involved transmitting an ultrashort picosecond laser pulse through the scattering sample while a reference pulse from the same laser was sent directly to a holographic plate where it arrived coincident with the emerging light from the sample. Coincidence was achieved by introducing a time-delay so that the reference pulse arrived at the holographic plate simultaneously with ballistic photons from the sample. Thus, a hologram is created between the coherent ballistic photons and the reference pulse, while the scattered photons contribute an incoherent background noise. In practice, laser sources have a

finite coherence time which is shorter than the pulse duration. This means that photons which are slightly scattered and are transmitted within the coherence time will retain some coherent properties with the source. Therefore any slightly scattered photons which are transmitted within the coherence time can also form part of the hologram. Hence the spatial resolution of the technique is limited by the coherence time of the laser source. The desire for improved spatial resolution has provoked the development of more sophisticated systems using femtosecond pulses which have shorter coherence times. Chen et al[79] describe a femtosecond system using a CCD camera to detect the hologram. Computer processing of the hologram is employed to remove the incoherent background to improve contrast and averaging multiple holograms to improve the signal to noise ratio (SNR). They have reported imaging three 1 mm diameter wires embedded in a 4 cm wide tank filled with a diffusing medium. However, it is certain that the diffusing medium, consisting of latex microspheres of unspecified concentration suspended in water, was not as highly scattering as breast tissue. Hyde et al[83] describe a picosecond system which detects the reflected, rather than transmitted, coherent signal from an object which enables depth-resolved images to be obtained. They employ a photorefractive crystal to record the hologram and report imaging a test object, consisting of concentric cylinders, through a scattering solution with millimeter depth resolution.

An alternative to an ultrashort pulse is to use a long pulse or CW light source with a short coherence time. In practice, the coherence time can be much shorter than the pulse duration. As before, scattered photons which are transmitted later than the coherence time are rendered incoherent and so the spatial resolution is limited by the coherence time of the laser source. This principle was employed in the original LIF experiments pioneered by Abramson et al which used a short coherence time CW light source. More recently Spears et al[81] have used long pulses (approximately 5 ns) with much shorter coherence times (approximately 1 ps) in their chronocoherent imaging technique. The technique was employed to image a black letter "E" (8 mm x 2.5 mm) obscured by two ground glass diffuser plates. They also reported imaging a black letter "C" (1 cm x 0.2 cm) through 28 slabs of parafilm which corresponds to 1.8 cm of breast tissue. The possible advantage of using longer pulses or CW light is that they involve less expensive

technology than those incorporating ultrashort pulses. It must be noted that generally these holographic techniques are hindered by the presence of an incoherent background of scattered photons which substantially reduces the hologram contrast for media of high optical thickness. However, the photorefractive effect employed in the technique by Hyde et al[83] is insensitive to the incoherent background.

Discrimination between coherent ballistic photons and incoherent scattered photons has also been attempted using non-linear optical processes[84-89] which are strongly dependent upon the degree of coherent correlation between two beams. Reintjes et al[86] have developed techniques using non-linear optical Raman interactions. These have either used short laser pulses,[87,88] or long laser pulses with short coherence times.[86,89] One technique was based on the phenomenon known as coherent anti-Stokes Raman scattering (CARS).[89] In the CARS experiment a long laser pulse (approximately 8 ns) with a short coherence time (approximately 250 fs) and wavelength of 566 nm is split into a pump beam and a sample beam. The sample beam passes through a Raman cell to produce Stokes radiation at 740 nm which is used to illuminate the scattering media. A time-delay is introduced to the pump beam such that it arrives at a CARS cell coincident with the ballistic Stokes radiation. The transmitted Stokes radiation and pump beam are then combined in the CARS cell where they undergo the CARS effect to produce anti-Stokes radiation at 458 nm. Therefore, the intensity of the anti-Stokes radiation produced, determined by the coherent correlation between the transmitted Stokes radiation and pump beam, is mainly influenced by the intensity of the coherent ballistic photons. As the anti-Stokes radiation is emitted from the CARS cell at a different angle than the transmitted Stokes radiation and pump beam it can be easily detected by a CCD camera. Reintjes et al[86] have reported obtaining sharp images of test bars, 0.5 mm thick, hidden behind 6 mm of raw chicken tissue. One problem with the technique is that the transmitted Stokes radiation and pump beam must be crossed at an angle in the CARS cell to ensure phase matching. Unfortunately, this leads to a reduced spatial resolution of images in the plane of the crossing angle.

Reintjes et al[86] have also developed a technique using the phenomena known as stimulated Raman scattering (SRS). This is very similar to the CARS method, although

the CARS cell is replaced with a Raman cell. A potential problem with this technique is that the Stokes radiation produced is emitted from the Raman cell in the same direction as the transmitted scattered Stokes radiation. This will lead to an incoherent background in the detected image, as experienced in holographic techniques. However, as there is no requirement for phase matching, there is equal spatial resolution of the images in all directions. A recent improvement to the technique by Bashkansky et al[85] is known as coherently amplified Raman polarisation (CARP) and utilises the polarisation properties of the SRS effect. This involves linearly polarising the Stokes radiation before it enters the scattering medium and polarising the pump beam either circularly or linearly at 45 degrees to this direction. The Stokes radiation produced in the Raman cell will then be perpendicularly polarised to the original Stokes radiation. Placing a polariser after the Raman cell will preferentially allow ballistic Stokes light to be detected as opposed to scattered Stokes radiation which will be randomly polarised. They have reported imaging a cross pattern of 1 mm thick bars hidden behind a 1 cm wide scattering cell filled with a solution of microspheres (corresponding to μ_s' = 0.2 mm^{-1}).

Polarisation discrimination has also been investigated by other authors.[90-92] Schmitt et al[91] demonstrated the ability to measure 0.1 % fraction of circularly polarised light through scattering suspensions of polystyrene spheres which suggested that it should be measurable through tissues up to 10 mm thick. Monte Carlo simulations and laboratory experiments reported by Bruscaglioni et al[92] indicated that total depolarisation is reached after a depth of ten transport scattering lengths, which again suggests a limiting tissue thickness of about 10 mm.

Alternative attempts to distinguish between coherent ballistic photons and scattered incoherent photons have also included heterodyne detection techniques.[93-96] In general these involve a laser beam being split into a sample beam which illuminates the scattering media and a reference beam which is passed through an acousto-optical modulator to produce a frequency shift. The reference beam is then directed so that it interferes collinearly with the transmitted beam from the scattering media, e.g. with a Mach Zender interferometer. A heterodyne detector is then used to detect the beat

frequency produced by the reference beam and the transmitted beam. As only the ballistic photons retain coherence with the reference beam, the amplitude of the beat frequency is directly proportional to their intensity. The incoherent scattered light forms an effective constant background noise which can in principal be removed. More sophisticated systems using coherent imaging techniques to perform optical coherence tomography (OCT) have been developed. Inaba[94] has reported a heterodyne coherent system and imaged various objects in scattering media, e.g a metal clip made from 0.7 mm diameter steel wire embedded in 10 mm of chicken tissue. Incorporation of tomographic backprojection enabled slice images to be obtained of a new-born mouse head, approximately 1 cm diameter, which identified the skull and various regions of the brain.

In summary, although the coherent imaging methods described above have demonstrated some utility for media of low optical thickness, they are unlikely to be of use in thick tissues, such as the breast, where all the transmitted light is highly scattered and rendered incoherent.

4.1.3 TIME RESOLVED IMAGING

Until the relatively recent advent of ultrafast optical sources and detectors, the possibility of acquiring high spatial resolution images through thick, highly scattering media seemed formidable. However, when a scattering medium is illuminated with a short pulse of light the transmitted photons will travel different paths through the scattering medium and therefore have different flight times. The temporal distribution of the transmitted light is known as a temporal point spread function (TPSF). It follows that the shorter the flight time of the photon, the shorter its path through the medium. Therefore, for thick, highly scattering media, where there are no ballistic photons, the early arriving photons must have travelled paths closest to the line of sight. Thus, these photons are only influenced by the optical properties of a small narrow volume surrounding the line of sight which contains all the possible early arriving photon paths. Obviously, later arriving photons may have taken longer paths through the medium and thus explored a larger volume surrounding the line of sight. Therefore early arriving

photons will contain higher spatial resolution information than later arriving photons, as illustrated in Fig.(4.1).

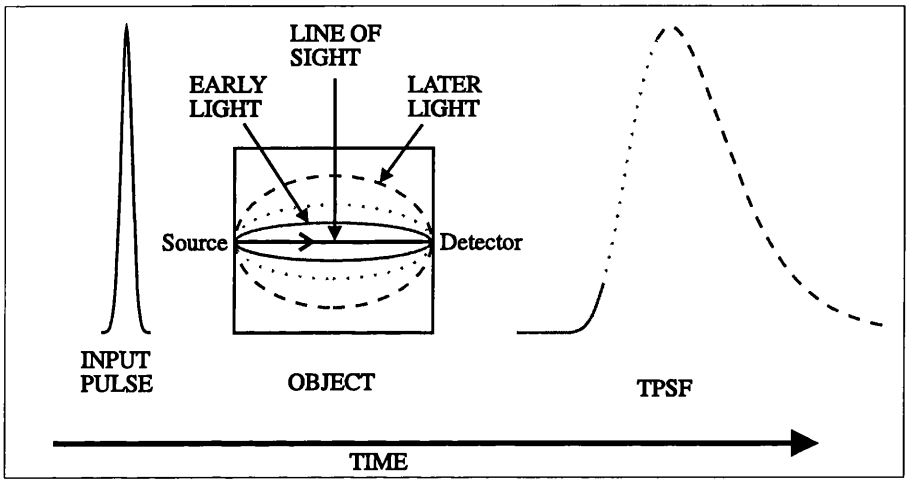

Figure 4.1 *Generation of a TPSF through a scattering medium.*

Several authors have demonstrated the potential effectiveness of using temporal discrimination to improve transillumination imaging with Monte Carlo simulations[97,98] and theoretical analysis.[99,100] This has provoked the development of several time resolved imaging techniques.

In 1971 Duguay and Mattick[101] described an ultrafast camera which employed short infrared laser pulses, 10 ps in duration, to induce temporary birefringence in a Kerr cell which thereby acted as a very fast shutter. They describe an experiment[101] that used the ultrafast camera to observe a 1 cm thick scattering cell, containing milk particles suspended in a water-alcohol mixture ($\mu_s' = 0.3$ mm^{-1}), which was illuminated with short green pulses of 10 ps duration. The infrared pulses were appropriately delayed to coincide with the green pulses passing through the cell. Therefore, the high speed film in the ultrafast camera was exposed for 10 ps and produced a photograph of the green pulse in flight through the cell. The ultrafast camera was subsequently used by Martin et al[102] to obtain reflection images from an isolated mammalian heart. More recently several researchers have used the optical Kerr gate for time-gated transmission imaging. Wang et al[103] have reported submillimeter resolution through 3.5 mm of human breast tissue using an optical Kerr gate system. A sophisticated Kerr gate system described by

Kalpaxis et al[104] employed a backprojection reconstruction algorithm to obtain three dimensional images of a rubber T-shaped object embedded in a 55 mm scattering cell containing 2% from stock intralipid solution (it is unclear whether it was a 100% or 10% stock intralipid solution). Liang et al[105] have combined a Kerr gate system with spatial Fourier filtering in an attempt to further improve spatial resolution. They reported imaging a 2 mm thick object, containing various concentrations of intralipid solution, embedded in a 55 mm scattering cell containing 0.2% intralipid solution. Unfortunately, the main disadvantage of these Kerr gate techniques is the limited dynamic range in the opacity of the Kerr cell. Measurements[102] have revealed a maximum Kerr-gate transmission of 2% when open compared to 0.005% when closed. Therefore, although the Kerr gate enhances detection of early arriving photons, the spatial resolution of the images is hindered by the presence of later arriving, highly scattered photons.

Alternative ultrafast technologies have enabled direct measurement of the TPSF. Time-gating can then be performed by integrating the TPSF over a desired time-window (Fig.(4.2)). The advantage of this approach over all previous methods is that time-gated images can be generated for any chosen time-window and, in principle, will have no contribution from later arriving light.

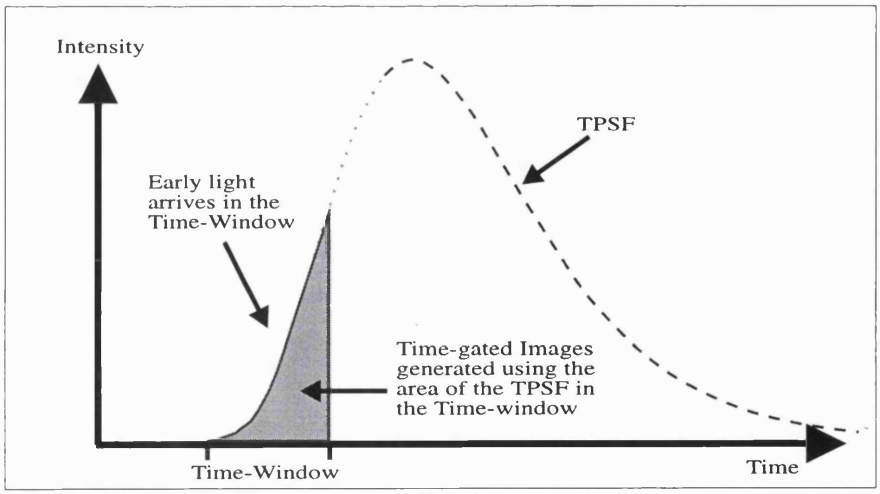

Figure 4.2 *Principle of time-gated imaging.*

Berg et al[106] describe a system based on the time-to-amplitude converter (TAC) for measuring the TPSF through a scattering object. A laser pulse is used to illuminate the scattering object and the transmitted photons are detected on a photon-counting micro-channel plate photo-multiplier tube (PMT). The signal from the PMT is fed through a fast amplifier and a discriminator to the TAC. The output signal from the TAC is then fed to a multichannel analyser in which a histogram of the photon arrival times (i.e. the TPSF) is formed and can be recorded on computer. The system was used to measure the TPSF through breast tissue samples and the first time-gated images of a tumour within a 30 mm thick breast sample (*in vitro*). The same system was employed by Andersson-Engels et al[107] to image 5 mm diameter black rubber cords embedded at different depths in both a 35 mm thick paraffin phantom and 34 mm thick sample of breast tissue (*in vitro*). They also used the system to scan across part of a human hand (*in vivo*) which identified the finger bones. Benaron and Stevenson[108] developed a similar system, known as the time-of-flight and absorbance (TOFA) scope to obtain time resolved images of a dead rat. These revealed several major internal features of the rat, such as the heart, liver, spleen, pancreas, and intestinal gas. The system was adapted to obtain tomographic slice images of the neonate brain (*in vivo*) and was able to identify severe incidence of brain haemorrhage.[109] However, the disadvantages of these TAC systems are the relatively low maximum photon count rate (around $2x10^4$ photons per second) and the low temporal resolution of the detector (about 100 ps at best).

An alternative device which enables a TPSF to be sampled with very high temporal resolution when illuminated with a train of laser pulses is a streak camera. Photons transmitted through a small input slit at the front of the streak camera are incident on the photocathode of a streak tube which converts them into electrons. These electrons are directed towards a phosphor screen at the end of the streak tube by accelerating electrodes. A sinusoidal potential is applied to deflection plates within the streak tube which is synchronised to the train of laser pulses. Hence, the deflection plates cause the electrons to be continuously swept across the surface of the phosphor screen creating a streak image. Therefore the streak image represents an intensity versus time measurement of the photons transmitted through the slit. The streak camera is able to sum the streak images produced by multiple pulses with a temporal resolution of

approximately 20 ps. Generally, a CCD camera is mounted on the rear of the streak camera to detect the streak image. By averaging the streak image along the slit axis a streak profile, i.e. a TPSF, may be obtained which can be stored on a computer. Hebden et al[110-113] have reported the use of a streak camera system to measure TPSFs through various scattering media. One experiment[113] involved two-dimensional imaging of opaque and transparent spheres (8 mm in diameter) embedded at different depths in a 51 mm thick scattering cell containing a solution of latex microspheres ($\mu_s' = 0.2$ mm^{-1}). This was further extended[114] using tomographic reconstruction techniques to obtain slice images of six glass tubes of various diameters embedded in a larger cylinder (50 mm in diameter). The cylinder and tubes were filled with a scattering solution of nondairy creamer ($\mu_s' = 0.3$ mm^{-1}) and the tubes were filled with different concentrations of absorbing dye. A streak camera system, similar to that used by Hebden et al, is used in my Ph.D. research and is discussed in more detail later. The principal disadvantages of streak cameras are the relatively small effective light collection area (about 1 mm^2) and the high cost (>£50K).

Time-gated imaging has been demonstrated, both by simulation and experiment, to significantly improve the spatial resolution of images obtained through highly scattering media compared to conventional transillumination. However, there are several main disadvantages of the technique. First, time-gating, by definition, is extremely inefficient as only the early arriving photons are used while later arriving photons are discarded. Second, although a smaller time-gate should, in principle, improve the spatial resolution, it is accompanied by a decrease in the number of detected photons. Therefore there is a limit to how small the time-gate can be made before there are insufficient photons transmitted to give adequate SNR, and the images become dominated by noise. Hebden et al[115,116] have reported that time-gated images through highly scattering breast-like media are limited to a spatial resolution of approximately 1 cm compared to several centimetres for conventional transillumination. Therefore time-gated imaging can still not obtain the spatial resolution adequate for breast screening. A novel technique introduced by Hebden and Delpy[117] has attempted to enhance the performance of the time-gated method. This technique, called temporal extrapolation, is the principle method employed in my Ph.D. research and is discussed in Sec.(4.3).

4.1.4 FREQUENCY DOMAIN IMAGING

Since any measurement in the time domain can be equivalently expressed in the frequency domain, researchers[38,66,118,119] have sought to acquire transmitted light information in the frequency domain directly. The main advantage of this approach is that CW light sources and detectors can be employed which are generally significantly less expensive than the time domain systems. In theory, a time domain measurement, with 20 ps temporal resolution, could be achieved in the frequency domain by intensity modulating a CW light source over a range of frequencies from zero to 50 GHz and detecting the modulation depth and phase shift of the transmitted light. A Fourier transform of this hypothetical data could then provide the TPSF as measured in the time domain. Unfortunately, in practice there are severe technical limitations.[118] First, for low frequencies there is a very small change in the phase shift of the transmitted light which is hard to measure accurately. Second, for very high frequencies there will be phase shifts greater than 2π which can only be accounted for using phase unwrapping techniques. Also at high frequencies the modulation depth decreases and may be hard to measure. Finally, current technical limitations mean that gigahertz modulation frequencies are not available. At present, for several centimetres of tissue a frequency range between 200 - 500 MHz can be used where the modulation depth is still large enough to be measured and the phase shift is significant but still below 2π. At this limited range of frequencies it is not possible to fully reconstruct the TPSF with the equivalent temporal resolution of a streak camera. Duncan et al[118] reported that for low frequencies up to approximately 300 MHz across 4 cm of adult head, their is a linear relationship between the phase shift, ϕ, and the modulation frequency, ω, given by

$$\phi = \omega . \langle t \rangle \quad , \tag{4.1}$$

where <t> is the mean flight time of the TPSF. Therefore, for existing frequency domain systems it is possible to measure the mean flight time of the transmitted photons, although the shape of the temporal distribution can only be measured with around 2 ns resolution. The results reported by Duncan et al[118] are given in Fig.(4.3)-(a) and show a TPSF, with its corresponding <t>, measured in the time domain using a streak camera

system across 4 cm of adult head. Also shown in Fig.(4.3)-(b) is the corresponding phase shift and modulation depth, M_D, in the frequency domain, calculated as the Fourier transform of (a).

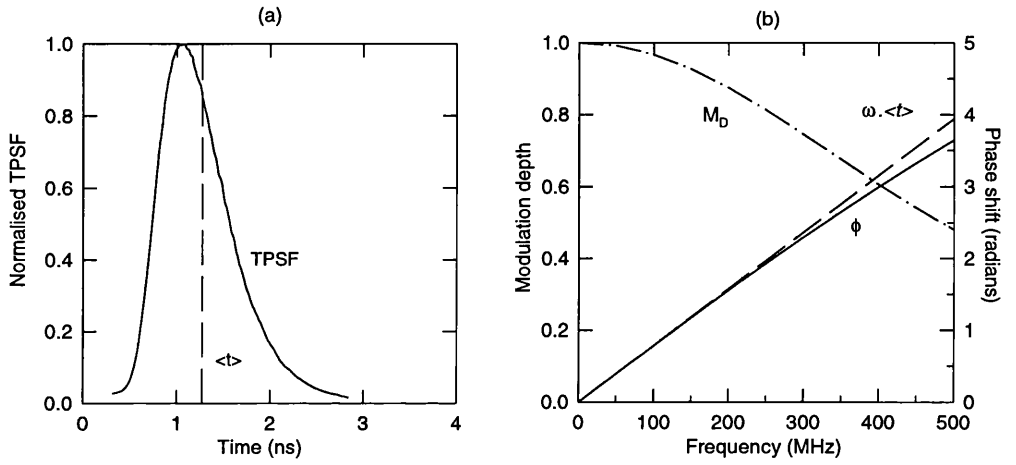

Figure 4.3 *A typical TPSF in the (a) time and (b) frequency domain.*

Note that at frequencies from about 300 MHz up to 500 MHz there is a slight departure between phase shift and ω.<t> due to the skewness of the TPSF. Unfortunately, present technological limitations prevent the direct measurement of any higher frequency information.

The closely related field of near infrared spectroscopy (NIRS) is concerned with measuring changes in the average optical properties of a large tissue volume, e.g the brain, and relating them to changes in various tissue chromophore concentrations. As <t> is influenced by the optical properties of the average volume explored by all the transmitted photons it may be used to quantify these changes. Duncan et al[120] have reported the use of a frequency domain system for clinical measurement of <t> in preterm babies. An advantage of frequency domain systems is that they are small enough to be used clinically in intensive care units.

Whilst frequency domain systems have found great success in NIRS they have only recently been employed for optical imaging. Gratton et al[121] used a frequency domain system to obtain images through a hand (*in vivo)* which revealed internal structures such as bones and blood vessels, claiming a spatial resolution of about 1 mm. Fantini et al[122]

have reported the use of a frequency domain system for imaging the breast (*in vivo)* and detection of a tumour approximately 1.5 cm in size. The effectiveness of prototype frequency domain breast imaging systems is currently being assessed through clinical trials by Siemens AG and Carl Zeiss in Germany.

4.2 ITERATIVE RECONSTRUCTION IMAGING

The imaging techniques described so far have attempted to detect either ballistic photons or those confined to a small, narrow volume surrounding the line of sight, whilst disregarding the highly scattered transmitted photons. An alternative approach[123-127] is based on the assumption that given a set of measurements of transmitted light between pairs of points on the surface of an object, there exists a unique three dimensional distribution of internal scatterers and absorbers which would yield that set. The reconstruction of this distribution from the measurements is an example of an inverse problem. Schweiger et al[123] have approached the inverse problem using an iterative reconstruction algorithm outlined in Fig.(4.4).

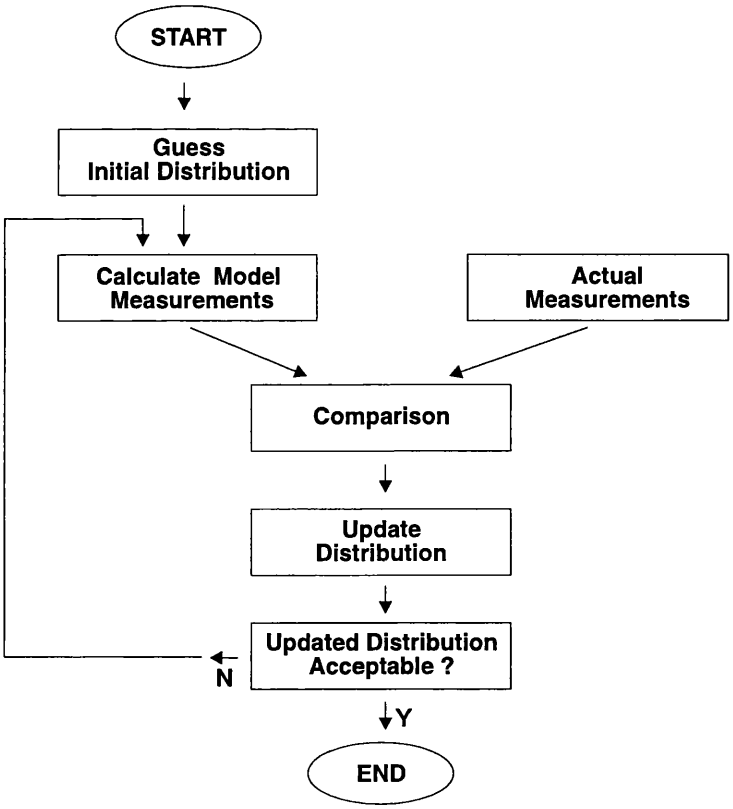

Figure 4.4 *Principle of the iterative reconstruction algorithm.*

A photon propagation model is applied to an initial guess of the distribution to generate model measurements. The model used was a numerical solution of the diffusion equation using FEM (see Sec.(3.5.2)). Comparison of the actual and model measurements leads to a correction of the distribution, which can be iteratively re-fed into the model until the difference between the model and actual measurements is sufficiently small. The highly ill-posed nature of the inverse problem and noise in the actual measurements requires regularisation methods to be employed in the algorithm.

The measured quantity can, in principle, be any property of the transmitted light, even total transmitted intensity. However, in practice, higher moments of the TPSF are found to be more suitable. The mean flight time, <t>, for example, is found to be far less dependent on surface interactions than total transmitted intensity. If available, several independent measurement quantities are employed, since the more information provided about the transmitted light the better defined the inverse problem becomes. Schweiger et al[124] have used measurements of <t> to generate a two-dimensional slice image of two 5.1 mm diameter plastic rods of different scattering properties (μ_s' = 6.5 mm^{-1} and 1.5 mm^{-1}, μ_a = 0.09 mm^{-1} for both) embedded in a larger 70 mm plastic cylinder (μ_s' = 1.5 mm^{-1} and μ_a = 0.04 mm^{-1}). Arridge et al[126,127] have demonstrated the same technique theoretically using computer simulated data. Although significantly faster than Monte Carlo an iterative FEM reconstruction algorithm is still highly computationally expensive, particularly when extended into 3-dimensions.

4.3 TEMPORAL EXTRAPOLATION

One of the objectives of my Ph.D. research has been to assess the utility and limitations of an extension of time-gated imaging known as temporal extrapolation. This concept was originally suggested by Hebden and Delpy[117] who used it to obtain two-dimensional time resolved extrapolated images of opaque and transparent spheres (8 mm in diameter) embedded at different depths in a 51 mm thick scattering cell containing a solution of latex microspheres (μ_s' = 0.76 mm^{-1}) and a NIR absorbing dye (μ_a = 0.011 mm^{-1}). The technique attempts to extract high resolution information by fitting a mathematical model of photon migration to all or part of the TPSF in order to improve the estimation

of the short pathlength photons. The model is then used as if it represented a noise free estimate of the original data and images are created using the predicted intensities of short pathlength photons. Despite the limitations of using simple models which assume homogeneous media, the experimental results for inhomogeneous phantoms have so far been encouraging.[115-117,128-130]

The argument in support of this method is based on the observation that the transmitted intensity of photons of all pathlengths are influenced to some degree by the optical properties along the line of sight. Thus the model fitting provides a means of extrapolating a TPSF, known to be smooth and continuous, to shorter flight times where the spatial resolution is higher. Obviously, this extrapolation technique cannot generate high resolution information from data in which it not already contained, and therefore relies upon how accurately the model can infer the true population of short pathlength photons from longer pathlength photons. Selecting the degree of complexity of the model involves compromise between the need to reproduce the shape of the data and the need to suppress the random effects of noise. So far in my Ph.D. research relatively simple models such as the semi-infinite slab solution to the time dependent diffusion equation (Eq.(3.20)) as formulated by Patterson et al[64] (subsequently known as the PCW model), have been shown to satisfy this compromise particularly well. In practice, the transmitted intensity function, $T(\rho,d,t)$, is integrated over a finite aperture of radius R centred on the line of sight, where R is the radius of the detector. However, since the apparatus used to measure the TPSF does not measure transmitted intensity in absolute units, when fitting to experimental data the function $T(R,d,t)$, is scaled by an arbitrary constant A.

An inherent problem in using a diffusion theory model is its inability to describe the transmitted intensity of photons from an incident laser pulse at very short times. This is because these photons will not have had time to undergo multiple large angle scattering which is inadequately described by diffusion theory that assumes an isotropic source. Furthermore, the diffusion approximation does not satisfy the principle of causality. In other words, a transmitted intensity can only be measured at some distance from the source after at least the time for straight propagation from the source has

elapsed. However, in the diffusion approximation a non-zero intensity exists at all points in the volume at the instant following the generation of the isotropic point source (approximated to the photon entry time) which is obviously non-physical. For time-gating experiments, time zero is chosen to be the time at which a ballistic photon emerges from the slab. Therefore when fitting the PCW model to a measured TPSF, the time, t, includes an offset, t_0, equal to the ballistic flight time. Thus, in my Ph.D. research the actual expression used in the fitting procedure is given by

$$T(R,d,t) = AD^{-\frac{3}{2}}(t-t_0)^{-\frac{5}{2}}\exp(-\mu_a c(t-t_0))\; Q(d,t-t_0)\int_0^R \rho\; \exp\left(-\frac{\rho^2}{4Dc(t-t_0)}\right) d\rho \quad , \tag{4.2}$$

where $Q(d,t-t_0)$ is the dipole source term given in Eq.(3.17).

The appeal of this model is the relatively simple mathematics involved in fitting it to an experimental TPSF . Despite the various approximations and assumptions made in its derivation, it does nonetheless appear to correspond very well to experimental TPSFs obtained through homogeneous media, yielding realistic values for μ_a and μ_s' (see Chapter 6). Although the PCW model is only strictly valid for homogeneous media it is still possible to obtain reasonable fits for inhomogeneous media if all the parameters (μ_a, μ_s', A and t_0) are allowed to vary during the fitting procedure (see Chapter 6). Experiments show that although the final fit parameters themselves may not be particularly meaningful, it is still possible to use the fit for extrapolation.

A typical example of the PCW model fitted to an experimental TPSF obtained through an inhomogeneous medium, (see Sec.(6.2)), is given in Fig.(4.5),

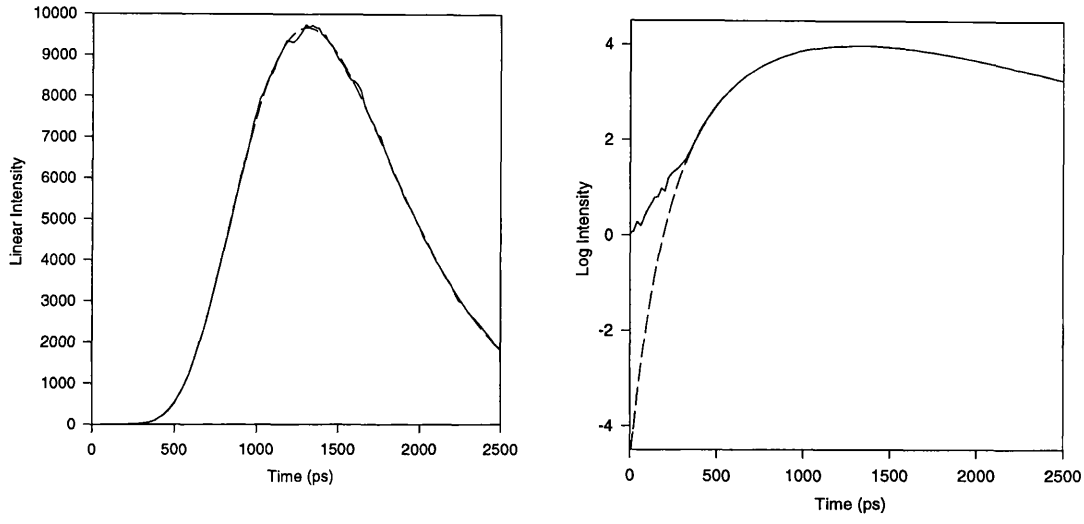

Figure 4.5 *Principle of temporal extrapolation.*

This illustrates the inherent limitation of time-gating and also reveals the basis for the reasonable success of the temporal extrapolation technique. The PCW model curve (dashed line) aligns closely with the experimental TPSF (solid line) and is able to continue the general trend to smaller integration times where the experimental TPSF becomes dominated by noise. The accuracy of the extrapolation will decrease with decreasing flight time and research described in Chapter 6 has sought to investigate whether or not it is possible to extrapolate far enough to produce images with a spatial resolution adequate for breast screening.

CHAPTER 5

THE TIME RESOLVED NIR IMAGING SYSTEM

This chapter describes the time resolved NIR imaging system which has been employed and developed during my Ph.D. research. The overall purpose of the time resolved NIR system is to obtain time resolved images of highly scattering media when illuminated with short pulses of NIR radiation. Described in more detail below is the experimental apparatus which is used to acquire the TPSFs and the data processing required to generate time resolved intensity images.

5.1 EXPERIMENTAL APPARATUS

A schematic representation of the experimental set up, similar to that reported by Hebden et al,[110-112] is given below.

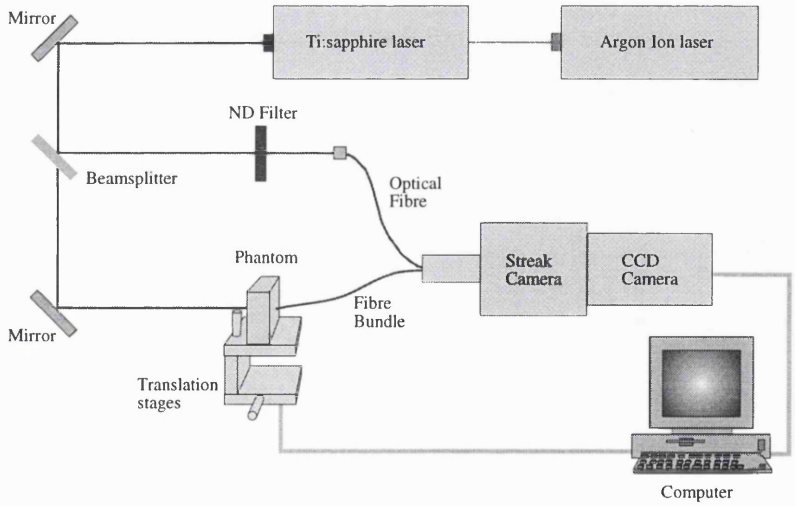

Figure 5.1 *The time resolved NIR imaging system.*

5.1.1 THE SYSTEM COMPONENTS

Near infrared pulses, a few picoseconds in duration, are produced at a rate of 82 MHz by a Spectra-Physics Tsunami Ti:Sapphire laser pumped by a Spectra-Physics 2040 Argon-ion laser. The wavelength of the NIR pulses may be tuned between approximately 700 nm to 900 nm. The maximum average output power of the Tsunami is approximately 1.5 Watts when pumped at approximately 8 Watts. A beam splitter is used to divide the beam of pulses into a reference pulse and a much more intense diagnostic pulse. The diagnostic pulse, 3 mm in diameter, is directed, via mirrors, onto the object's surface. The light emitted from a small area on the opposite surface of the object, collinear with the diagnostic pulse, is collected by a 2 mm wide optical fibre bundle coupled to the input slit of a Hamamatsu C1587 streak camera. Meanwhile, the reference pulse is relayed via another fibre directly to the input slit of the streak camera. Generally, the optical pathlengths of the reference and diagnostic arms are adjusted such that the reference and diagnostic pulses arrive at the streak camera simultaneously in the absence of an object. The reference pulse therefore allows absolute temporal alignment of the TPSFs at a later stage in the data processing (see Sec.(5.2.1)). The streak camera (see Sec.(4.1.3)) is synchronised with the train of pulses using the modelocker signal from the Ti:Sapphire laser. This measures the temporal distribution of the light transmitted through its input slit which is exhibited as a streak image on the phosphor screen. The streak camera generates streak images with a temporal resolution of approximately 20 ps. It is important to ensure that the streak camera is not damaged by excessive exposure by inserting appropriate neutral density (ND) filters into the beam when necessary.

A Hamamatsu C3640 CCD camera is mounted on the rear of the streak camera to record the streak image on the phosphor screen. It is operated for routine usage via Hamamatsu's own software, PCTA version 6.0a. The camera is based on a 1024x1024 CCD which, in practice, is binned to a 512x512 array to decrease the streak image transfer time between the CCD camera and the computer. As discussed in Sec.(4.1.3), when the streak image is averaged in the spatial direction of the streak camera it produces a streak profile (TPSF). The random noise in the TPSF is reduced by

accumulating several streak images and averaging. The acquisition parameters consist of an integration time, i.e. the exposure time per frame, and an accumulation count, i.e. the number of frames taken. Therefore the total exposure time per TPSF is equal to the integration time multiplied by the accumulation count. To obtain the optimum dynamic range for the TPSF the integration time should be sufficiently long for the streak image to totally fill the memory buffer available for a single frame. To obtain the optimum SNR for the TPSF the accumulation count must be maximised in accordance with the computer memory limitations. The PCTA software outputs a single frame as 12-bit data and has a maximum available storage memory of 16-bits. This implies an acquisition of 16 full frames before saturation. However, in practice, the integration time and accumulation count are not fully optimised in order to maintain the experiment duration within a comfortable limit (e.g. a few hours).

The software also performs a dark correction, shading correction, and linearity correction to the streak image. The dark correction compensates for the dark current produced by the CCD camera by subtracting an image recorded with the shutter closed from each streak image. The shading correction compensates for the non-uniform gain across the phosphor screen of the streak camera by normalising the streak image to a calibration image obtained under uniform illumination. The linearity correction compensates for the non-linear sweep of the photon electrons across the phosphor screen in the streak camera. Non-linearity arises from the sinusoidal form of the sweeping voltage which causes the sweep speed to be lower at the beginning and end of a sweep. This non-linearity causes a distortion to the temporal axis of the streak image which becomes more pronounced at slower sweep speeds. The Hamamatsu C1587 has four sweep speeds which correspond to maximum temporal widths across the phosphor screen of 0.75, 1.0, 2.0, and 3.6 ns. These are subsequently referred to as streak times 1, 2, 3, and 4 respectively. Unfortunately, in order to acquire the majority of the TPSF through breast-like media it is necessary to use the slower streak speeds[115,116,128-130] for which the non-linearity is more significant. The linearity correction is performed by approximating the sweep speed of the streak camera to a fourth or fifth order polynomial function. The polynomial coefficients, known as linearity coefficients, are determined for each streak time from a calibration experiment, and are used to rescale the temporal axis of the

TPSF following each acquisition. Therefore, a possible source of error in the temporal axis of the TPSF arises from the approximations in the linearity correction. Finally, the resulting dark-, shading-, and linearity-corrected TPSF, with its corresponding reference pulse profile, are stored on the computer disk as two separate data files, each consisting of 512 time, intensity data pairs.

5.1.2 AUTOMATION OF THE SYSTEM

In order to obtain a time resolved image it is necessary to acquire TPSFs corresponding to multiple lines of sight through the object. For this single channel system this may be achieved by scanning the diagnostic beam and streak camera fibre bundle in parallel across the surface of the object. In practice, however, it is easier to translate the object, while the streak camera fibre bundle and diagnostic beam remain stationary. Previous experiments have employed motorised translation stages to move the object either in one dimension (1D) or two dimensions (2D) relative to the diagnostic beam and streak camera fibre. When a 2D time resolved image is required the object is translated in a raster-scanning fashion. The resulting time resolved image may consist of a single image row, for a 1D scan, or multiple image rows, for a 2D scan. However, this procedure involves the use of translation stage software to move the object, in addition to the CCD camera software to acquire the TPSFs. In practice, running two programs simultaneously proved to be both time-consuming and tedious and the procedure was in desperate need of automation.

The initial stage of my Ph.D. research involved the development of an automation program which combined and improved the existing translation stage and CCD camera software. The automation program, which I developed in the C programming language, is provided a list of instructions that are contained in a "script" file. These instructions are used to operate either the translation stage or CCD camera. Several script files were created to control various imaging procedures. For example, one script file automatically raster-scans the object in two-dimensions, whilst acquiring and storing a TPSF and reference pulse profile at 2 mm intervals. The implementation of the automation program has significantly reduced the previous tedious nature of imaging experiments,

simplified the user operation, and increased the rate of data acquisition by a factor of ten. This has enabled more ambitious imaging experiments to be performed which were previously impractical due to time constraints. However, total automation of the system has been hindered by several technical limitations. One significant problem is the inherent laser instability. In practice, a person must be present at all times during an imaging experiment to ensure that the laser tuning is optimum. Small adjustments are required about every 15 minutes to optimise the Tsunami output power and to ensure pulse stability. That person must also check that the streak camera fibre remains in contact with the object's surface during scanning. Should any problems occur, the automation program includes a pause command which halts the imaging procedure until prompted by the user to continue. This allows the apparatus to be checked and any problems rectified during the imaging experiment.

Obviously, an inherent limitation on the experimental duration is the exposure time, which, for a given diagnostic pulse intensity, cannot be decreased without compromising the SNR of the data. However, in practice this only accounts for a small proportion of the overall experimental time. At present, the majority of the time per acquisition is consumed transferring the streak image to the computer via the CCD camera and applying the various corrections to it. In principal, this time could be decreased by storing each streak image on the computer and applying the various corrections after the experiment. However, there is a large cost in computer memory by storing large streak image files rather than smaller streak profile files. Furthermore, it is useful to check the streak profiles throughout the experiment for any distortions that may occur which require corrective action.

5.2 DATA PROCESSING

The TPSFs and reference pulse files that are generated by imaging experiments are normalised for variations in exposure time and converted into time resolved intensity images via several automated data processing steps outlined below.

5.2.1 TEMPORAL ALIGNMENT

The triggering circuit in the streak camera, which synchronises the sweep voltage to the modelocker of the Ti:Sapphire laser, will cause streak images to experience small, random, temporal shifts, known as trigger jitter. This will affect the temporal position of the TPSFs acquired during an imaging experiment. Therefore the initial step of the data processing involves absolute temporal alignment of the TPSFs. This is achieved by least-squares fitting a Gaussian function to each reference pulse profile, see Fig.(5.2)-(a), and aligning the Gaussian centres to a common zero time. As the reference pulse and diagnostic pulse were initially aligned in the absence of an object it is necessary to temporally offset the reference pulses by a constant, t_B, to account for the refractive index of the object. This value is calculated as follows,

$$t_B = \frac{d}{c_0}(n - 1) \quad , \tag{5.1}$$

where d = the object thickness, n = the refractive index of the object, and c_0 = the speed of light in a vacuum.

The same temporal shifts are then applied to the corresponding TPSFs, such that zero time is the time at which a ballistic photon would be detected. This new set of TPSFs are subsequently known as temporally aligned TPSFs.

5.2.2 DECONVOLUTION - GAUSSIAN SUBTRACTION

The temporally aligned TPSFs represent the true TPSFs convolved with the response of the detector. The detector response can be considered to be a smooth narrow function with a FWHM of about 20 ps, plus a very broad, low power component due (according to Hamamatsu Photonics) to the scatter of light in the optics that couple the CCD and streak camera. Consequently, the true TPSF appears to be very slightly broadened and superimposed upon a broad, low intensity background. This convolution effect is evident in the temporally aligned TPSFs which have non-zero intensity values at zero, and even

negative times, which is obviously non-physical. Although the slight broadening effect is not a particular hindrance to data analysis, the broader low intensity background is a major source of uncertainty in evaluation of the low level signal in the TPSF. Deconvolution of this detector response is technically very difficult and a reliable method has not yet been devised. Instead, the slight broadening effect is taken to be negligible and the broad low intensity background is assumed to be an addition to, rather than a convolution with, the true TPSF. This broad low intensity background can therefore be accounted for by the subtraction of a broad low level Gaussian from each temporally aligned TPSF. This background Gaussian, see Fig.(5.2)-(b), is calculated as follows. First, the centre of the Gaussian is assumed to occur at a position on the time axis corresponding to the centre of gravity of the temporally aligned TPSF. Second, the maximum amplitude of the Gaussian is assumed to be a constant proportion, k, of the total area of the temporally aligned TPSF. The value of k is estimated empirically from a mean TPSF generated from all the temporally aligned TPSFs. Finally, the Gaussian width is fixed by anchoring the Gaussian to a point on the temporally aligned TPSF corresponding to a negative time where only the convolved signal can exist. This anchor point is characterised by an *anchor time* and an *anchor intensity.* The temporally aligned, Gaussian subtracted TPSFs are then taken to be the true TPSFs and are subsequently known as corrected TPSFs.

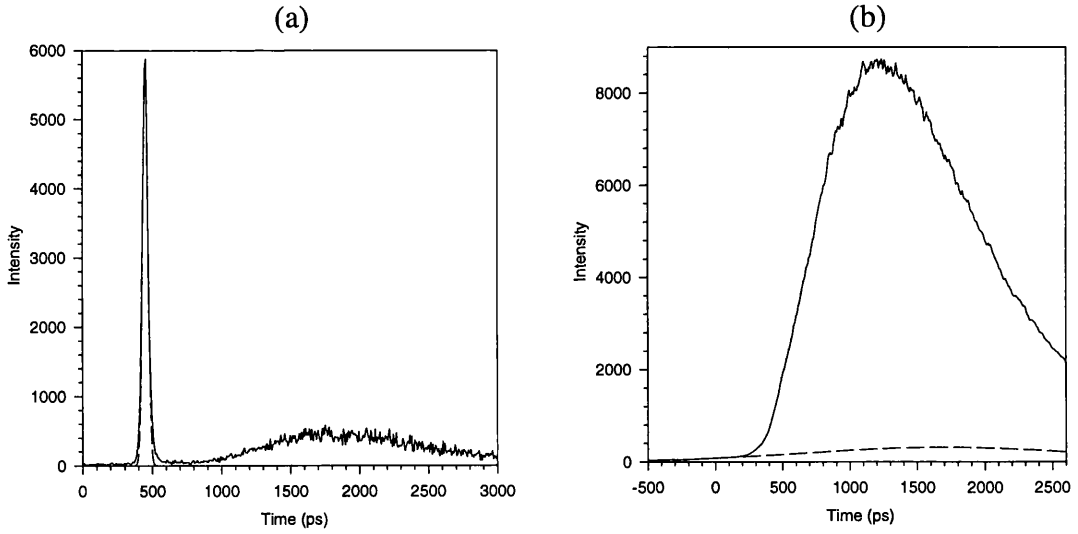

Figure 5.2 *(a) Reference pulse (solid line) with corresponding Gaussian fit (dashed line). (b) TPSF (solid line) with corresponding background Gaussian fit (dashed line).*

5.2.3 TIME RESOLVED INTENSITY IMAGES

Time-gated images are generated by integrating the corrected TPSFs over the time-window of interest and displaying the integrated intensities as a function of position. In practice, the actual percentage of the total transmitted light obtained through an object with a streak camera is object dependent. Typically about 90% of the TPSF is sampled for the breast-like phantoms described in Chapter 6. Therefore a conventional transillumination image can be approximated by integrating the corrected TPSFs over all the available time-window. As discussed in Sec.(4.1.3), due to the lack of early arriving photons, time-gated images acquired at small time-windows can be dominated by noise which limits the image spatial resolution. However, a further improvement in spatial resolution may be achieved using the temporal extrapolation technique as described in Sec.(4.3). This involves fitting the PCW model to the corrected TPSFs. By substituting the corrected TPSFs with their PCW model fits it is possible to generate temporal extrapolation images.

Computer software was written in the C programming language which applies all these data processing steps, both automatically and systematically, to the data files generated from the imaging experiments described in the next chapter. Further development of the system and software became necessary during the course of my research and is also described in the following chapter.

CHAPTER 6

EXPERIMENTAL STUDIES

This chapter describes the experimental studies conducted with the time resolved imaging system described in the preceding chapter. The main motivation of these studies is to assess the ability of the time resolved NIR system to image through highly scattering media and quantify the performance in order to indicate the potential of the methodology for breast imaging in the future.

6.1 EVALUATION OF SPATIAL RESOLUTION PERFORMANCE

6.1.1 INTRODUCTION

An imaging experiment was devised to determine the optimum spatial resolution that the temporal technique could achieve through a breast-like medium.[115] The spatial resolution measurements were performed using the method developed by Bentzen.[131] This method is based upon the reasonable assumption that the Line Spread Function (LSF) of an imaging system may be approximated by a Gaussian distribution. The LSF for a linear system is the derivative of the edge response function (ERF) and Bentzen provides an approximate expression for the finite integral of a Gaussian, consisting of an inverse polynomial. Previous work involving this technique has given sensible results. However, it should be noted that time resolved imaging is nonlinear and therefore the Bentzen method should be applied with some caution. The ERF may be obtained by recording the modulation in signal corresponding to the detection of a sharp boundary between media of highly contrasting transmittance. Four parameters which describe the response (the edge position, the maximum and minimum intensities of the edge profile, and a width parameter (σ) corresponding to the standard deviation of the corresponding Gaussian LSF) may be obtained by least squares fitting the inverse polynomial to the measured signal. Since the modulation transfer function (MTF) of the system is equal

to the Fourier modulus of the LSF, the width parameter is inversely proportional to the spatial frequency at which the MTF falls to some arbitrary fraction of its maximum. The spatial resolving power of a medical imaging system is often defined as that corresponding to a 10% response on the MTF curve, which can be shown[111] to imply a spatial resolution (Δx) given by

$$\Delta x \approx 2.93\sigma \quad . \tag{6.1}$$

6.1.2 EXPERIMENT

In order to obtain ERFs from which the spatial resolution could be evaluated the phantom shown below, Fig.(6.1), was constructed.

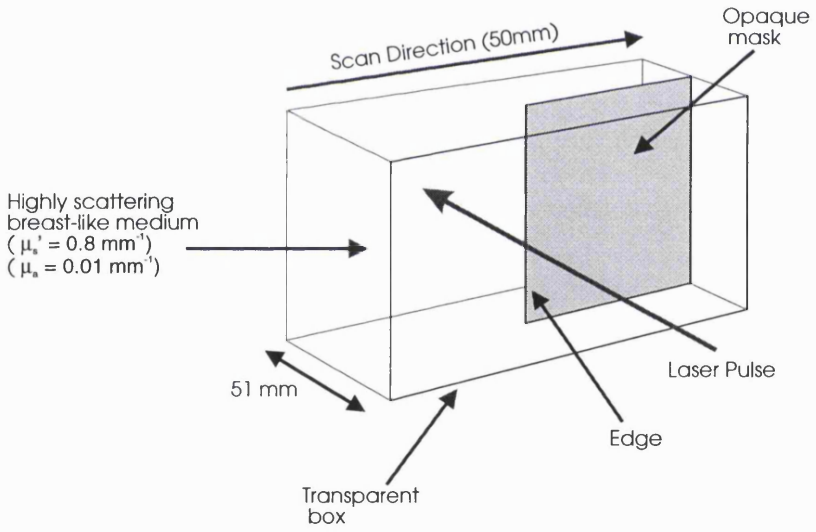

Figure 6.1 *The ERF phantom.*

It consists of a rectangular, transparent, plastic box (internal dimensions 150x100x51mm), containing an opaque mask located parallel to and halfway between the two largest sides. The vertical edge of the mask was located approximately halfway between the two smallest sides of the box. The box was filled with a scattering solution comprised from an aqueous suspension of non-absorbing 1.27μm-diameter latex

microspheres. The scattering properties of the solution, as calculated from Mie theory, were g = 0.918 and μ_s = 9.80 mm^{-1} at 790 nm, the wavelength at which the experiment was performed. This implies a transport scattering coefficient of 0.803 mm^{-1}. The refractive index of the scattering solution at 790 nm was 1.33. A near infrared dye was then added that produced an absorption coefficient of μ_a = 0.01 mm^{-1}. These optical coefficients are within the range of values expected for breast tissue (see Table (2.1)).

The time resolved imaging system was used to automatically translate a beam of pulses, wavelength 790 nm and incident power 0.75 W, 50 mm horizontally across the object in 1 mm steps, while recording the TPSF at each position. The acquisition parameters used were a fixed accumulation count of 10 and an integration time increasing from 0.5 s to 5 s as the mask moved across the line of sight. The vertical edge of the mask was aligned such that it intercepted the line of sight midway through the 50 mm scan. Streak time 3 (corresponding to a full temporal width of 2.3 ns) was used to obtain the majority (~ 90%) of the power in the TPSF. ERFs were then generated from the corrected TPSFs and PCW model fits. Note that when this experiment was performed the Gaussian subtraction had not yet been incorporated into the automatic data processing software and so a Gaussian was manually fitted to and subtracted from each TPSF.

6.1.3 RESULTS

Corrected TPSFs

ERFs were generated by integrating the intensity of each corrected TPSF over a specified time-window, Δt, and displaying the integrated intensities as a function of the displacement across the mask edge. Fig.(6.2) shows a series of normalised ERFs from the corrected TPSFs for time-windows of 300 to 1500 ps at intervals of 100 ps.

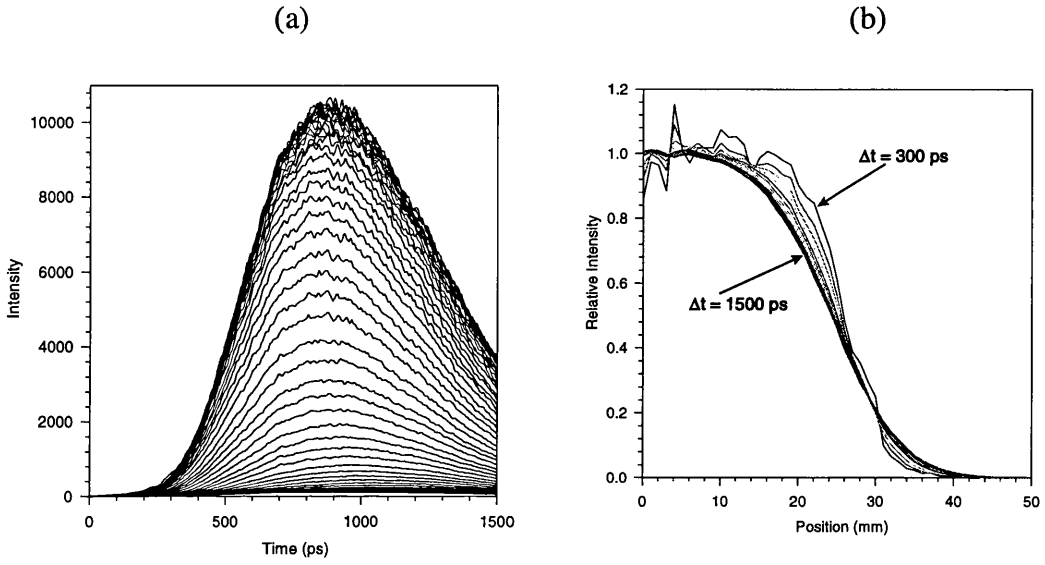

Figure 6.2 *(a) Corrected TPSFs obtained through the ERF phantom. (b) ERFs obtained from the corrected TPSFs for time-windows ranging from 300 to 1500 ps in 100 ps steps.*

In Fig.(6.2)-(b) the vertical axis represents the relative intensity of the detected light and the horizontal axis the position of the line of sight relative to the object in millimetres. The actual position of the edge is 25 mm ± 1 mm. As observed in an earlier experiment by Hebden,[111] there is a gradual increase in the slope of the curves as the time-window decreases indicating an improvement in spatial resolution. However, as expected, this increase in the slope of the curves is accompanied by a decrease in SNR. When the time-window is reduced below 300 ps the SNR becomes very low due to a lack of detected photons. Fig.(6.3) shows the ERF obtained for a time-window of 100 ps.

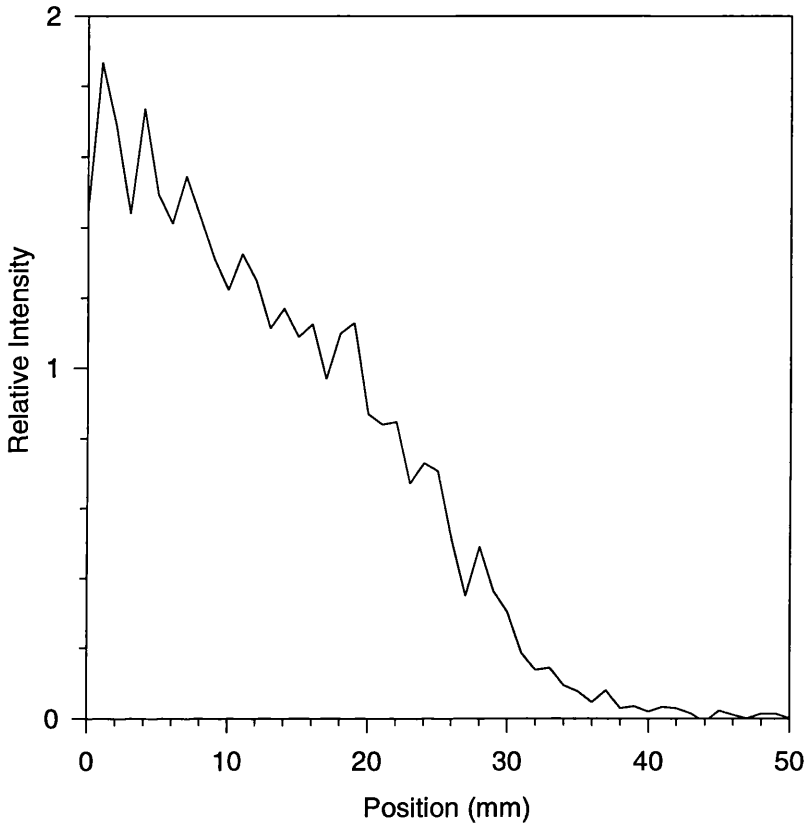

Figure 6.3 *The ERF obtained from the corrected TPSFs for a time-window of 100 ps.*

The manifestation of an "edge" (i.e. a gradient in the integrated intensity) is due almost entirely to the fact that the residual background intensity remaining after Gaussian subtraction is greater for data acquired on the side of the edge where the line of sight is unobscured by the mask.

The Bentzen model was least squares fitted to each of the ERFs and an estimation of the spatial resolution Δx was acquired for each value of Δt. The values of Δx and their associated uncertainties derived from the fitting procedure are plotted against Δt in Fig.(6.4). A steady improvement in spatial resolution as the time-window is decreased is evident.

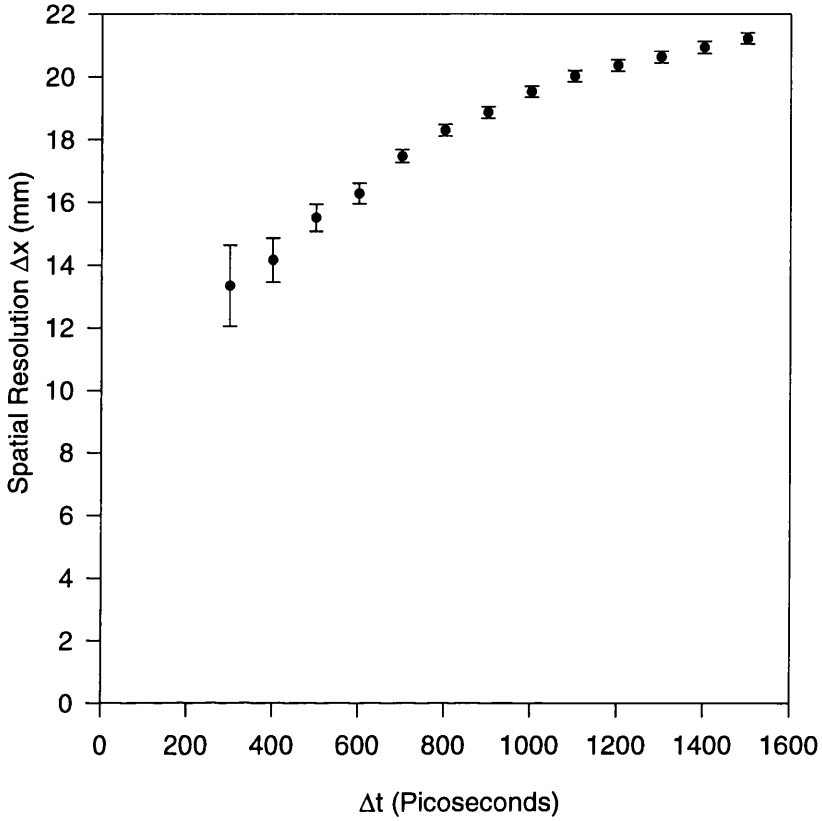

Figure 6.4 *The estimated spatial resolution as a function of time-window derived directly from the corrected TPSFs.*

However, due to insufficient signal for time-windows below 300 ps the spatial resolution appears to be limited to 13 mm. The spatial resolution performance of conventional transillumination can be estimated as Δt tends to infinity, which from Fig.(6.4) would appear to be well over 2 cm. Although time-gating has provided an improvement by roughly a factor of two, a resolution of 13 mm is still below the performance required of a breast imaging system for routine screening.

PCW Model Fits

A further improvement in spatial resolution was attempted using the temporal extrapolation technique. This involved employing the automatic data processing software to fit the PCW model to all of the corrected TPSFs. As mentioned previously, the PCW model is only strictly valid for homogeneous media and the object including an opaque mask is certainly not homogeneous. In order that the PCW model could accurately represent the shape of the early part of the corrected TPSFs it was necessary to let all the parameters vary in the fitting procedure. To decrease sensitivity to noise it is obviously necessary to fit each corrected TPSF over the widest possible time period. However, for PCW model fits generated with time periods greater than approximately one nanosecond, the PCW model was unable to adequately represent the shape of the early part of the corrected TPSFs. This is due to the limits of the PCW model in representing the TPSF of this highly inhomogeneous object. Therefore the PCW model was only fitted to the first nanosecond of each corrected TPSF. Thus, a second set of ERFs were generated as described above, but substituting the PCW model fits in place of the corrected TPSFs. Fig.(6.5) shows the ERF obtained by the PCW model fits for a time-window of 100 ps.

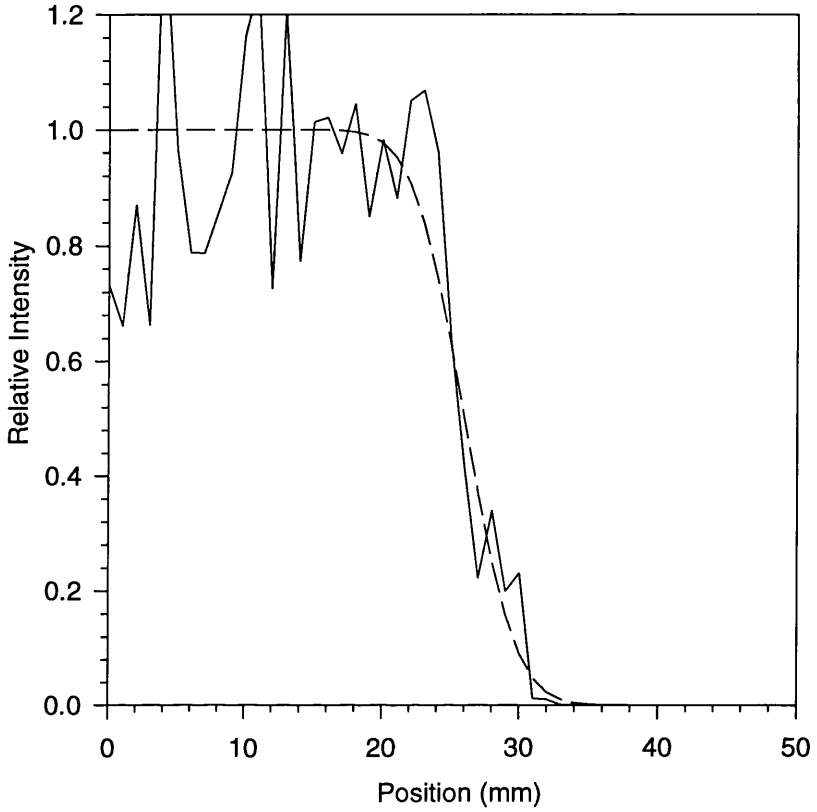

Figure 6.5 *The ERF obtained from the PCW model fits for a time-window of 100 ps (solid line) and its corresponding ERF model fit (dashed line).*

Unlike the ERF generated from the corrected TPSFs, Fig.(6.3), this clearly identifies the edge of the opaque mask. Also shown in Fig.(6.5) is the ERF model generated by fitting the Bentzen model to the ERF which corresponds to a spatial resolution of 8.8 mm. A fairly large uncertainty of ± 3.1 mm was derived from the fitting procedure, which results from the noise in the ERF. As the PCW model fits themselves are noiseless, the fluctuations in the ERF profile must be due to systematic noise or poor photon statistics in the original data. Potential sources of systematic noise which may possibly be eliminated were carefully considered and are described below.

Sources of Systematic Noise

A principal source of systematic noise is due to trigger jitter which, in addition to causing small temporal shifts to the TPSFs (see Sec.(5.2.1), generates a variation in the temporal resolution of the streak camera. This effect is evident in the width variation of reference pulse profiles (ranging from 10 ps to 30 ps for streak time 3) and will certainly introduce a variable broadening to the TPSFs. A possible solution to the problem is deconvolution of each TPSF with its corresponding reference pulse. However, this approach is far from trivial and has not been attempted.

Variability in the ERF intensity could be due to laser power fluctuation during the experiment. This was only measured with a power meter at the beginning and end of the scan, as measurement between each TPSF acquisition is too time-consuming and tedious. Although both these measurements gave a laser power reading of ~ 0.75 W, small fluctuations in the laser power during the scan cannot be ruled out. Unfortunately, such fluctuations may be misinterpreted in the final scan as regions of either high or low transmittance in the object. An initial attempt to normalise all the TPSFs for laser power fluctuations was performed by rescaling their intensities by the area of the corresponding reference pulse. As the reference pulse was recorded directly from the laser, in principal its area should be proportional to the power of the laser. However, due to the errors introduced by trigger jitter and the streak image corrections, the reference pulse area proved to be a poor indicator of variation in laser power. Therefore the laser power was assumed to have remained constant(~ 0.75 W) throughout the scan. A subsequent modification to the imaging system was the introduction of a means of continuously monitoring the laser power throughout an experiment, as discussed in Sec.(6.3.2).

Imprecise temporal alignment of the TPSFs is another potentially significant source of systematic noise. Unfortunately, a realignment of the TPSF on the temporal axis by a few picoseconds can produce a very large change in the integrated intensity for short time-windows. Imprecise temporal alignment can be due to residual error in the correction for the non-linear sweep of the streak camera and by uncertainty involved in the estimation of the centre of the reference pulses. The former error can be assumed

to be already optimised by an accurate calibration of the streak camera. However, the latter can be corrected for by applying small additional temporal shifts, within the uncertainty of the reference pulse centre, to the PCW model fits in order to minimise the random fluctuations in the integrated intensity. This is achieved by first calculating the times, t_1, at which the PCW model fits correspond to a fixed intensity I_1. Second, a profile is generated from the values of t_1 which is then very slightly smoothed. Finally, the difference between the original and smoothed profiles is used to calculate the small temporal shifts which are applied to the PCW model fits. The assumption of smoothness is based on the *a priori* assumption that the sampling interval (1 mm) is well below the expected spatial resolution from the system. If non-linear errors are insignificant then any value of I_1 can be chosen which is common to all PCW model fits. However, if non-linear errors are not negligible, then the smoothing process will preferentially improve an ERF with a time-window corresponding to the approximate time that an intensity of I_1 is reached. In practice, an intensity I_1 is chosen which corresponds to the time-window of the ERF required. This process, which will subsequently be called the *shift-smoothing procedure*, was incorporated into the data processing automation software. The shift-smoothing procedure was performed to the PCW model fits, with t_1 ~ 100 ps, to generate "shift-smoothed PCW model fits" which were used to create a third set of ERFs.

Another source of error worthy of note is that due to finite temporal sampling. The TPSFs are sampled by effectively integrating the detected light over 512 individual small time-windows, with a mean width of approximately 4.5 ps. The mean photon transmission time of each time-window is assumed to be the centre of the window. However, if the gradient of the TPSF changes rapidly within a single time-window then the actual mean transmission time will be slightly shifted from the centre. This error distorts the TPSF on a scale of about half the sampling rate which is approximately 2 ps for streak time 3. Therefore this source of error is assumed to be insignificant compared to other error sources and is ignored.

Shift-smoothed PCW Model Fits

Fig.(6.6) shows the ERF obtained from the shift-smoothed PCW model fits for an integration time of 100 ps. The profile is considerably less noisy than the corresponding ERF obtained from the PCW model fits directly, Fig.(6.5), without any noticeable loss in the edge sharpness.

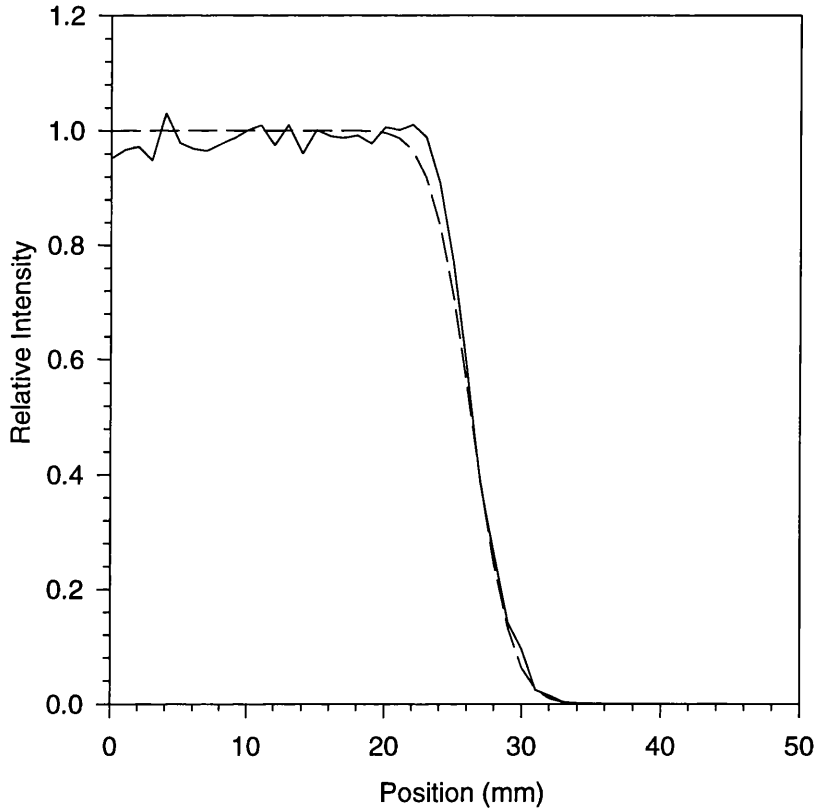

Figure 6.6 *The ERF obtained from the shift-smoothed PCW model fits for a time-window of 100 ps (solid line) and its corresponding ERF model fit (dashed line).*

Also shown in Fig.(6.6) is the appropriate ERF model fit which now corresponds to a spatial resolution of 7.0 mm, with an associated uncertainty of ± 0.6 mm.

The graph shown in Fig.(6.7) shows the spatial resolution, Δx, and their associated uncertainties plotted against the time-window, Δt.

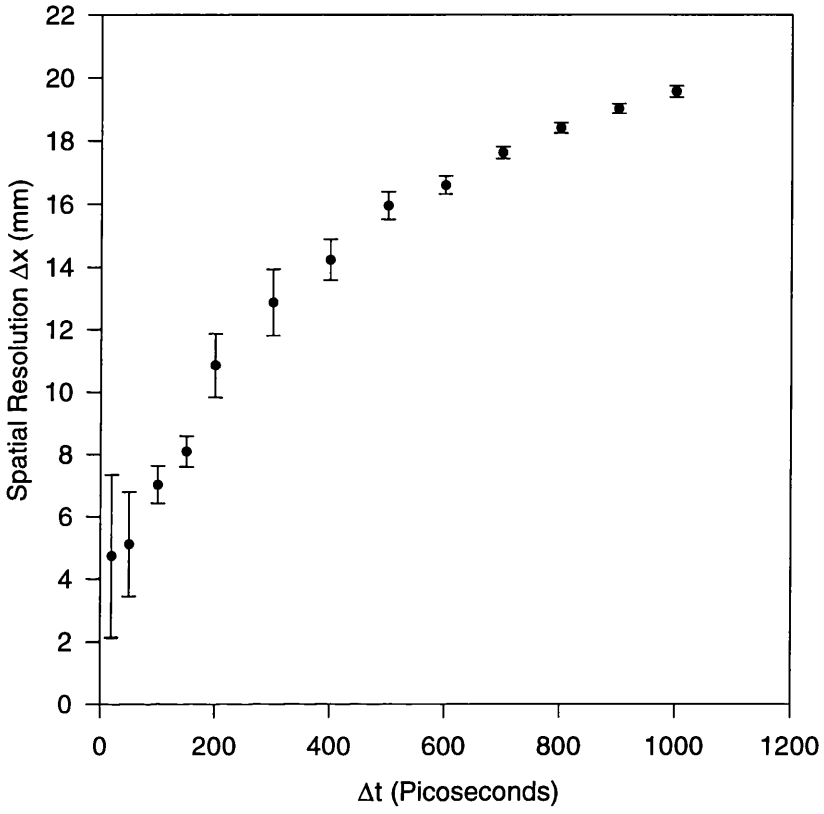

Figure 6.7 *The estimated spatial resolution as a function of time-window derived from the shift-smoothed PCW model fits.*

The improvement in spatial resolution as the time-window decreases is evident again, but now we have achieved sub-centimetre spatial resolution for time-windows less than 200 ps. For time-windows less than 20 ps the ERFs become noisier without any discernable further improvement in spatial resolution. As the value of t_1 was chosen to be approximately 100 ps in the shift smoothing procedure, the uncertainty in the ERF model at 100 ps is a local minimum. Residual non-linearity errors still produce noise in the ERFs for smaller and larger time-windows resulting in larger uncertainties. The uncertainty decreases again at very large time-windows as the sensitivity to the shift-smoothing procedure decreases.

6.1.4 DISCUSSION

The experiment has demonstrated that the temporal extrapolation technique can significantly increase the spatial resolution obtained by the time-gating method, which in this case corresponds to an improvement in spatial resolution from about 13 mm to 5 mm. This result is highly encouraging and suggests that temporal extrapolation may eventually offer adequate spatial resolution for a breast screening modality in the future.

During the data analysis it was possible to improve the ERF for short time-windows by applying the shift-smoothing procedure. This was achieved via the application of *a priori* information. Specifically, it was assumed that the variation in the intensity of the TPSFs as the mask edge was translated across the line of sight should be smooth. However, in a general case, inhomogeneities might exist closer to the object's surface where the spatial resolution would be inherently superior and may be of the order of the sampling interval. In such circumstances, the assumption of smoothness may not necessarily be valid. Nevertheless, it is anticipated that the application of *a priori* information may have a valuable role to play in the development of time resolved imaging as a breast imaging modality.

Although this experiment has demonstrated that temporal extrapolation can be effective, it has yet to be established what factors limit the degree to which spatial resolution can be improved. One would expect, for example, the achievable spatial resolution to be ultimately limited by the finite temporal resolution of this system, since this limits the accuracy with which the TPSFs can be measured. For this experiment no improvement in the spatial resolution was observed for time-windows below about 20 ps, the finite temporal resolution of the streak camera. However, it is unlikely that this technique can always produce a gain in spatial resolution limited only by temporal resolution. It is more likely that the achievable gain in spatial resolution will depend upon the extent to which the TPSFs can be extrapolated with reasonable accuracy. Thus, for a given object, the resolution limit will depend upon the minimum photon flight time at which a measurable flux of photons is obtained, approximately 300 ps for this experiment.

6.2 IMAGING OF A SOLID BREAST PHANTOM

6.2.1 INTRODUCTION

Until recently tissue imaging experiments have been hindered by the lack of suitable tissue-equivalent phantoms. Liquid phantoms, such as that described in Sec.(6.1.), are cumbersome and could not be used for long durations due to the tendency of the scattering particles to settle out of solution. Furthermore, liquid phantoms require containers which can lead to impedance mismatch problems and, moreover, the introduction of well-defined regional variations in the optical properties is difficult to achieve. However, research at UCL by Firbank et al[42,51,132,133] has resulted in a design for the manufacture of inexpensive, stable, solid phantoms with precisely defined regions of absorbing and scattering properties. Such phantoms have enabled experiments to be performed which had previously been impractical using liquid phantoms. The experiment described here[116,128] is probably the first ever attempt to acquire two-dimensional time resolved images of multiple objects inside a solid phantom with physical dimensions and optical properties matched very closely to those of the human breast.

6.2.2 EXPERIMENT

The recipes developed at UCL for the manufacture of solid phantoms have been described extensively elsewhere.[42,51,132,133] The phantom made for the experiment described here was constructed from clear polyester resin in which was suspended titanium dioxide particles. Absorption was introduced by the addition of a small quantity of near infrared dye. The first stage of construction involved making a single solid slab. The concentrations of titanium dioxide and dye were pre-calculated to provide a transport scatter coefficient $\mu_s' = 1.0 \pm 0.1$ mm^{-1} and an absorption coefficient of $\mu_a = 0.01 \pm 0.001$ mm^{-1} at a wavelength of 800 nm. These values are consistent with the range of values obtained from both *in vitro* breast tissue samples and *in vivo* breast measurements, (see Table (2.1)), although the latter generally show somewhat lower absorption coefficients. The final slab had dimensions of 54 mm x 75 mm x 135 mm and a refractive index at 800 nm of 1.56. Secondly, four small, solid cylinders were

made corresponding to various contrasting optical properties. Each cylinder was 5 mm in length and had a diameter of 5.75 mm. These were embedded in the slab by drilling four separate holes, 6 mm wide, in the middle of one face, as illustrated in Fig.(6.8).

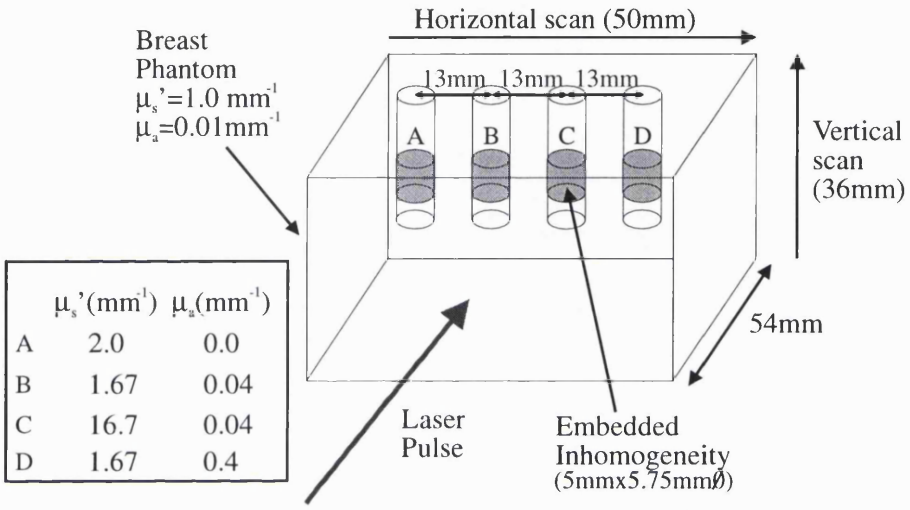

	μs'(mm-1)	μa(mm-1)
A	2.0	0.0
B	1.67	0.04
C	16.7	0.04
D	1.67	0.4

Figure 6.8 *The imaging volume of the breast phantom.*

After depositing each small cylinder in a hole, the space above was filled with cylindrical rods having the same optical properties as the slab. Finally, the remaining space around the cylinders and rods was filled with an epoxy resin, again with the same optical properties as the slab, which held the rods permanently in place. This process was researched and tested very thoroughly on clear transparent blocks of solidified resin until we were sure that it could be performed repeatedly without trapping any air bubbles capable of producing signal artifacts. The absence of bubbles in the completed phantom was confirmed by acquiring suitable x-ray images. Furthermore, a fifth hole,

not shown in the illustration, was drilled in the slab and contained a small cylinder of the same optical properties as the slab. As expected, this cylinder was undetected in a test scan across the phantom and confirmed that there was no contrast due to the cylinder-slab interface. The optical properties of the four small cylinders correspond to relatively large changes in both optical coefficients relative to the surrounding slab. This was due in part to a desire to ensure that the contrast produced by at least two of the cylinders would be high enough to observe any gains in spatial resolution achieved by the imaging technique independent of the SNR. Cylinder B corresponded to a factor of 1.66 increase in scatter and a factor of 4 increase in absorption, while cylinders C and D corresponded to a further order of magnitude increase in scatter and absorption respectively. Finally, cylinder A represents a region of twice the scatter, but zero absorption. These properties were not chosen to correspond to any particular diseased or healthy breast tissues.

The imaging system was used to automatically raster-scan a beam of pulses in 2D, with a wavelength of 800 nm and incident power of ~ 1 watt, in 2 mm steps across the surface of the breast phantom while recording the TPSF at each position. The total area imaged was 18 cm^2, as illustrated in Fig.(6.8), with the centre of the raster-scan aligned to the centre of the phantom. The acquisition parameters used were a fixed accumulation count of 5 and an integration time of 1.5 s. Streak time 4 (corresponding to a full temporal width of 3.6 ns) was used to obtain the majority (60%) of the power in the TPSF. Laser power was measured at the beginning of each imaging row and found to vary throughout the experiment, 1.75 ± 0.05 W. Therefore the TPSFs underwent an image row normalisation which rescaled the intensity of the TPSFs in proportion to the output laser power. This step was incorporated into the data processing software via an "adjustment file" which contained the rescaling intensity coefficients. As with the ERF experiment, described earlier, no account was made for laser power fluctuations within the same imaging row which were assumed to have remained at constant power. Time resolved images were then generated from the corrected TPSFs, PCW model fits, and shift-smoothed TPSFs.

6.2.3 RESULTS

Corrected TPSFs

Images of the breast phantom were generated by numerically integrating the intensity of each corrected TPSF over a specified time-window. Fig.(6.9) shows the image obtained for the time-window of 1750 ps, which corresponds to more than 60% of the power in the TPSFs, and represents the largest integration time we were able to accommodate given the finite temporal range of the data. Note that all the images in this thesis are displayed using a linear grey-scale which is digitized 0-255.

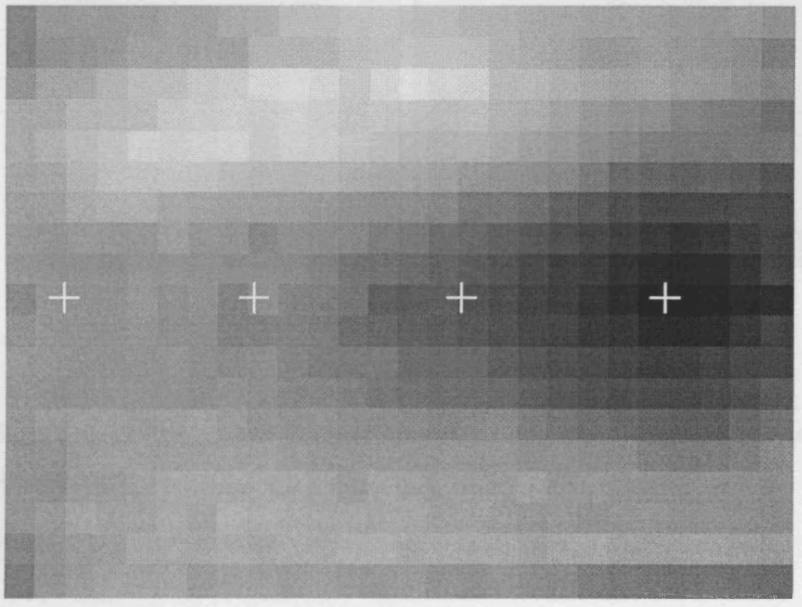

Figure 6.9 *Integrated intensity image generated from the corrected TPSFs for a time-window of 1750 ps. White crosses indicate the centres of the embedded cylinders.*

The image is dominated by the highly absorbing cylinder D. Although there is some contrast also produced by cylinder C, and perhaps A, the spatial resolution is too poor to distinguish them as distinct objects.

Fig.(6.10) shows four images obtained for much smaller integration times of 800 ps, 700 ps, 600 ps, and 500 ps.

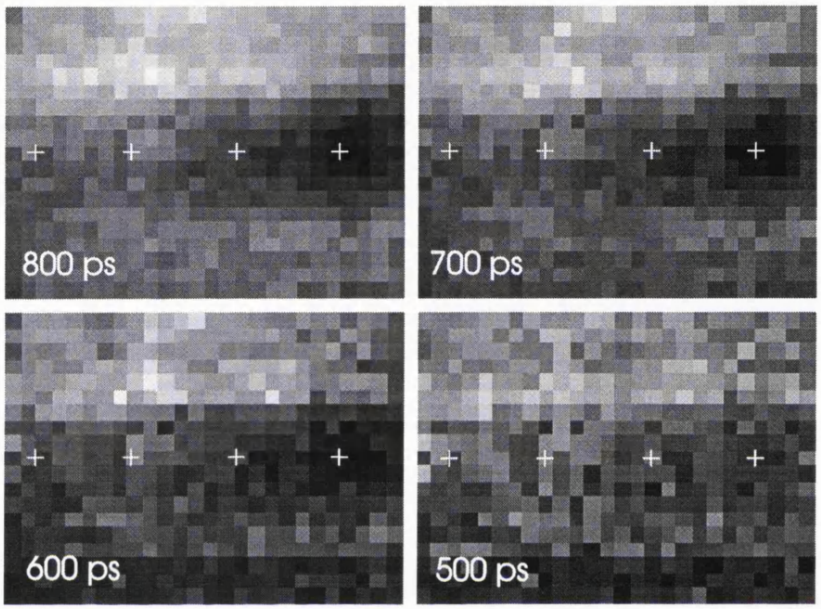

Figure 6.10 *Integrated intensity images generated from the corrected TPSFs for decreasing time-windows.*

This figure illustrates the fundamental problem of time-gated imaging. Decreasing the integration time produces the expected gain in spatial resolution, but at a drastic cost in terms of SNR, as increasing numbers of photons are discarded. As the time-window is reduced from 800 ps to 500 ps we become able to identify cylinders A, C, and D as distinct objects, but the contrast is soon overcome with noise. A time-window of 500 ps represents the minimum below which all the cylinders become unidentifiable.

PCW Model Fits

The automatic data processing software was used to fit the PCW model to all of the corrected TPSFs. Although the breast phantom is not homogenous, provided all the parameters were allowed to vary during the fitting process excellent fits were obtained. For the previous ERF experiment, where the media contained a gross inhomogeneity, excellent fits were also obtained, albeit with values of μ_a and μ_s' which were not particularly meaningful. However, the fits obtained for the data described here, where the inhomogeneities are relatively small and embedded deep within the slab, yielded coefficients which varied little from the known values for the slab ($\mu_a \sim 0.01$ mm^{-1} and $\mu_s' \sim 1.0$ mm^{-1}). Fitting was performed over flight times between zero and 1750 ps, the maximum range of our acquired data. Thereafter images were generated by integrating the PCW model profiles in a manner identical to that employed for the original corrected TPSFs.

Although there was a noticeable improvement in the image quality for time-windows below 700 ps, the images obtained directly from integration of the PCW model profiles still contained noise, particularly of a systematic nature.

Additional Sources of systematic noise

In addition to the sources of systematic noise outlined earlier for the ERF experiment, several other error sources were also identified and are described below.

In the ERF experiment the background Gaussians were manually fitted to each TPSF where the anchor intensity of the Gaussian (see Sec.(5.2.2)) could be optimally chosen by the user. However, for a large number of TPSFs, as in this experiment, this would be far too time-consuming. Therefore the Gaussian subtraction process was automated which required the automatic calculation of the anchor intensity. To reduce the susceptibility to noisy fluctuations in the background signal the anchor intensity was calculated by averaging the TPSF intensity over a small time period (~ 20 ps) centred on the specified anchor time. While this approach appeared to work for the majority of the

TPSFs, the anchor intensities of a few TPSFs (approximately 1%) were still too large or too small due to noise which generated an error in the time resolved images. For TPSFs where such errors became apparent, Gaussians still needed to be fitted manually.

Another source of systematic noise arises from the manner in which the dark correction was performed. Ideally, each TPSF should be individually dark corrected by subtraction of its corresponding dark image. However, the acquisition of a dark image for each TPSF would have substantially increased the experiment duration. Therefore, only one dark image, recorded at the beginning of the experiment, was subtracted from every TPSF. This assumed that the background signal would remain constant throughout the experiment. However, continual exposure of the streak camera creates an after-glow on the phosphor screen which gradually increases the background signal. Furthermore, the after-glow intensity is considered to be a function of the incident intensity on the phosphor screen. In principle, the TPSFs obtained through a homogenous phantom should all be identical and hence any variation due to after-glow can be removed. However, obviously the same approach cannot be applied to TPSFs obtained through an inhomogeneous phantom where the addition of after-glow to each TPSF is unknown. At present, apart from individual dark correction of each TPSF, there is no obvious correction which can be applied to the TPSFs to account for after-glow.

Following the usual corrections to the data, the shift-smoothing procedure was applied in both the image row and image column directions to generate a set of shift-smoothed PCW model fits.

Shift-smoothed PCW Model Fits

Images acquired from the models after performing the shift-smoothing procedure are shown in Fig.(6.11) for time-windows of 500 ps, 400 ps, 300 ps, and 200 ps.

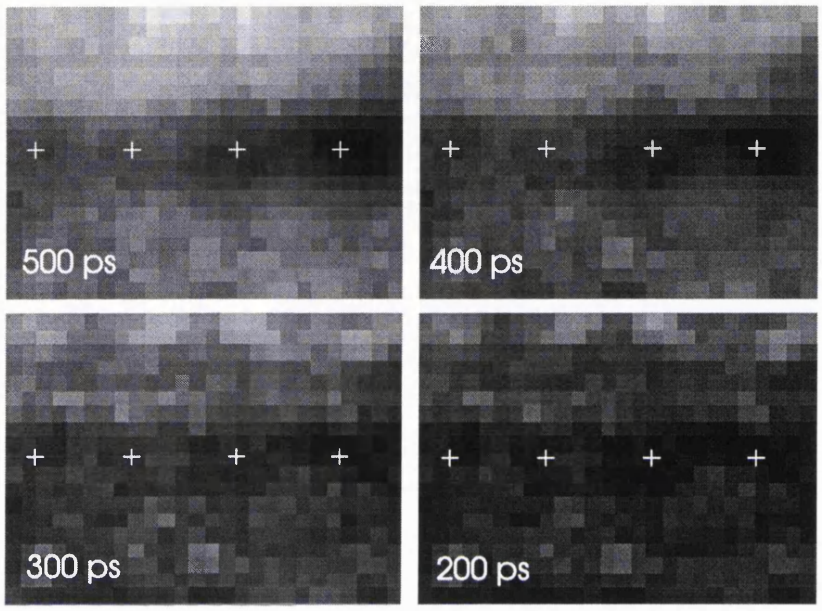

Figure 6.11 *Integrated intensity images generated from the shift-smoothed PCW model fits for decreasing time-windows.*

Although the contrast is low, the SNR for the images corresponding to time-windows of 400 ps and 500 ps is sufficient to reveal all four cylinders. Most encouragingly, cylinder B, which had been indistinct in all the images obtained directly from the corrected TPSFs, can now be identified in all the images. Unfortunately, extrapolation below about 200 ps resulted in images which again became dominated by noise which is considered to be mainly systematic. Although the PCW model profiles are themselves noiseless, the corrections for the various systematic errors are just not sufficient to continue the extrapolation to smaller integration times.

To provide an even clearer indication that all four cylinders have been resolved, the mean of the three centre rows of pixels in each image in Fig.(6.11) are shown in Fig.(6.12).

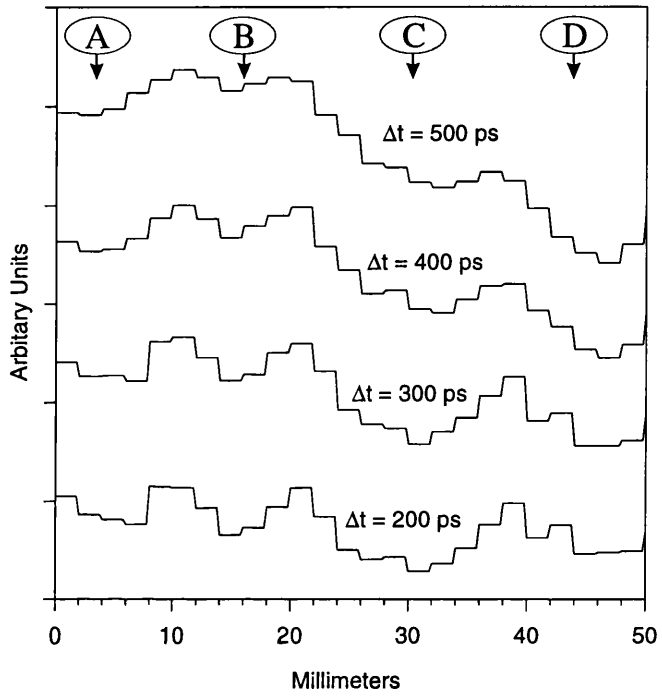

Figure 6.12 *Profiles across the images shown in Fig.(6.11), indicating the presence of the four embedded cylinders.*

Although it is difficult to quantify spatial resolution from this data, the clear delineation between the cylinders in the 200 ps profile suggests that a spatial resolution better than 1 cm has been achieved.

6.2.4 DISCUSSION

Although the experiment described was performed for demonstrative rather than quantitative purposes, the results do provide some useful indications of the performance of the method applied to breast imaging. The visibility of the high contrast cylinders C

and D in Fig.(6.11) and Fig.(6.12) suggests that although a gain in spatial resolution of roughly a factor of two can be obtained in comparison to conventional transillumination, the resolution achievable using straightforward integrated intensity measurements is unlikely to exceed 1 cm for breast imaging. This result is in agreement with previous studies of the probable performance of time resolved imaging methods.[134] This is unlikely to be sufficient for the purposes of screening for breast disease, where it is necessary to detect tumours at an earlier, smaller stage before metastasis occurs and treatment becomes much more difficult. The extrapolation technique, as demonstrated by the results shown in Fig.(6.11) and Fig.(6.12), suggests that resolution can be improved further, and the identification of tumours of a few millimetres in size may yet be possible.

In order to obtain the best PCW model fits to the corrected TPSFs it was necessary to let all the parameters vary in the fitting procedure. As a consequence, the actual fit parameters were not particularly meaningful and images generated from them did not yield useful information. Therefore, although the temporal extrapolation technique can identify regions of varying attenuation it cannot yet indicate whether this is due to changes in absorption or scattering, or a combination of both. However, for breast tumour diagnosis it may be sufficient to rely on attenuation variations and high resolution morphological information.

Detection of small tumours will depend strongly on their optical properties relative to surrounding healthy tissue. The experiment described here did not employ particularly subtle features within our phantom, and further experiments with phantoms incorporating more tumour-like objects were clearly required. Such inhomogeneities also need to be more isolated within the phantoms. It is evident that the appearance of cylinder B in the images in Fig.(6.11) would have been far more dramatic had it not been located in such close proximity to other cylinders of much higher contrast.

While offering some positive encouragement for time resolved techniques as a breast imaging modality, the experiment revealed quite overwhelmingly that imaging a real human breast using a streak camera system is not a realistic proposition. Although the

data collection time of 8 hours can in principle be reduced, the exposure time of 1 hour could not be decreased without compromising the SNR. Furthermore, the average laser power output exceeds the safety limits of NIR radiation exposure to the skin. The maximum permissible exposure[135] (MPE) of NIR radiation to the skin, for durations ranging from 10 seconds to approximately 8 hours, is an average irradiance of 2 $mWmm^{-2}$. In this experiment, using a 3 mm diameter beam, an average irradiance of approximately 140 $mWmm^{-2}$ was used. Therefore, in order for this experiment to satisfy the MPE, the incident photon energy could be spread over a longer time period. Alternatively, one could decrease the average irradiance by effectively increasing the illuminated area, e.g. using a sophisticated flying-spot arrangement. However, for a future clinical system, the possible risks introduced by exceeding the MPE must be weighed against the potential benefits of breast cancer diagnosis.

6.3 EVALUATION OF SPATIAL RESOLUTION AS A FUNCTION OF THICKNESS

6.3.1 INTRODUCTION

The objectives of this study[129] were twofold. The first objective was to experimentally measure the relationship between the spatial resolution achieved using a time-gated technique and the thickness of the object being imaged. It was anticipated that a study of the likely dependence of resolution and SNR on tissue thickness would indicate the merits, if any, of breast compression for a clinical implementation of the method. The second objective was to confirm or otherwise the effectiveness of the temporal extrapolation technique using a series of separate measurements, and observe the range of object thicknesses over which its application has a significant effect.

6.3.2 EXPERIMENT

In order to study the spatial resolution performance of time resolved methods as a function of tissue thickness, a phantom was required which i) contained a sharp opaque boundary from which the ERF could be evaluated, and ii) had an adjustable thickness.

To avoid difficulties associated with having to retain liquids in suitable vessels, it was decided to manufacture a single solid phantom which could be machined to successively smaller thicknesses. The phantom constructed for the experiments described here is illustrated in Fig.(6.13).

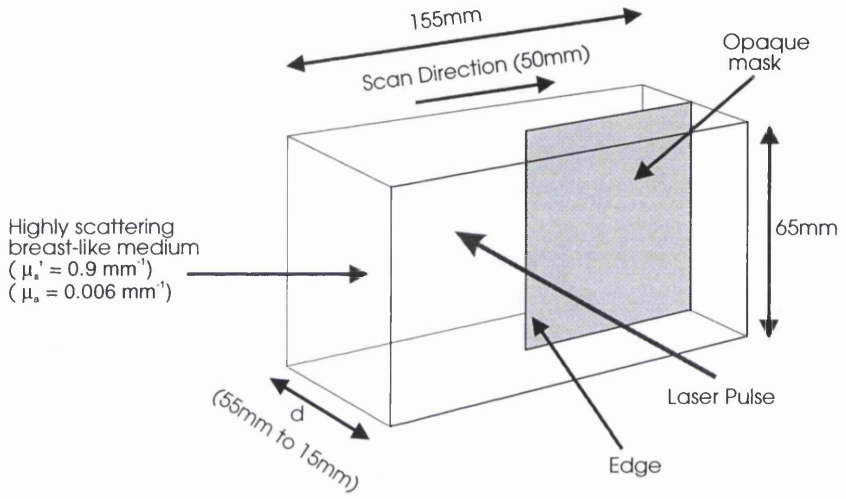

Figure 6.13 *Variable thickness ERF phantom.*

It consists of a rectangular block of polyester resin in which is suspended a uniform distribution of titanium dioxide particles. The concentration of particles provides a transport scatter coefficient μ_s' of about 0.9 mm^{-1} at a wavelength of 800 nm, and a small quantity of NIR dye provides an absorption coefficient μ_a of about 0.006 mm^{-1}. These optical properties fall within the range of reported values for human breast tissues measured *in vivo*, (see Table (2.1)). The refractive index at 800 nm is about 1.56 .

The phantom material was initially cast into a rectangular slab of dimensions 155 mm x 65 mm x 55 mm with a thin rectangular black plastic mask located in the midplane as illustrated in Fig.(6.13). The mask, which had a measured optical density of about six at 800 nm, was positioned parallel to, and halfway between the two largest sides of the

slab, and with the vertical edge located halfway between the two smallest sides. Reduction of the phantom thickness from 55 mm to smaller values was achieved by milling away the two largest surfaces of the phantom by equal amounts so that the opaque mask remained in the midplane. The principal disadvantage of this approach is that, having completed the experiment for a series of thicknesses, the experiment could not be repeated with the same phantom! Nevertheless, because of the time and effort required to manufacture solid phantoms, this method appeared significantly more attractive than having to generate a series of phantoms with different thicknesses. Furthermore, using a single phantom also ensures that the optical properties are always identical for each measurement.

To generate a set of time-dependent edge response functions for each thickness, the system was used to horizontally translate the phantom a distance of 50 mm in 1 mm steps and a TPSF was recorded at each position. Note that for this and later experiments, the Hamamatsu C1587 streak camera was replaced with a brand new Hamamatsu C5680 model. The C5680 had similar streak times to the C1587, but with a more uniform gain across the phosphor screen. The vertical edge of the mask intercepted the optical axis at precisely midway through the 50 mm translation. The time over which the transmitted signal was integrated was varied between 2.5 seconds and 150 seconds consistent with maintaining a reasonably constant SNR. For a given phantom thickness, the integration time increased as the mask moved across the beam, but integration times became smaller as the thickness of the phantom was reduced. The full temporal window recorded by the camera was about 3.2 ns for the larger thicknesses and about 2.2 ns for the smaller thicknesses.

As discussed in Sec.(6.1.3), small fluctuations in laser output power throughout the experiment would distort the ERFs generated from the data. Therefore it was decided to monitor the laser output power continuously throughout the experiment. In order to avoid the tedious and time-consuming procedure of manually inserting a power meter into the main beam between each TPSF acquisition, an additional beam splitter was positioned between the Ti:Sapphire output and the first mirror, (refer to Fig.(5.1)). This enabled a small percentage of the laser output beam to be continuously monitored by

the power meter. The automation software was adapted to include the control of a digital meter, manufactured by Blue Chip Technology, which measured the power meter output voltage, proportional to the laser power. Therefore for each TPSF acquisition the power meter output voltage could be automatically recorded, with negligible increase in the overall experiment time. These voltage values were then used by the data processing software to normalise the TPSFs for variations in laser output power.

The experiment was repeated for seven different thicknesses from 55 mm to 25 mm at 5 mm intervals over a period of one month, and then once more for a thickness of 15 mm. The reason for the later addition of a 15 mm measurement is explained in the next section. Each experiment resulted in a set of 51 TPSFs which were processed in several discrete steps as described in detail in Sec.(6.1.3).

6.3.3 RESULTS

Corrected TPSFs

For each phantom thickness a set of ERFs were obtained directly from the corresponding set of TPSFs in a manner identical to that described in Sec.(6.1.3). This involved numerically integrating the intensity of each TPSF between zero (the time at which an unscattered photon would be detected) and a range of specified integration times. ERFs were generated by displaying the integrated intensity for each integration time, Δt, as a function of the spatial displacement across the edge of the mask. The value of Δt was incremented in 100 ps intervals from 100 ps to 1700 ps, which was the approximate temporal width of the narrowest TPSF. The Bentzen model was then fitted to each ERF to produce an estimate of the width parameter σ and hence the spatial resolution Δx. The values of Δx, and their associated uncertainties derived from the fitting process are plotted against Δt for each phantom thickness in Fig.(6.14).

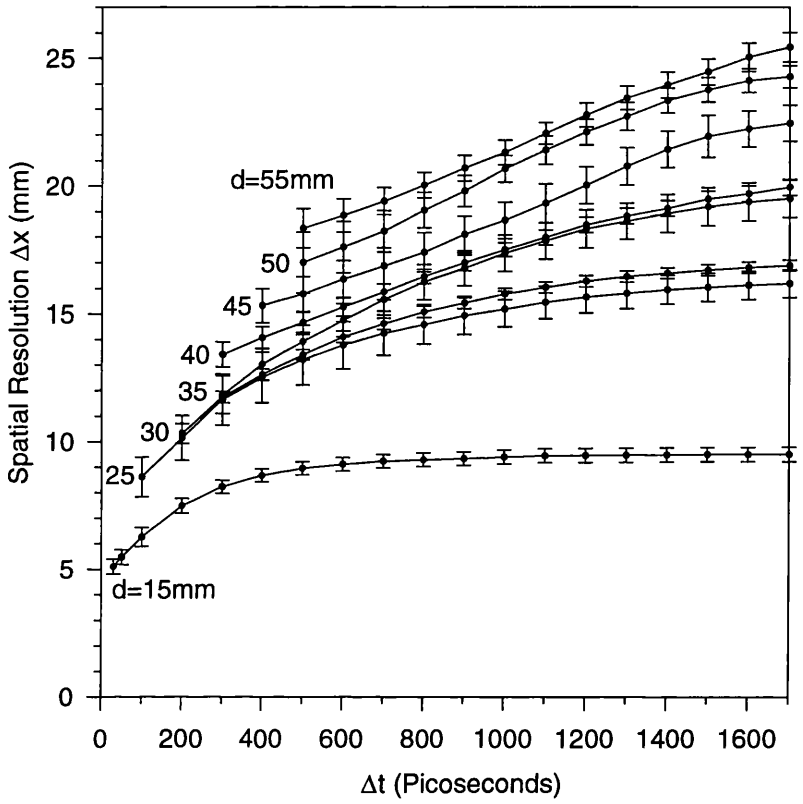

Figure 6.14 *Estimated spatial resolution as a function of time-window derived directly from the corrected TPSFs for all thicknesses.*

In agreement with the previous investigations, Fig.(6.14) confirms that for a given phantom thickness there is a steady improvement in spatial resolution as Δt decreases. Here, however, it is also observed that for a given value of Δt the spatial resolution is worse for larger thicknesses. The spatial resolution Δx is expected to increase with Δt, converging asymptotically towards the value obtained when all the available light is used. The asymptotic value of Δx corresponds to the resolution expected using CW transillumination methods. For smaller thicknesses the resolution obviously reaches the asymptotic value at a shorter integration time because the TPSFs are correspondingly narrower. Although each curve would be expected to converge towards the system response function as Δt decreases, there is a limit below which the integrated intensity becomes too small to evaluate the spatial resolution. Hence the missing data at shorter integration times for larger thicknesses.

PCW Model Fits

The temporal extrapolation method was again explored as a means of evaluating the spatial resolution performance for integration times over which the recorded flux of photons was below the measurable limit. By employing a protocol identical to that used previously, the PCW model was least-squares fitted to each of the TPSFs. Fitting was performed over the first 1500 ps of the data. Although the assumption of homogeneity is clearly unrealistic for this experiment, as it was for the previous ERF experiment, the PCW model was again able to represent the shape of each TPSF very adequately over the fitted range, albeit with fit parameters of μ_a and μ_s' that were not particularly meaningful. Models derived from the fitting procedure were used to generate a second set of ERFs for each phantom thickness in a manner identical to that employed for the original TPSFs. The ERFs were acquired for values of Δt at 50 ps intervals in the range from 50 ps to 500 ps, and at 100 ps intervals from 600 ps to 1700 ps. Spatial resolution Δx was then evaluated for each new ERF using a least-squares fit to the Bentzen model. The values of Δx and their associated uncertainties are plotted against Δt for each phantom thickness in Fig.(6.15). The ability to extend the gain in spatial resolution using temporal extrapolation is clearly demonstrated.

Although the uncertainties in the values obtained for the largest thicknesses and the smallest values of Δt were several millimeters, Fig.(6.15) clearly indicates a convergence of the curves towards a minimum at $\Delta t = 0$. A number of factors dictate the size of the minimum Δx, and the smallest Δt at which that minimum is reached. First, there is the dependence on the spatial extent of the detector and the illuminating beam. Their contribution to the spatial resolution measurement was evaluated empirically by scanning the beam across the edge of an opaque sheet. Since there was no scattering involved, the total integrated intensity was sufficient to acquire an edge response, which yielded a value of Δx equal to about 1.5 mm. Second, the minimum Δx is limited by the inherent inability to define a value of Δt with greater precision than the temporal resolution of the system. If temporal resolution is denoted by δt, then each value of Δt essentially has a corresponding uncertainty of around $\pm\delta t$. Since the number of detected photons rises dramatically with flight time, this uncertainty in Δt will produce an

overestimate of the spatial resolution Δx. However, this effect will only be significant when Δt is of the order of δt, which was estimated to be never worse than 30 ps overall. A third and far less quantifiable factor which limits spatial resolution is the presence of systematic noise in the data. The potentially most serious source of systematic noise is the temporal non-linearity, which is an unfortunate feature of data acquired with a streak camera. Despite attempts to reduce its influence, residual temporal non-linearity certainly produces an additional uncertainty in Δt which is difficult to quantify and which is likely to vary from experiment to experiment.

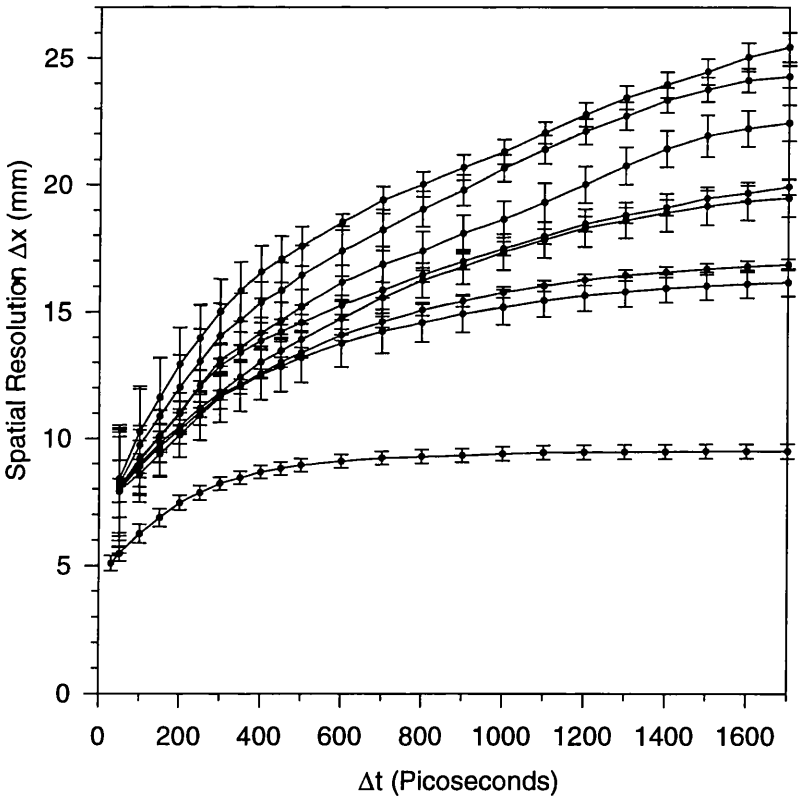

Figure 6.15 *Estimated spatial resolution as a function of time-window derived from the PCW model fits for all thicknesses.*

Finally, another factor which almost certainly influences the minimum spatial resolution as exhibited in Fig.(6.15) is the limited accuracy with which the extrapolation process

is able to predict the true intensity of short flight-time photons. The error in the extrapolated values will naturally be largest when the extrapolation is attempted over a greater interval. It is also important to note that a model based on diffusion theory is an inaccurate predictor of photon behaviour at short flight times, and therefore the extrapolated intensities for Δt less than approximately 100 ps are inherently unreliable. Extrapolation errors may be the cause of the apparent convergence of the extrapolated values in Fig.(6.15) towards a value of around 8 mm at an integration time of 50 ps, which is significantly higher than the limit expected due to other contributing effects.

For phantom thicknesses of 25 mm or larger, there was no measurable flux of photons for integration times less than 100 ps. Thus a further measurement for a thickness of 15 mm was obtained in order to acquire a direct evaluation of the minimum spatial resolution for a value of Δt at or near the inherent temporal resolution of the system. A measurement of the ERF at Δt = 30 ps yielded a spatial resolution of about 5 mm. This provides a reasonable empirical estimate of the minimum spatial resolution achievable with the system when all contributing systematic factors are included, and independent of the extrapolation process. For a linear imaging system, a combination of blurring effects produces a spatial resolution characterized by the geometric mean of the blurring produced by each effect individually. Although the effect of the detector and beam size probably contribute in such a manner to the measured value of Δx, contributions due to uncertainty in Δt or extrapolation errors certainly do not.

Spatial resolution as a function of detected intensity

As has frequently been stressed, the factor which ultimately limits the spatial resolution performance of time-gated imaging is the availability of photons with sufficiently short pathlengths through the object. Although experiments have demonstrated the utility of temporal extrapolation to predict the very small intensities of photons having the shortest pathlengths, the technique can only hope to be effective over a finite range dependent on the SNR of the original data. The rapid decrease in detected intensity as integration time is decreased is illustrated in Fig.(6.16).

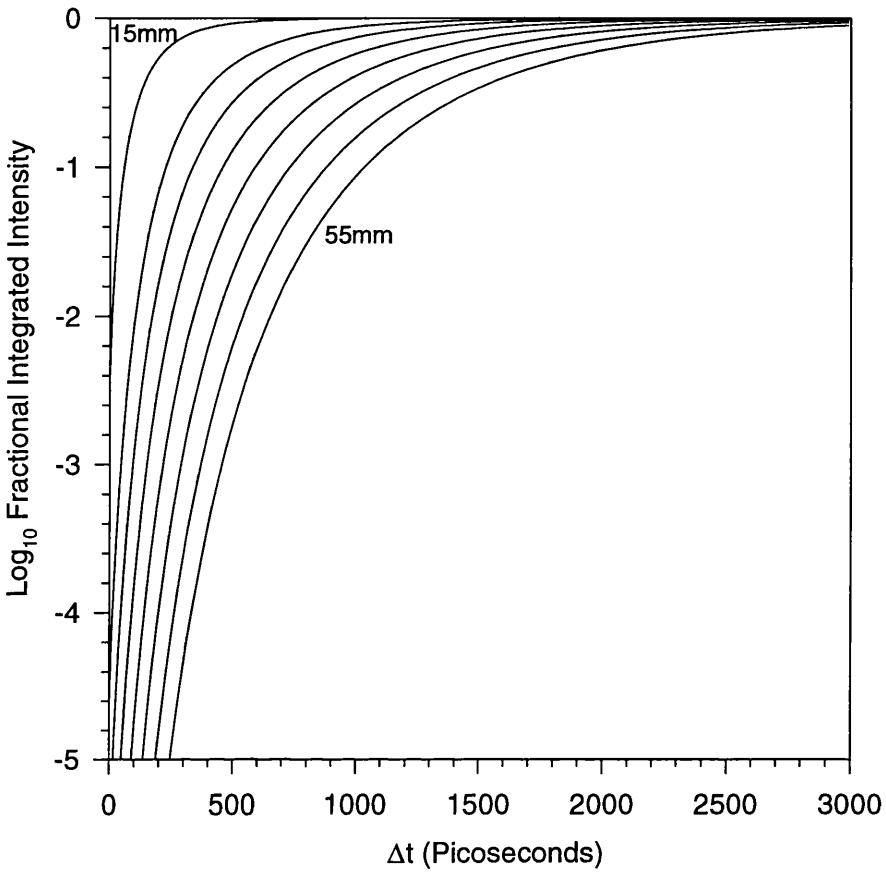

Figure 6.16 *Normalized integrals of the PCW models obtained for homogeneous slabs having the same thicknesses and optical properties as the phantom.*

These curves represent the normalized integrals of diffusion model TPSFs obtained for homogeneous slabs having the same thicknesses and optical properties as the phantom described above, in the absence of the opaque mask. Although, as already mentioned above, a diffusion model becomes increasingly unreliable at shorter photon flight-times (particularly below 100 ps), these curves indicate the enormous difficulty of measuring or estimating the intensity of light at short integration times for thick objects. This difficulty, and the limited effectiveness of temporal extrapolation, can be emphasized further by using the curves in Fig.(6.16) to re-display the spatial resolution measurements shown in Figs.(6.14) and (6.15) as a function of the relative fraction of integrated intensity. This is shown in Fig.(6.17).

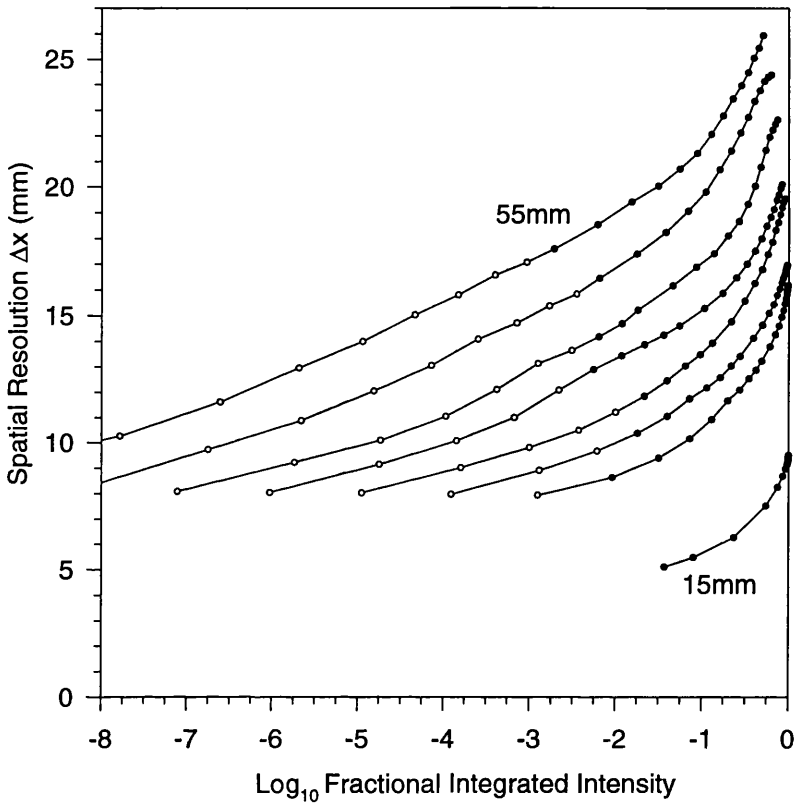

Figure 6.17 *Spatial resolution shown in Figs.(6.14) and (6.15) re-displayed as a function of the relative fraction of integrated intensity obtained from Fig.(6.16).*

Spatial resolution estimates obtained only by extrapolation are indicated using open circles, while estimates obtained directly from the data are indicated using filled circles. Error bars, which would be the same as indicated in Fig.(6.15), are not shown for reasons of clarity. Note that since the integrated intensities were calculated for a homogeneous medium, Fig.(6.17) can be considered representative of the resolution performance for detection of relatively low contrast embedded features (such as a breast) rather than the phantom containing the large opaque mask. The figure indicates, rather discouragingly, that extrapolation over several orders of magnitude in detected intensity is only rewarded by an improvement in spatial resolution of a few millimeters.

6.3.4 DISCUSSION

There have been several recent theoretical and experimental studies of the spatial resolution performance of time resolved imaging technique.[72,99,100,111,115,136-140] Unfortunately comparison of the results of these studies has been hindered by the variety of the definitions for spatial resolution. For example, Mitic et al[136] performed ERF measurements on a 40 mm thick liquid phantom, defining resolution as the base-width of a right-angled triangle fitted to the ERF. A spatial resolution of 12 mm was demonstrated. Studies by de Haller et al[137] involved comparison between time resolved measurements of *in vitro* breast tissue and Monte Carlo simulations. Instead of measuring spatial resolution directly, the researchers defined the ability to visualize small structures in terms of the image quality index (IQI), which is equal to the diameter of the smallest detectable object. IQI depends on all three of the most fundamental image parameters: contrast, spatial resolution, and the SNR. In this case, however, spatial resolution was defined in terms of the spread of light on the surface of a slab illuminated from behind at a single point.

A theoretical relationship between spatial resolution and sample thickness has been explored by several researchers. A diffusion-based analysis by Moon et al[99] suggested that for minimum integration times sufficient to collect light above a detectable threshold, the spatial resolution Δx scales with the thickness d of the sample as $\Delta x \approx 0.2d$. A subsequent study by the same researchers[138] inferred that there can be no improvement upon this diffusion limit of spatial resolution for samples thicker than ~ 35 transport lengths by using arbitrarily short time-gates. However, once again spatial resolution was defined in terms of the photon distribution on the exit surface. A definition of resolution more consistent with that employed here was used by Joblin,[139] who investigated resolution performance in the specific case of an imaging system involving a gating mechanism with a finite contrast, such as the Kerr cell. Spatial resolution was defined as the FWHM of the photon distribution at the midplane of a slab using a confocal geometry. Analysis based on the diffusion equation indicated that for some types of gating mechanism there exists a minimum gating time below which the image resolution is not improved. From a consideration of the minimum detectable

intensity and the finite contrast ratio of a typical Kerr gate mechanism, Joblin deduced that the limiting resolution would be approximately 20% of the medium thickness.

The most comprehensive theoretical examination of spatial resolution of time resolved imaging systems has been conducted by Gandjbakhche et al,[72,100] who employed a model based on random walk theory to calculate the LSF of photons as they cross the midplane of a homogeneous slab of finite thickness. A relationship was derived between the spatial resolution (precisely equivalent to that defined here) and the excess time, t_{xs}, by which a photon is delayed by scattering in reaching the detector. Strong support for the model has been provided by previous comparisons with experimental results obtained for media with two different values of μ_s' but similar thickness.[140] This comparison involved an assumption that t_{xs} could be substituted by Δt, which is reasonable over the earliest region of the TPSF where the detected intensity increases rapidly and most of the detected photons will have flight times at or near $t_{xs} = \Delta t$. A surprising feature of the model is the suggestion that the spatial resolution is independent of medium thickness. However, whatever contributions to the data there may be from detector temporal non-linearity, extrapolation error, and other sources of uncertainty in the resolution measurements, Fig.(6.14) and Fig.(6.15) clearly shows that the spatial resolution achieved at a given Δt has dependence upon the phantom thickness. This appears to be true even at the larger thicknesses and small values of Δt where the approximation of $t_{xs} = \Delta t$ is most valid.

Overall, the implications of this experiment for the likely performance of a breast imaging modality based on time-gating are moderately encouraging. Fig.(6.15) supports previous claims that sub-centimeter spatial resolution is achievable for objects with breast-like properties and thicknesses. It is also important to note that, using a collinear arrangement as employed here, lesions located nearer to either the detector or source will be imaged with superior spatial resolution. Meanwhile the data presented here can also be used to assess any benefit derived from compression of the breast. Published measurements of the effective attenuation coefficient of breast tissue[55,56] suggest that the total intensity transmitted across the breast will increase by about a factor of three for each centimeter of compression. This implies that for a given source and detector

sensitivity, a 1 cm compression allows a further 67% of the available transmitted light to be discarded by reducing Δt without a net loss of signal. Fig.(6.17) indicates that the combination of a 1 cm compression and a factor of three decrease in the fraction of available signal can improve spatial resolution by perhaps as much as 7 mm. Unfortunately part of this gain will be offset by the requirement for shorter exposure times due to the discomfort caused by significant compression. Less encouraging is the implication from Fig.(6.17) that extrapolation over several orders of magnitude in intensity is required to obtain a similar gain in resolution. However, it is feasible that the future employment of models able to predict the behaviour of the shortest pathlength photons with more accuracy may yield higher resolution than that currently achieved using a simple model based on the diffusion approximation.

6.4 EVALUATION OF CONTRAST LIMITS

6.4.1 INTRODUCTION

In the 1980's, several studies by other researchers investigated the potential contrast performance of conventional transillumination methods. Ertefai and Profio[141] applied a one dimensional K-M discrete ordinate analysis to describe light propagation through a three layer model. The transmitted signal was calculated when all three layers were normal breast tissue, i.e. the healthy case, and also when a cancerous breast tissue layer (μ_{eff} = 0.4 mm^{-1}, D = 0.778 mm) was surrounded by two normal layers (μ_{eff}= 0.255mm^{-1}, D = 1.027 mm), i.e. the cancerous case. The contrast due to the introduction of the cancerous layer was defined as the difference in the transmitted signal between the healthy and cancerous case divided by the transmitted signal in the healthy case. For a 5 mm thick cancerous layer, midway within an overall thickness of 35 mm, the contrast was 0.519. As expected, if the cancerous layer was increased to 10 mm thick, and the overall thickness remained constant, the contrast increased to 0.767. However, the ability of the 1D model to represent the physical situation was limited. Navarro and Profio[142] extended the analysis to a 2D discrete ordinate K-M analysis. They concluded that a 5 mm thick tumour would probably not be detected using conventional transillumination methods if located deeper than 5 mm below the tissue surface. Its contrast would be

about ten times smaller than the contrast observed if the same tumour was located at the tissue surface. For surface tumours the contrast was found to decrease by a factor of 3 or 4 when the tumour size was decreased by 50%, although a decrease in the breast thickness from 4 cm to 3 cm had negligible effect on the contrast. This and other CW transillumination studies generally support a rough "rule of thumb" that a breast tumour with a diameter d mm would only be detectable using CW techniques if located within about d mm of the surface.

As discussed previously, these early results demonstrated that conventional transillumination methods were unacceptable for detecting small tumours, embedded deep within the breast. However, quantitative studies of contrast performance using a time resolved methodology are scarce in the published literature.[143,144] Recently, Berg et al[144] investigated, both theoretically and by experiment, the contrast of a 5 mm hole in the middle of a 30 mm thick slab of the highly scattering plastic Delrin ($\mu_s' = 2.3$ mm^{-1} and $\mu_a = 0.002$ mm^{-1}). The contrast of the hole was defined as the signal detected during the first 230 ps when the measurement was on-axis with the hole, divided by the signal detected in the same time-window when the measurement was 15 mm off-axis from the hole. The contrast was measured using their TAC system as the optical properties of the hole were varied by filling it with different solutions of intralipid and dye. The experimental results were shown to be in good agreement with the theoretical predictions from a numerical solution of the diffusion equation, and for various simulated optical properties for the hole ($\mu_a = 0.005$ - 0.1 mm^{-1}, $\mu_s' = 0.2$ - 2.2 mm^{-1}) the contrast was found to vary from 0.5 to 2.2. They also reported that for a given time-gate there are critical combinations of μ_a and μ_s' for the hole, different from the surrounding media, when the contrast is equal to 1. However, they add that this limitation can be overcome by using various time-gates.

It is clear from the solid breast phantom experiment described in Sec.(6.2), that the temporal extrapolation technique is capable of detecting small inhomogeneities within a breast-like phantom. However, this study was of a qualitative, rather than a quantitative, nature and the minimum values of $\Delta\mu_a$ and $\Delta\mu_s'$ that can be detected using time resolved optical imaging methods could not be evaluated. Such limits will be a

critical factor in the detection of small breast tumours in a future clinical breast imaging system. The imaging experiments described below were devised to investigate the limits of the methodology when attempting to detect small absorbing or scattering inhomogeneities of low, but known, contrast embedded in breast-like phantoms.

6.4.2 EXPERIMENT

A pair of contrast phantoms were constructed, one containing scattering inhomogeneities and the other containing absorbing inhomogeneities. The initial stage of the manufacture involved the production of two solid breast-like slabs in a similar manner to that previously described in Sec.(6.2.2). The optical properties of the slabs were $\mu_a = 0.006$ mm^{-1} and $\mu_s' = 0.9$ mm^{-1} and fall within the reported range of values for healthy breast tissue (see Table (2.1)). The slabs had a refractive index of 1.56 at 800 nm and dimensions of 55 mm x 82 mm x 166 mm.

The next stage involved the production of several small, cylindrical, inhomogeneities of various optical properties to be embedded in the slabs. Given the practical limitations of an imaging experiment duration, together with the necessity for the inhomogeneities to be well separated and of reasonable size, it was decided to construct four μ_a inhomogeneities for one phantom and four μ_s' inhomogeneities for the other. It was estimated from previous experiments that inhomogeneities with a factor of 4 increase in either the μ_a or μ_s' compared to the slabs should be detectable, whereas those with a factor of 1.1 increase would probably not be detectable. Therefore the inhomogeneities were manufactured with μ_a or μ_s' 4, 2, 1.5, and 1.1 times greater than the slabs, with dimensions of 5 mm (length) x 5 mm (diameter). In a similar manner to the breast phantom manufacture, described in Sec(6.2.2), four holes of 5.5 mm diameter were drilled in each slab, an inhomogeneity deposited in each hole, and the remaining gaps filled in with exactly the same material as used to manufacture the slabs. Fig.(6.18) indicates the position of the inhomogeneities within both slabs in relation to the volume scanned by the system.

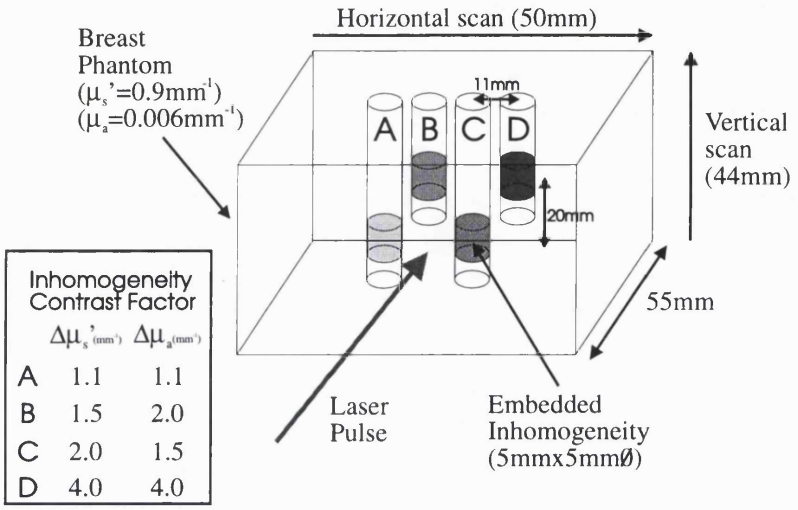

Inhomogeneity Contrast Factor	$\Delta\mu_s'$ (mm^{-1})	$\Delta\mu_a$ (mm^{-1})
A	1.1	1.1
B	1.5	2.0
C	2.0	1.5
D	4.0	4.0

Figure 6.18 *The imaging volume of the absorbing/scattering contrast phantoms.*

The phantoms, known as the "absorbing contrast phantom" and the "scattering contrast phantom" were imaged using the system in separate experiments. As for the previous breast phantom experiment, a beam of pulses was automatically raster-scanned in 2D, at a wavelength of 800 nm and incident power of ~ 1 Watt, in 2 mm steps across the surface of each phantom while recording the TPSF at each position. The total area imaged on each phantom was 22 cm^2, as illustrated in Fig.(6.18), with the centre of the raster-scans corresponding to the centre of each phantom. The acquisition parameters were the same for each experiment, consisting of an accumulation count of 5 and an integration time of 1 second. Streak time 4 (corresponding to a full temporal width of 3.2 ns) was used to obtain the majority of the power in the TPSF. The power meter output voltage was recorded for each TPSF acquisition and used to normalise the TPSFs for variations in laser power throughout the experiment. Time resolved images were generated from the corrected TPSFs and PCW model fits in a similar manner as described previously. However, for these experiments the small differences in the TPSFs due to the embedded inhomogeneities proved to be comparable to or smaller than the uncertainty in the estimation of the background Gaussian component. Therefore, Gaussian subtraction was not performed, which unfortunately limited the ability to accurately estimate short Δt intensities.

6.4.3 RESULTS

Corrected TPSFs - Absorbing Contrast Phantom

Images of the absorbing contrast phantom were generated by numerically integrating the intensity of each corrected TPSF over a specified time-window. Fig.(6.19) shows the image obtained for a time-window of 2500 ps and represents the largest integration time that could be accommodated given the finite temporal range of the data.

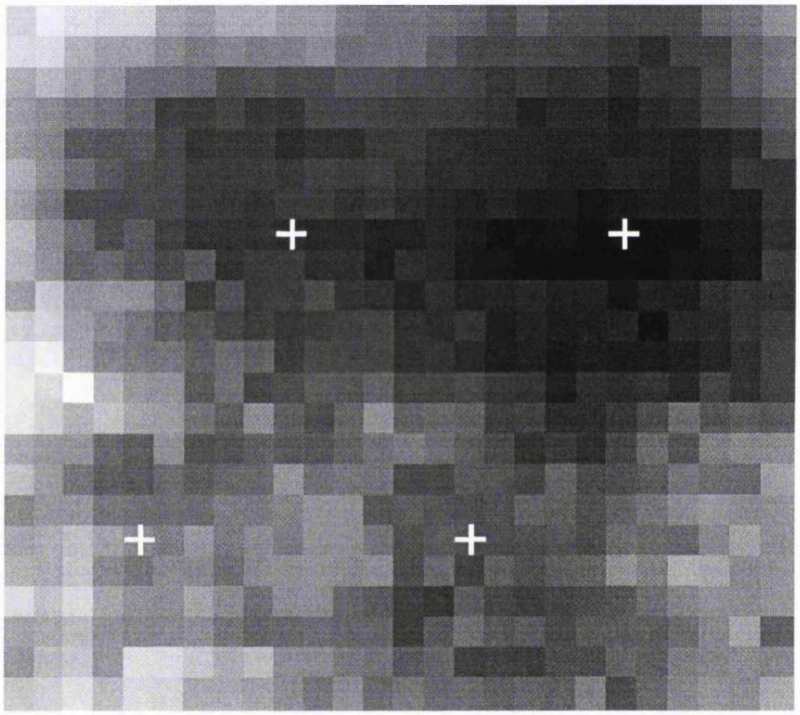

Figure 6.19 *Absorbing contrast phantom time-gated image generated from the corrected TPSFs for Δt = 2500 ps. Expected positions of inhomogeneities marked with white crosses.*

The highest absorbing inhomogeneity, D, can be easily identified in Fig.(6.19), and the ability to detect the other inhomogeneities decreases with the magnitude of their contrast factor. As expected for a time-window of 2500 ps, effectively the same as CW transillumination, the spatial resolution is poor, and probably no better than 2 cm since

the inhomogeneities are ~ 2 cm apart. It is worth commenting that in this and subsequent images the observed positions of the inhomogeneities do not necessarily correspond exactly with their expected positions. Reasons for this discrepancy are discussed later.

Fig.(6.20) shows the time-gated image generated from the corrected TPSFs for a time-window of 1000 ps.

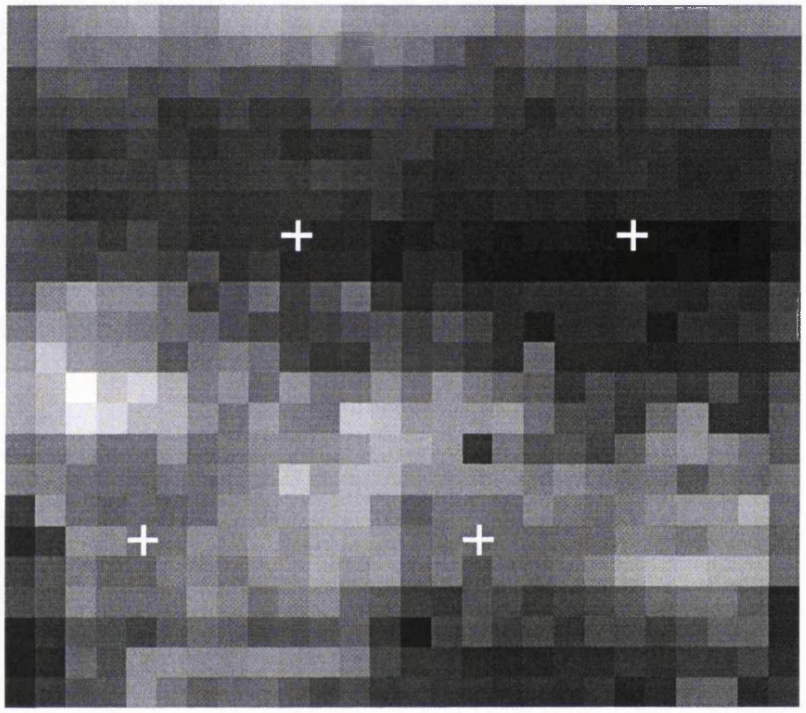

Figure 6.20 *Absorbing contrast phantom time-gated image generated from the corrected TPSFs for Δt = 1000 ps.*

As in Fig.(6.19), inhomogeneities B and D can be identified in Fig.(6.20), with no observable increase in spatial resolution. However, somewhat surprisingly, the contrast is apparently worse, and A and C are barely detectable. Explanations for the apparent decrease in contrast of the absorbing inhomogeneities by time-gating are discussed in Sec.(6.4.4). Unfortunately, even though there is plenty of transmitted light detected for Δt = 1000 ps, the contrast produced by the inhomogeneities becomes overwhelmed by systematic noise for smaller values of Δt.

Corrected TPSFs - Scattering Contrast Phantom

Using the same procedure as described for the absorbing phantom, Fig.(6.21) shows an image of the scattering contrast phantom for a time-window of 2500 ps.

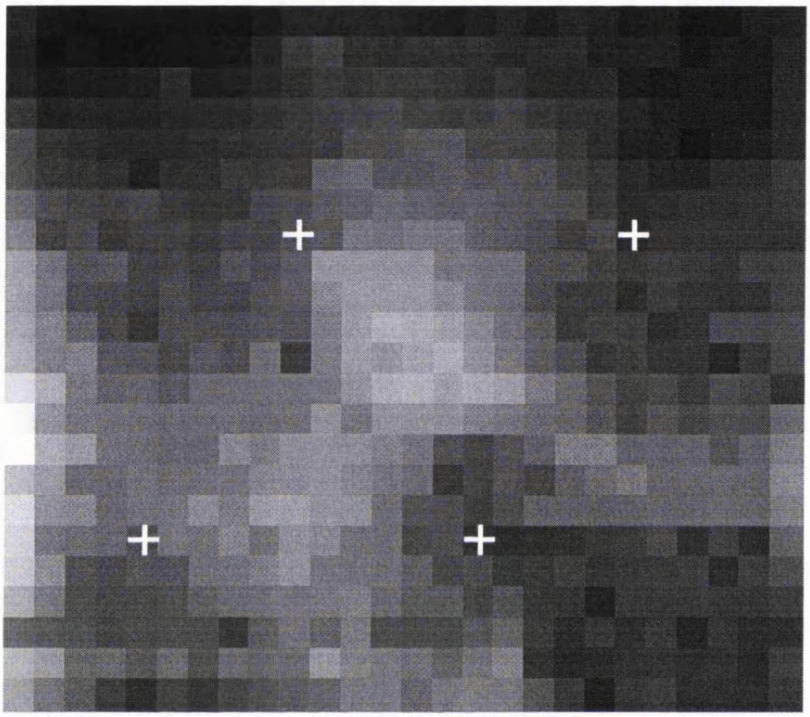

Figure 6.21 *Scattering contrast phantom time-gated image generated from the corrected TPSFs for* Δt *= 2500 ps. Expected positions of inhomogeneities marked with white crosses.*

As for the absorbing contrast phantom, the highest scattering inhomogeneity, D, can be identified in Fig.(6.21), and the ability to detect the other inhomogeneities decreases with the magnitude of their contrast factor. As expected for a time-window of 2500 ps, effectively the same as CW transillumination, the spatial resolution is poor and again probably no better than about 2 cm.

Fig.(6.22) shows the time-gated image generated from the corrected TPSFs for a time-window of 1000 ps.

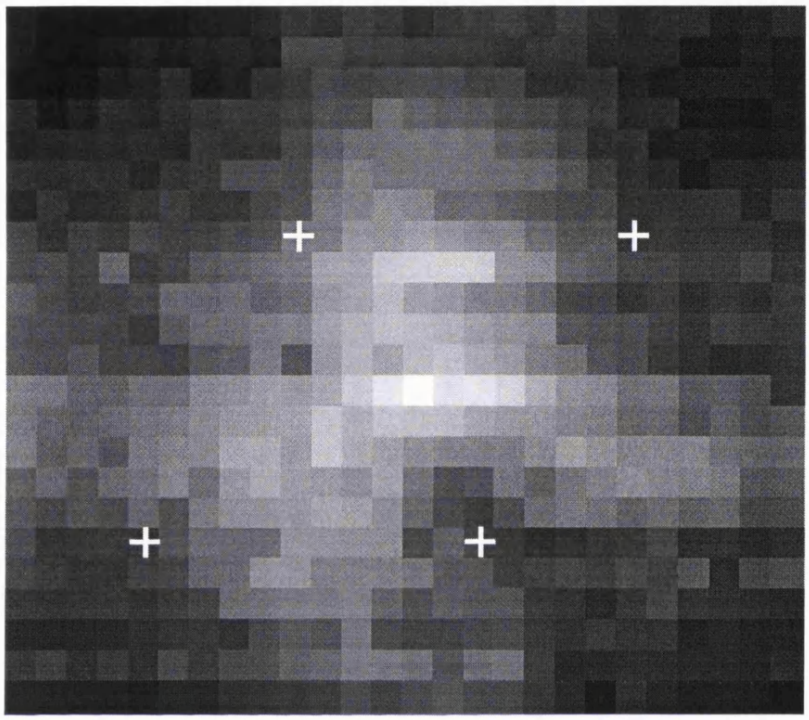

Figure 6.22 *Scattering contrast phantom time-gated image generated from the corrected TPSFs for Δt = 1000 ps.*

As in Fig.(6.21), the ability to identify the inhomogeneities in Fig.(6.22) decreases with the magnitude of their contrast factor, with perhaps a slightly observed increase in spatial resolution and contrast. As before, for Δt less than 1000 ps the images become dominated by systematic noise. A quantitative evaluation of the contrast produced by the inhomogeneities in the previous images is described later.

PCW Model Fits - Absorbing Contrast Phantom

Generating images from PCW model fits to the corrected TPSFs was again explored as a means of improving the images via temporal extrapolation. Unfortunately, the small differences in the TPSFs due to the embedded inhomogeneities proved to be comparable to or smaller than the uncertainty in the estimation of the photon intensity from fitting

the PCW model. Therefore, unfortunately the resulting images did not show any evidence of increased contrast of the inhomogeneities.

PCW Model Fits - Scattering Contrast Phantom

Temporal extrapolation was also attempted on the scattering contrast phantom data. Unlike the absorbing contrast phantom the results were much more encouraging. Fig.(6.23) shows an image of the scattering contrast phantom for a time-window of 300 ps using PCW model fits.

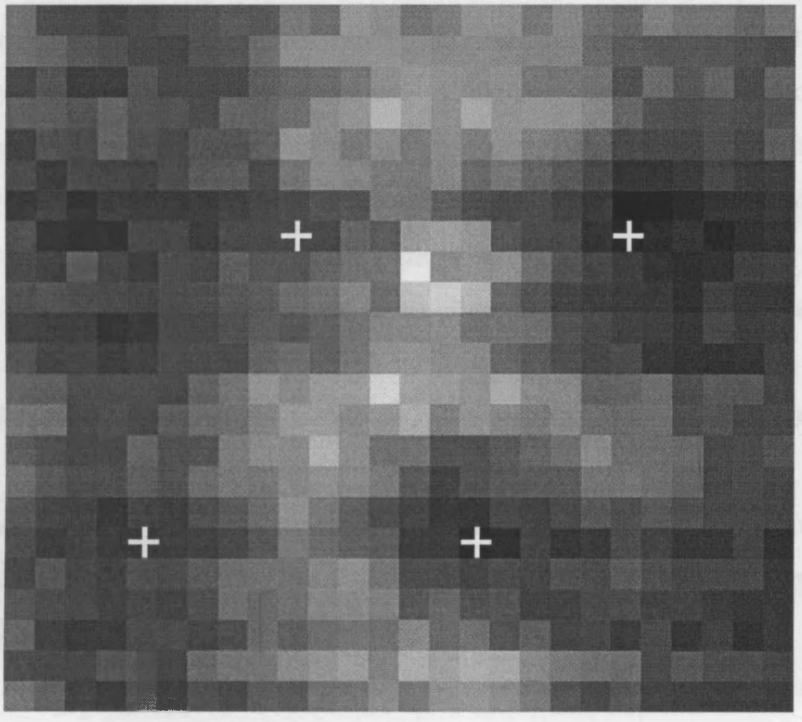

Figure 6.23 *Scattering contrast phantom time-gated image generated from the PCW model fits for Δt = 300 ps.*

Despite the presence of some systematic noise, it is still possible to identify the inhomogeneities in Fig.(6.23) with varying ability. The apparent spatial resolution and contrast are perhaps superior to Fig.(6.22), and again indicates the success of temporal extrapolation. Unfortunately, for Δt less than 300 ps the temporally extrapolated images become totally dominated by systematic noise.

As mentioned earlier, the observed positions of the inhomogeneities in the previous images do not necessarily agree with their expected positions. Although one could argue that this could be due to errors in the actual positioning of the inhomogeneities inside the slabs, it is unlikely to fully account for the discrepancy. Another factor could be the ensemble effect of multiple inhomogeneities. In the ideal ballistic imaging scenario, the observed position of the inhomogeneities should correspond with their expected positions. However, as Δt increases the photons are able to explore more than one inhomogeneity before being detected. Therefore the observed position of an inhomogeneity in the image will be influenced by the presence of the surrounding inhomogeneities. This would explain the difference between the expected and observed positions of the inhomogeneities. Furthermore this effect will certainly be nonlinear with Δt and unfortunately at present there is no obvious correction that can be made.

Evaluation of Inhomogeneity Contrast - Absorbing Contrast Phantom

The contrast produced by each embedded inhomogeneity in the absorbing contrast phantom images was evaluated as follows. First, the image pixel corresponding to the expected centre of the inhomogeneity was identified and indicated by a white cross in the images. The inhomogeneity intensity, I_H, was then calculated as the mean intensity of the nine pixels contained in a 3 x 3 pixel matrix centred on the inhomogeneity. A background region of the image were then identified well away from the inhomogeneities covering an area of 46 pixels. The background intensity, I_B, was calculated as the mean intensity of the pixels contained in the background region. Therefore the % contrast, C, was defined as,[143]

$$C = \left| \frac{I_H - I_B}{I_B} \right| \times 100\ \% \qquad (6.2)$$

An uncertainty value for each estimate of C was derived from the standard deviations of I_H and I_B. Fig.(6.24) shows the contrast evaluated for each inhomogeneity in the time-gated images derived from the corrected TPSFs.

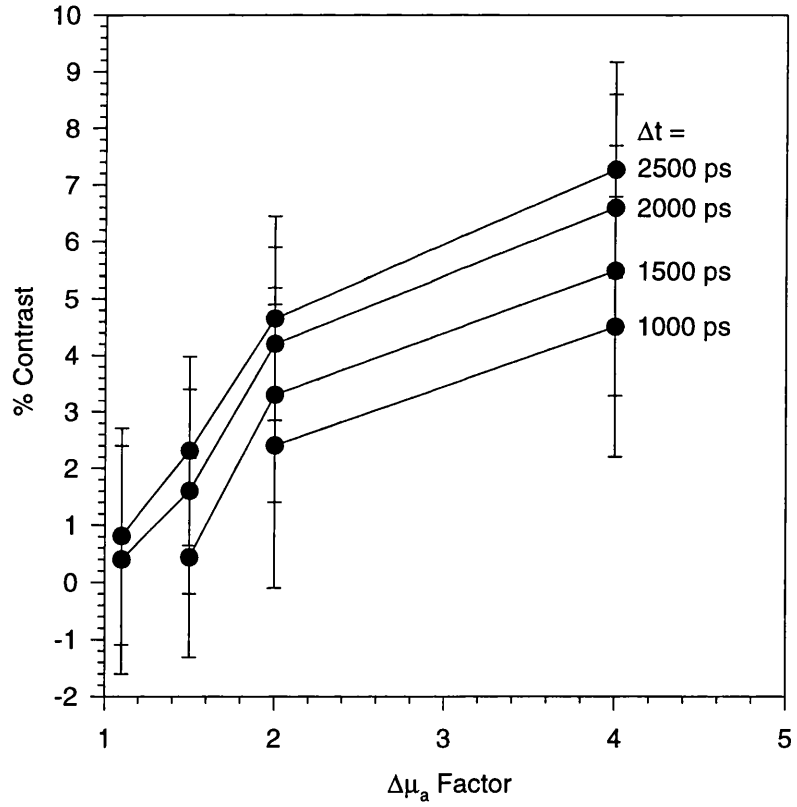

Figure 6.24 $\Delta\mu_a$ *factor versus % contrast evaluated from the time-gated images of the absorbing contrast phantom.*

Fig.(6.24) confirms the earlier suspicion that the % contrast of all the inhomogeneities decreases as Δt *decreases* from 2500 ps to 1000 ps. It is interesting to note that the

absolute decrease in % contrast between 2500 ps and 1000 ps is approximately 3 % for all the inhomogeneities. For Δt of 1500 ps and 1000 ps the error bars for the lower contrast inhomogeneities became extremely large, due to the presence of systematic noise, and hence the missing data points. The data also indicates that the relationship between $\Delta\mu_a$ factor and % contrast is reasonably linear.

Evaluation of Inhomogeneity Contrast - Scattering Contrast Phantom

In an identical manner to that already described for the absorbing contrast phantom, the contrast of each inhomogeneity in the scattering contrast phantom images was evaluated.

Fig.(6.25) shows the contrast of each inhomogeneity in the time-gated images derived from the corrected TPSFs for Δt > 750 ps and the PCW model fits for Δt < 750 ps.

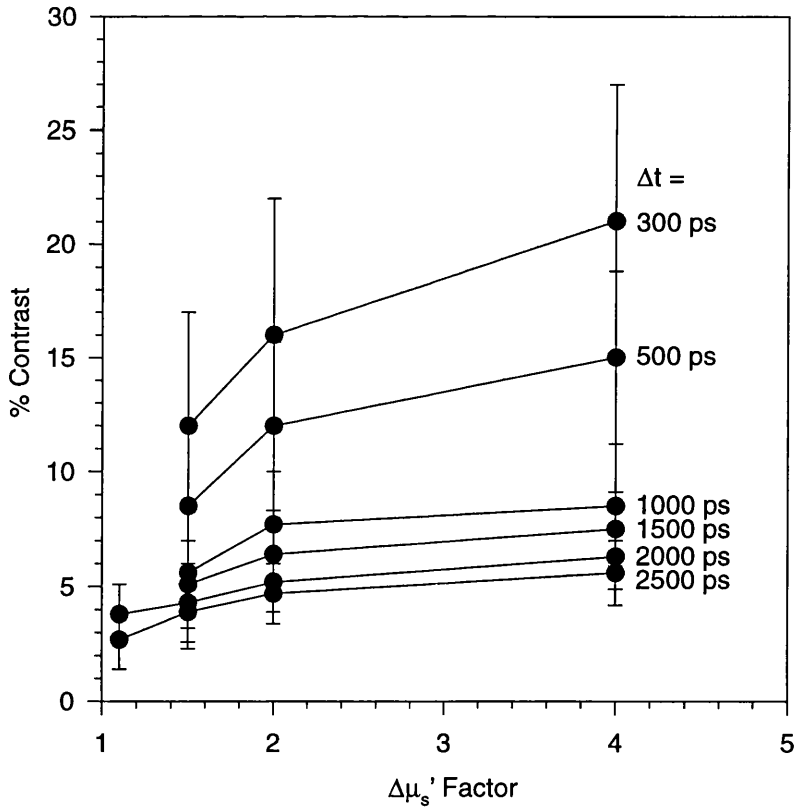

Figure 6.25 $\Delta\mu_s'$ *factor versus % contrast evaluated from the time-gated images of the scattering contrast phantom.*

As expected, Fig.(6.25) confirms the earlier suspicion that the % contrast of all the inhomogeneities *increases* as Δt decreases from 2500 ps to 300 ps. It is worth re-emphasising that this is the opposite trend to that observed for the absorbing contrast phantom. Fig.(6.25) also indicates that the larger the $\Delta\mu_s'$ factor, the greater the gain in % contrast from Δt = 2500 ps to 300 ps. Furthermore the maximum % contrast that can be achieved for of all the inhomogeneities is much larger than the corresponding values achieved for the inhomogeneities in the absorbing contrast phantom. For Δt less than 1500 ps, the error bars for the lowest contrast inhomogeneity became extremely large, due to the presence of systematic noise, and hence the data points have been omitted.

6.4.4 DISCUSSION

One of the surprising conclusions of this study is that time-gating appears to decrease the contrast of a small, absorbing inhomogeneity, embedded in a highly scattering slab, whereas the opposite is true for a scattering inhomogeneity. Unfortunately, at present, there are no other experimental studies reported in the literature with which to compare this observation. However, Hebden and Arridge[145] have theoretically investigated the contrast produced by a point-like inhomogeneity in the midplane of a slab using a model based on diffusion theory, and Gandjbakhche et al[69] have performed a similar analysis using a random walk theory. The model developed by Hebden and Arridge was used to generate a graph, Fig(6.26), of contrast versus Δt for either an absorbing or scattering point-like inhomogeneity embedded in the midplane of a breast-like slab. Strictly, the curve for the scattering inhomogeneity was generated from a perturbation in the diffusion coefficient, rather than μ_s', but the approximation is valid for $\mu_s' >> \mu_a$ as is the case here. The model incorporated the optical properties and geometry of the slab, and assumes that the detector and source are collinear with the inhomogeneity.

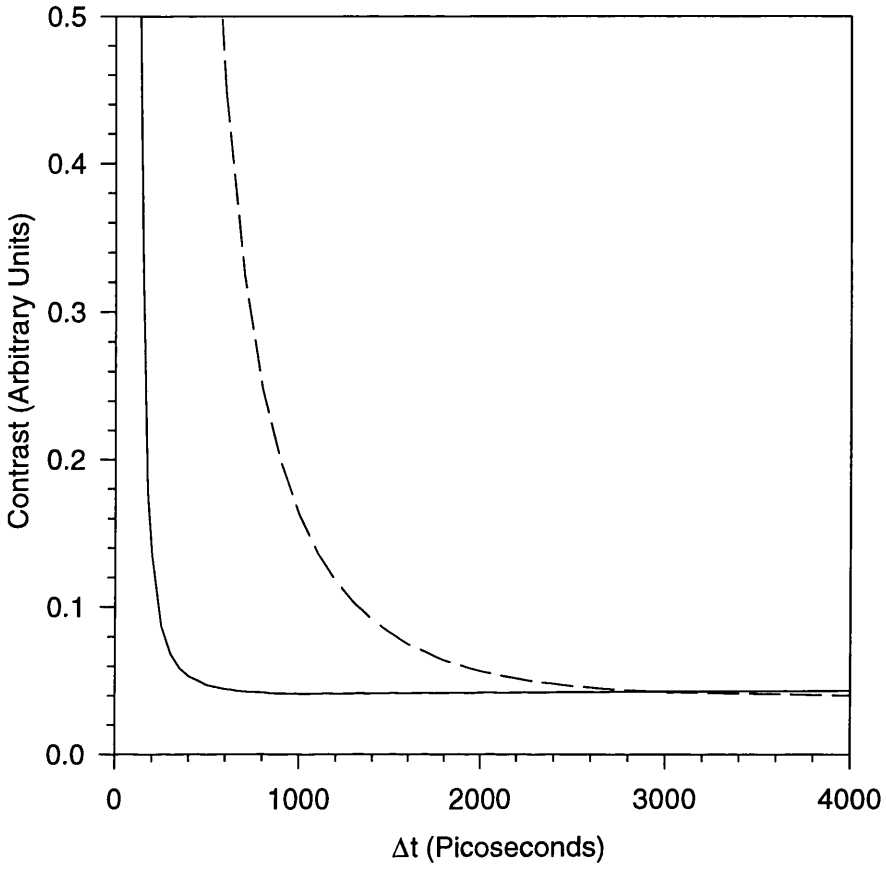

Figure 6.26 *Model predictions of contrast versus Δt for an absorbing inhomogeneity (solid line) and a scattering inhomogeneity (dashed line) embedded midplane in a breast-like slab.*

Fig.(6.26) demonstrates that as the time-window is decreased, the contrast of an absorbing inhomogeneity (solid line) slowly decreases to a minimum at $\Delta t \sim 1000$ ps and then dramatically increases for $\Delta t < 300$ ps. Fig(6.26) also demonstrates that as the time-window is decreased, the contrast of a scattering inhomogeneity (dashed line) always increases and does so dramatically for $\Delta t < 1000$ ps. The experimental results from this study support the predictions of the model. Fig.(6.25) indicates a slow increase in the contrast of the scattering inhomogeneities from $\Delta t = 2500$ ps to 1000 ps, followed by a dramatic increase in the contrast for $\Delta t < 1000$ ps. Fig(6.24) indicates a slow decrease in the contrast of the absorbing inhomogeneities from $\Delta t = 2500$ ps to 1000 ps, below which the data becomes dominated by systematic noise which cannot be

overcome by temporal extrapolation. Therefore, it is not possible to confirm whether there is a rapid increase in the contrast of the absorbing inhomogeneities for $\Delta t < 300$ ps, as predicted by the model.

Although the behaviour of contrast for an inhomogeneity is apparently in accordance with theory, these results can initially seem counter-intuitive. They can perhaps be best explained by considering two effects that influence the contrast of the inhomogeneities as Δt is increased.

The first effect is that the volume sampled by the photons becomes less dominated by the inhomogeneity. This effect will tend to decrease the contrast for both types of inhomogeneity. The second effect is that the photons will have spent longer in the phantom and thus have had more opportunity to interact with the inhomogeneity. Therefore, for an absorbing inhomogeneity more of the photons will become absorbed and tend to increase the contrast. However, for a scattering inhomogeneity, since the photons are already scattered isotropically, the additional scatter cannot make them "more isotropic" and therefore has no effect on the contrast.

Combining the above two effects it can be seen that as Δt is increased the contrast of a scattering inhomogeneity will always decrease. Whereas, for an absorbing inhomogeneity, the first effect initially decreases the contrast, until the second effect becomes dominant and gradually increases the contrast. Since the model assumes point-like inhomogeneities their finite size has been neglected in this analysis and furthermore only a qualitative comparison to the experimental results is valid.

Quantifying the contrast limits of the system is by no means trivial. The results from Fig.(6.25) indicate that for $\Delta t > 2000$ ps the scattering inhomogeneity with a $\Delta\mu_s'$ factor of 1.1 can be separated from the background, including the error, with a % contrast of approximately 3 %. However, for $\Delta t < 2000$ ps, the lowest scattering inhomogeneity that can be separated from background has a $\Delta\mu_s'$ factor of 1.5 with the % contrast increasing to approximately 12 % at 300 ps. Meanwhile, Fig.(6.24) indicate that for $\Delta t > 2000$ ps the absorbing inhomogeneity with a $\Delta\mu_a$ factor of 1.5 can be separated from

background with a % contrast of approximately 2 %. However, for Δt = 1500 ps the lowest absorbing inhomogeneity that can be separated from background has a $\Delta\mu_a$ factor of 2, and a % contrast of approximately 3 %, or for Δt = 1000 ps it is $\Delta\mu_a$ = 2, the % contrast being approximately 2 %. Since the previous studies have demonstrated that the spatial resolution improves with decreasing Δt, as observed here, the problem becomes one of defining the contrast limit for a given spatial resolution. If however, as was found here for the absorbing inhomogeneities, the time-gated images becomes dominated by systematic noise before its contrast begins to increase, a compromise must be found between the inhomogeneity contrast and the spatial resolution.

In practice a clinician would be more concerned with the visualisation of a tumor, which is dependent upon several image parameters, including spatial resolution, contrast and SNR. Visualisation is a large research topic in its own right and outside the scope of this thesis. Whether the values for the achievable contrast presented here are clinically acceptable in terms of visualisation is unclear. It is certainly difficult to justify a claim that in the images, all the inhomogeneities whose contrast can be separated from background can be identified. However, the experiment was designed to investigate the contrast limits and therefore inhomogeneity identification was not intended to be easy. Finally, it must be remembered that the inhomogeneities were not meant to accurately represent any real breast tumour. Current estimates of the optical properties of breast tumours have been limited to *in vitro* measurements (see Table 2.1). The values reported for μ_s' are generally found to be higher than those of healthy breast tissue. The recent study by Troy et al[54] reported one patient with a μ_s' of 1.04 ± 0.2 mm^{-1} for healthy tissue and 1.48 ± 0.2 mm^{-1} for a ductal carcinoma. It is worth noting that these values for μ_s' closely correspond to the values employed for the scattering contrast phantom and its inhomogeneity B. Unfortunately, the reported values for the μ_a of breast tumours fall within the range reported for healthy breast tissue. However, since *in vivo* breast tumours are usually hypervascular, the associated increase in μ_a should improve the contrast.

CHAPTER 7

CONCLUSIONS AND FUTURE WORK

7.1 CONCLUSIONS

This thesis has presented research concerning the development of a near infrared time resolved imaging system, and the assessment of the methodology with a view to its potential as a future breast imaging modality. Overall the research has made valuable contributions to the field of biomedical optics and has resulted in several publications.[3,115,116,128-130] The main results and conclusions of this research are summarised below, followed by a brief discussion of the possible directions for future work.

Chapter 5 discussed the development of the time resolved NIR imaging system employed in the research. It was demonstrated that the automation of the system increased the data acquisition rate by approximately a factor of ten. This enabled the imaging experiments described in Chapter 6 to be performed, which would have been impractical using the previous system due to time constraints. Other important improvements to the system involved linearity correction of the streak camera via calibration experiments and the addition of automatic laser power monitoring. Additionally, computer software was developed throughout the research to apply data processing steps semi-automatically and systematically to the TPSFs in order to produce the final images. The system was also employed by other members of the department to conduct various time resolved experiments. For example, Schweiger et al used the system to image the breast-like phantom, described in Sec.(6.2), using a fanbeam source-detector geometry and an iterative FEM reconstruction algorithm. Hebden and Arridge[146] used the system to collinearly scan across a breast-like phantom containing a small inhomogeneity and investigated the ability of an analytical perturbation model to predict the true displacement of the inhomogeneity from the line of sight. Finally, an M.Sc.

project by Tziraki[147] employed the system to image a breast-like phantom containing a small inhomogeneity using a dual wavelength technique known as TEAM.[148,149]

Chapter 6 described the experimental studies conducted with the system in order to assess the methodology, with a view to its future application to breast imaging. This involved the manufacture of phantoms with optical properties similar to breast tissue, edge-phantoms to evaluate the achievable spatial resolution, and phantoms with several embedded inhomogeneities of differing absorption and scattering properties to evaluate the achievable contrast.

The first experiment performed with the system, Sec.(6.1), was an evaluation of its spatial resolution performance for a breast-like scattering medium.[115] The results indicated that temporal extrapolation has the potential to substantially improve the spatial resolution performance of time-gated imaging. A spatial resolution of ~ 5 mm was achieved using temporal extrapolation, compared to ~ 13 mm for time-gating and > 21 mm for conventional transillumination.

The imaging experiment described in Sec.(6.2) represents the world's first attempt to obtain 2D time resolved images of a solid phantom with breast-like optical properties.[116,128] Images generated using the earliest arriving light substantially improved the identification of embedded inhomogeneities compared to conventional transillumination, although those images corresponding to Δt less than around 700 ps were severely degraded due to a lack of photons. This degradation was partially overcome, while still achieving a significant gain in contrast and spatial resolution, by temporal extrapolation. However, this experiment also confirmed that implementing the technique clinically using a single streak camera would be highly impractical due to the prohibitively long data acquisition times.

An investigation of the relationship between spatial resolution and the phantom thickness was presented in Sec.(6.3).[129] As for the previous experiments, the ability of temporal extrapolation to improve the spatial resolution performance of time-gating was demonstrated. For a given time-gate, an improvement in the spatial resolution was

observed as the phantom thickness was reduced. The results indicated that a breast compression of 1 cm may improve the limiting spatial resolution by as much as 7 mm. Less encouraging was the implication that temporal extrapolation over several orders of magnitude in intensity is required to achieve a comparable improvement in spatial resolution.

Finally, a study was performed, Sec.(6.4), to evaluate the contrast of small inhomogeneities embedded inside a breast-like phantom.[130] This is arguably the most challenging time resolved imaging experiment to date. The very small differences between the optical properties of the inhomogeneities and those of the surrounding medium were close to the expected differences between normal and diseased tissues. The results indicated that small, low contrasting inhomogeneities can be identified. Although temporal extrapolation was able to improve the contrast of the scattering inhomogeneities, the data became dominated by systematic noise for the absorbing inhomogeneities. Furthermore, the results indicated that as the time-window is decreased the contrast of scattering inhomogeneities always increases, whereas the contrast of absorbing inhomogeneities gradually decreases, although the model does predict a rapid increase in contrast at small Δt.

Overall, the research has demonstrated that the time resolved methodology can image small, low contrast inhomogeneities embedded in breast-like phantoms with high spatial resolution (~ 5 mm). The success of temporal extrapolation indicates that it is possible to extract high resolution information from the data by inferring the population of short pathlength photons from longer pathlength photons, even when only a simple diffusion model (PCW) is employed. The implications from the research are highly encouraging with regard to using the time resolved methodology in a future clinical breast imaging system. Indeed, the research contributed to the decision to develop such a system at UCL (see Sec.(7.2)).

7.2 FUTURE WORK

The time resolved imaging methodology requires further research in a number of areas. Although the phantoms employed in this research were generally of a realistic clinical thickness, they were largely unrepresentative of the female breast geometry. Furthermore, the PCW model used in the temporal extrapolation technique assumes a semi-infinite slab geometry which takes no account of edge effects. Therefore it will be necessary to investigate the distortions that edges and different geometries have on the temporal extrapolation technique. Corrections for any distortions will be essential for a future imaging systems using real patients. Similar research is already being pursued by Fantini et al[122] using frequency domain technology.

During the research, the simple PCW model was used for temporal extrapolation and yielded encouraging results. However, as discussed in Sec.(4.3), the PCW model is theoretically inappropriate for accurately representing the transmission of early arriving photons through inhomogeneous media, despite giving reasonable results. Therefore it is worth investigating more sophisticated analytical photon propagation models which could provide superior predictions of early photon behavior for temporal extrapolation.

A future avenue of research is to investigate time resolved imaging at multiple wavelengths. One approach may involve comparing breast images obtained at specific NIR wavelengths which target certain spectral characteristics of breast tumours and may aid their diagnosis.[150] Another possibility is to generate a single image by combining TPSFs acquired at several different wavelengths. This approach may cancel out certain artifacts common at all wavelengths and thereby improve breast tumour diagnosis. Already, a technique known as TEAM[148] (temporal extrapolation absorbance method) has been investigated to produce images from the ratio of TPSFs obtained at two different wavelengths. By assuming that μ_s' is the same at both wavelengths the effects due to photon scatter are effectively cancelled out and images are produced corresponding to the wavelength dependent differences in μ_a. Although the TEAM algorithm is only strictly valid for the trivial case of homogeneous media, some utility for imaging inhomogeneous phantoms has been demonstrated.[147,149]

Currently, a clinical time resolved breast imaging system is being constructed at UCL. This will utilize 32 photon counting detectors, which are considerably less expensive than streak cameras, and a pulsed NIR laser source. The source and detectors will be arranged around the breast and for each source position the TPSF will be simultaneously measured at each detector position. Multiple detector time resolved systems are also known to be under construction by groups at Stanford University[151] (USA) and Hamamatsu Photonics K.K.[152] (Japan). Meanwhile, clinical frequency domain systems have been developed by Carl Zeiss[153] and Siemens AG[150] (Germany), although at present they provide less information than time domain systems due to the limited range of modulation frequencies available.

Information provided from future clinical systems, either time or frequency domain, could be used as input to the iterative reconstruction algorithms described in Sec.(4.2). This approach is showing great promise and current research involves extending the numerical FEM model into complex 3D geometries and including numerous measured quantities into the reconstruction algorithm. One possible measured quantity that has yet to be incorporated is the predicted intensity of early photons obtained from temporal extrapolation.

In the next few years it is expected that there will be a significant increase in clinical breast imaging trials using the latest time and frequency domain NIR imaging systems. If successful they will herald the arrival of a new breast imaging modality, though possibly as a complement rather than as an alternative to x-ray mammography.

REFERENCES

1. B. Chance, ed., "Time-Resolved Spectroscopy and Imaging of Tissues," SPIE **1431** (1991).

2. B. Chance and R. R. Alfano, eds., "Optical Tomography, Photon Migration, and Spectroscopy of Tissue and Model Media: Theory, Human Studies, and Instrumentation," SPIE **2389** (1995).

3. D. J. Hall, "Tissue Imaging with Near Infrared (NIR) Light and its Potential as a Breast Imaging Modality," Surgery (In Press).

4. E. J. Roebuck, "A personal view of the approach to breast cancer screening in the UK," The Breast **3**, 60-68 (1994).

5. G. J. Tortora and N. P. Anagnostakos, "Principles of Anatomy and Physiology," 909-911, Harper Row, New York (1990).

6. L. A. Liotta, "Cancer Cell Invasion and Metastasis," Sci. Am. **266**(2), 34-41 (1992).

7. L. Nystrom, L. E. Rutqvist, S. Wall, A. Lindgren, M. Lindqvist, S. Ryden, I. Andersson, N. Bjurstam, G. Fagerberg, J. Frisell, L. Tabar, and L. Larsson, "Breast cancer screening with mammography: overview of Swedish randomised trials," The Lancet **341**(8851), 973-978 (1993).

8. UK Trial of Early Detection of Breast Cancer Group, "First results on mortality reduction in the UK trial of early detection of breast cancer," The Lancet **2**(8608), 411-416 (1988).

9. UK Trial of Early Detection of Breast Cancer Group, "Breast cancer mortality after 10 years in the UK trial of early detection of breast cancer," The Breast **2**(1), 13-20 (1993).

10. N. Wald, J. Chamberlain, and A. Hackshaw, "Consensus Conference on Breast Cancer Screening," Oncology **51**(4), 380-389 (1994).

11. S. A. Feig, "Radiation Risk from Mammography: Is It Clinically Significant?," AJR **143**(3), 469-475 (1984).

12. E. McCrea, "Clinical Imaging," 205-214, Churchill Livingstone, New York (1988).

13. I. H. Gravelle, "A textbook of Radiology and Imaging (2)," 1359-1373, Churchill Livingstone, Edinburgh (1993).

14. S. A. Fox, D. S. Klos, and C. V. Tsou, "Underuse of screening mammography by family physicians," Radiology **166**, 431-433 (1988).

15. S. E. Harms, D. P. Flamig, K. L. Hesley, M. D. Meiches, R. A. Jensen, W. P. Evans, D. A. Savino, and R. V. Wells, "MR Imaging of the Breast with Rotating Delivery of Excitation Off Resonance: Clinical Experience with Pathologic Correlation," Radiology **187**(2), 493-501 (1993).

16. P. S. Tofts, B. Berkowitz, M. D. Schnall, "Quantitative analysis of Dynamic Gd-DTPA Enhancement in Breast Tumours using a Permeability Model, " MRM **33**(4), 564-568 (1995).

17. U. Hoffmann, G. Brix, M. V. Knopp, T. Heß, and W. J. Lorenz, "Pharmacokinetic Mapping of the Breast: A New Method for Dynamic MR Mammography," MRM **33**(4), 506-514 (1995).

18. K. T. Evans and I. H. Gravelle, "Mammography, Thermography and Ultrasonography in Breast Disease," Butterworth & Co. Ltd., London (1973).

19. W. M. Park and B. L. Reece, "Fundamental Aspects of Medical Thermography," 26-28, The British Institute of Radiology, London (1976).

20. W. Cheong, S. A. Prahl, and A. J. Welch, "A Review of the Optical Properties of Biological Tissues," IEEE J. Quant. Elec. **26**(12), 2166-2185 (1990).

21. M. Cutler, "Transillumination as an aid in the diagnosis of breast lesions," Surgery, Gynecology and Obstetrics **48**(6), 721-729 (1929).

22. A. E. Profio, G. A. Navarro, and O. W. Sartorius, "Scientific basis of breast diaphanography," Med. Phys. **16**(1), 60-65 (1989).

23. F. F. Jobis, "Noninvasive, Infrared Monitoring of Cerebral and Myocardial Oxygen Sufficiency and Circulatory Parameters," Science **198**, 1264-1267 (1977).

24. B. Ohlsson, J. Gundersen, and D. Nilsson, "Diaphanography: a method for evaluation of the female breast," World. J. Surgery **4**, 701-705 (1980).

25. E. Carlsen, "Transillumination light scanning," Diagnostic Imaging **3**, 28-33 (1982).

26. B. Monsees, J. M. Destouet, and D. Gersell, "Light Scan Evaluation of Nonpalpable Breast Lesions," Radiology **163**(2), 467-470 (1987).

27. B. Monsees, J. M. Destouet, and W. G. Totty, "Light Scanning versus Mammography in Breast Cancer Detection," Radiology **163**(2), 463-465 (1987).

28. O. Jarlman, I. Andersson, G. Balldin, and S. A. Larsson, "Diagnostic accuracy of lightscanning and mammography in women with dense breasts," Acta Radiologica **33**(1), 69-71 (1992).

29. O. Jarlman, G. Balldin, I. Andersson, M. Lofgren, S. A. Larsson, and F. Linell, "Relation between lightscanning and histologic and mammographic appearance of malignant breast tumors," Acta Radiologica **33**(1), 63-68 (1992).

30. G. E. Geslien, J. R. Fisher, and C. Delaney, "Transillumination in Breast Cancer Detection: Screening Failures and Potential," AJR **144**(3), 619-622 (1985).

31. P. He, M. Kaneko, M. Takai, K. Baba, Y. Yamashita, and K. Ohta, "Breast Cancer Diagnosis by Laser Transmission Photo-Scanning with Spectro-Analysis (Report 4)," Rad. Med. **8**(1), 1-5 (1990).

32. P. Bouguer, "Essai d'optique sur le gradation de la lumiere, " Paris (1729).

33. P. Bouguer, "Traite d'Optique sur la gradation de la lumiere," Paris (1760), Translated by W.E K. Middelton, "Optical treatise on the gradation of light," Toronto Press, Toronto (1961).

34. F. A. Jenkins and H. E. White, "Fundamentals of Optics," 231 and 457-473, McGraw-Hill, Tokyo (1976).

35. J. H. Lambert, "Photometria, sive de mensura et gradibus luminis, colorum et umbrae," Ausburg (1760).

36. M. S. Patterson, B. C. Wilson, and D. R. Wyman, "The Propagation of Optical Radiation in Tissue I. Models of Radiation Transport and their Application," Lasers in Medical Science **6**, 155-168 (1991).

37. A. Beer, "Bestimmung der Absorption des rothen Lichts in fabrigen Flussigkeiten," Ann. Phys. U. Chem. **86**, 78-88 (1852).

38. S. L. Jacques, "Principles of phase-resolved optical measurements," Future Trends in Biomedical Applications of Lasers, SPIE **1525**, 143-153 (1991).

39. M. Cope, "The development of a near infrared spectroscopy system and its application for non invasive monitoring of cerebral blood and tissue oxygenation in the newborn infant," Ph.D. thesis, University of London, (1991).

40. J. Kaltenbach and M. Kaschke, "Frequency and time-domain modelling of light transport in random media," Medical Optical Tomography: Functional Imaging and Monitoring, SPIE **IS11**, 65-86, Washington (1993).

41. L. G. Henyey and J. L. Greenstein, "Diffuse Radiation in the Galaxy," J. Astrophys. **93**, 70-83 (1941).

42. M. Firbank, M. Hiraoka, and D. T. Delpy, "Development of a stable and reproducible tissue equivalent phantom for use in infrared spectroscopy and imaging," Photon Migration and Imaging in Random Media and Tissues, SPIE **1888**, 264-270 (1993).

43. G. Zaccanti and P. Bruscaglioni, "Method of measuring the phase function of a turbid medium in the small scattering angle range," Appl. Opt. **28**(11), 2156-2164 (1989).

44. C. F. Bohren and D. R. Huffman, "Absorption and Scattering of light by Small Particles," Wiley, New York (1983).

45. D. R. White, E. M. Widdowson, H. Q. Woodard, and J. W. T. Dickerson, "The composition of body tissues (II) Fetus to young adult," British Journal of Radiology **64**(758), 149-159 (1991).

46. G. M. Hale and M. R. Querry, "Optical Constants of Water in the 200nm to 200 μm Wavelength Region," Appl. Opt. **12**(3), 555-563 (1973).

47. J. M. Conway, K. H. Norris, and C. E. Bodwell, "A new approach for the estimation of body composition: infrared interactance," Am. J. Clin. Nutri. **40**, 1123-1130 (1984).

48. M. Cope, D. T. Delpy, "System for long-term measurement of cerebral blood and tissue oxygenation on newborn infants by near infra-red transillumination," Med. Biol. Eng. & Comp. **26**(3), 289-294 (1988).

49. M. Cope, P. van der Zee, M. Essenpreis, S. R. Arridge, and D. T. Delpy, "Data analysis methods for near infrared spectroscopy of tissue: problems in determining the relative cytochrome aa_3 concentration," Time-Resolved Spectroscopy and Imaging of Tissues, SPIE **1431**, 251-262 (1991).

50. D. A. Benaron, D. C. Ho, B. Rubinsky, and M. Shannon, "Imaging (NIRI) and Quantification (NIRS) in Tissue Using Time-Resolved Spectrophotometry: The Impact of Statically and Dynamically Variable Optical Path Lengths," Photon Migration and Imaging in Random Media and Tissues, SPIE **1888**, 10-21 (1993).

51. M. Firbank, "The design, calibration, and usage of a solid scattering and absorbing phantom for near infra red spectroscopy," Ph.D. thesis, University of London, (1994).

52. V. G. Peters, D. R. Wyman, M. S. Patterson, and G. L. Frank, "Optical properties of normal and diseased human breast tissues in the visible and near infrared," Phys. Med. Biol. **35**(9), 1317-1334 (1990).

53. H. Key, E. R. Davies, P. C. Jackson, and P. N. T. Wells, "Optical attenuation characteristics of breast tissues at visible and near-infrared wavelengths," Phys. Med. Biol. **36**(5), 579-590 (1991).

54. T. L. Troy, D. L. Page, and E. M. Sevick-Muraca, "Optical properties of normal and diseased breast tissues: prognosis for optical mammography," J. Biomed.Opt. **1**(3), 342-355 (1996).

55. G. Mitic, J. Kolzer, J. Otto, E. Plies, G. Solkner, and W. Zinth, "Time-gated transillumination of biological tissues and tissuelike phantoms," Appl. Opt. **33**(28), 6699-6710 (1994).

56. K. Suzuki, Y. Yamashita, K. Ohta, and B. Chance, "Quantitative Measurement of Optical Parameters in the Breast Using Time-Resolved Spectroscopy: Phantom and Preliminary In Vivo Results," Investigative Radiology **29**(4), 410-414 (1994).

57. K. Suzuki, Y. Yamashita, K. Ohta, M. Kaneko, M. Yoshida, and B. Chance, "Quantitative measurement of optical parameters in normal breasts using time-resolved spectroscopy: in vivo results of 30 Japanese women," J. Biomed. Opt. **1**(3), 330-334 (1996).

58. P. Kubelka and F. Munk, "Ein Beitrag zur Optik der Farbanstriche," Z. Tech. Phys. **12**, 593-601 (1931).

59. P. Kubelka, "New contributions to the optics of intensely light-scattering materials. Part 1," J. Opt. Soc. Am. **38**(5), 448-457 (1948).

60. P. S. Mudgett and L. W. Richards, "Multiple scattering calculations for technology II," J. Coll. Interface Sci. **39**(3), 551-567 (1972).

61. A. J. Welch, G. Yoon, and M. J. C. van Gemert, "Practical models for light distribution in laser-irradiated tissues," Lasers Surg. Med. **6**, 488-493 (1987).

62. B. C. Wilson and S. L. Jacques, "Optical reflectance and transmittance of tissues: Principles and Applications," IEEE Journal of Quantum electronics **26**(12), 2186-2199 (1990).

63. S. J. Matcher, P. Kirkpatrick, K. Nahid, M. Cope, and D. T. Delpy, "Absolute quantification methods in tissue near infrared spectroscopy," Optical Tomography, Photon Migration, and Spectroscopy of Tissue and Model Media: Theory, Human Studies, and Instrumentation, SPIE **2389**, 486-495 (1995).

64. M. S. Patterson, B. Chance, and B. C. Wilson, "Time resolved reflectance and transmittance for the non-invasive measurement of tissue optical properties," Appl. Opt. **28**(12), 2331-2336 (1989).

65. S. R. Arridge, M. Cope, and D. T. Delpy, "The theoretical basis for the determination of optical pathlengths in tissue: temporal and frequency analysis," Phys. Med. Biol. **37**(7), 1531-1560 (1992).

66. B. W. Pogue and M. S. Patterson, "Frequency-domain optical absorption spectroscopy of finite tissue volumes using diffusion theory," Phys. Med. Biol. **39**(7), 1157-1180 (1994).

67. T. J. Farrell and M. S. Patterson, "A diffusion theory model of spatially resolved, steady-state diffuse reflectance for the noninvasive determination of tissue optical properties in vivo," Med. Phys. **19**(4), 879-888 (1992).

68. S. R. Arridge, "Photon-measurement density functions. Part 1: Analytical forms," Appl. Opt. **34**(31), 7395-7409 (1995).

69. A. H. Gandjbakhche, R. F. Bonner, R. Nossal, and G. H. Weiss, "Absorptivity contrast in transillumination imaging of tissue abnormalities," Appl. Opt. **35**(10), 1767-1774 (1996).

70. S. R. Arridge, M. Schweiger, M. Hiraoka, and D. T. Delpy, "A finite element approach for modeling photon transport in tissue," Med. Phys. **20**(2), 299-309 (1993).

71. A. H. Gandjbakhche, H. Taitelbaum, and G. H. Weiss, "Random Walk analysis of time-resolved transillumination measurements in optical imaging," Physica A **200**, 212-221 (1993).

72. A. H. Gandjbakhche, R. Nossal, and R. F. Bonner, "Theoretical study of resolution limits for time-resolved imaging of human breast," Advances in Laser and Light Spectroscopy to Diagnose Cancer and Other Diseases, SPIE **2135**, 176-185 (1994).

73. J. C. Hebden, S. R. Arridge, and D. T. Delpy, "Optical Imaging in Medicine I: Experimental Techniques," Phys. Med. Biol. (In Press).

74. G. Jarry, S. Ghesquiere, J. M. Maarek, F. Fraysse, S. Debray, B. M. Hung, and D. Laurent, "Imaging mammalian tissues and organs using laser collimated transillumination," J. Biomed. Eng. **6**(1), 70-74 (1984).

75. A. O. Wist, P. P. Fatouros, and S. L. Herr, "Increased Spatial Resolution in Transillumination Using Collimated Light," IEEE Trans. on Med. Imaging **12**(4), 751-757 (1993).

76. P. C. Jackson, P. H. Stevens, J. H. Smith, D. Kear, H. Key, and P. N. T. Wells, "The development of a system for transillumination computed tomography," The British Journal of Radiology **60**(712), 375-380 (1987).

77. M. Kaneko, M. Hatakeyama, P. He, Y. Nakajima, H. Isoda, M. Takai, T. Okawada, M. Asumi, T. Kato, S. Goto, Y. Sugie, T. Hayashi, T. Hayakawa, Y. Yamashita, and K. Ohta, "Construction of a Laser Transmission Photo-Scanner: Pre-Clinical Investigation (Report 2)," Rad. Med. **7**(3), 129-134 (1989).

78. L. Wang, P. P. Ho, and R. R. Alfano, "Time-resolved Fourier spectrum and imaging in highly scattering media," Appl. Opt. **32**(26), 5043-5048 (1993).

79. H. Chen, Y. Chen, D. Dilworth, E. Leith, J. Lopez, and J. Valdmanis, "Two-dimensional imaging through diffusing media using 150-fs gated electronic holography techniques," Opt. Lett. **16**(7), 487-489 (1991).

80. N. H. Abramson and K. G. Spears, "Single pulse-in-flight recording by holography," Appl. Opt. **28**(10), 1834-1841 (1989).

81. K. G. Spears, J. Serafin, N. H. Abramson, X. Zhu, and H. Bjelkhagen, "Chrono-Coherent Imaging for Medicine," IEEE Trans. Bio. Med. **36**, 1210-1221 (1989).

82. A. Rebane and J. Feinberg, "Time-resolved holography," Nature **351**, 378-380 (1991).

83. S. C. W. Hyde, N. P. Barry, R. Jones, J. C. Dainty, P. M. W. French, M. B. Klein, and B. A. Wechsler, "Depth-resolved holographic imaging through scattering media by photorefraction," Opt. Lett. **20**(11), 1331-1333 (1995).

84. J. A. Moon, R. Mahon, M. D. Duncan, and J. Reintjes, "Three-dimensional reflective image reconstruction through a scattering medium based on time-gated Raman amplification," Opt. Lett. **19**(16), 1234-1236 (1994).

85. M. Bashkansky, C. L. Adler, and J. Reintjes, "Coherently amplified Raman polarisation gate for imaging through scattering media," Opt. Lett. **19**(5), 350-352 (1994).

86. J. Reintjes, M. Bashkansky, M. D. Duncan, R. Mahon, L. L. Tankersley, J. A. Moon, C. L. Adler, and J. M. S. Prewitt, "Time-gated imaging with Nonlinear Optical Raman Interactions," Opt. & Phot. News **4**(10), 28-32 (1993).

87. R. Mahon, M. D. Duncan, L. L. Tankersley, and J. Reintjes, "Time-gated imaging through dense scatterers with a Raman amplifier," Appl. Opt. **32**(36), 7425-7433 (1993).

88. M. D. Duncan, R. Mahon, L. L. Tankersley, and J. Reintjes, "Time-gated imaging through scattering media using stimulated Raman amplification," Opt. Lett. **16**(23), 1868-1870 (1991).

89. M. Bashkansky and J. Reintjes, "Imaging through a Strong Scattering Medium Using Nonlinear Optical Field Cross-Correlation Techniques," Opt. Lett. **18**(24), 2132-2134 (1993).

90. S. P. Morgan, M. P. Khong, and M. G. Somekh, "Polarization imaging through scattering media," Photon Propagation in Tissues, SPIE **2626**, 265-272 (1995).

91. J. M. Schmitt, A. H. Gandjbakhche, and R. F. Bonner, "Use of polarized light to discriminate short-path photons in a multiply scattering medium," Appl. Opt. **31**(30), 6535-6546 (1992).

92. P. Bruscaglioni, G. Zaccanti, and Q. Wei, "Transmission of a pulsed polarized light beam through thick turbid media: numerical results," Appl. Opt. **32**(30), 6142-6150 (1993).

93. G. Jarry, O. Schlee, O. Duhamel, J. Virmont, L. Poupinet, B. Clairac, M. Derrien, and D. Yeddou, "Coherent transmission of polarised light through mammalian tissue," Photon Transport in Highly Scattering Tissue, SPIE **2326**, 192-201 (1994).

94. H. Inaba, "Coherent Detection Imaging for Medical Laser Tomography," Medical Optical Tomography: Functional Imaging and Monitoring, SPIE **IS11**, 317-347, Washington (1993).

95. K. Dorschel, B. Messer, O. Minet, and G. Muller, "High resolution coherent tomography," Medical Optical Tomography: Functional Imaging and Monitoring, SPIE **IS11**, 348-354, Washington (1993).

96. M. R. Hee, J. A. Izatt, E. A. Swanson, and J. G. Fujimoto, "Femtosecond transillumination tomography in thick tissues," Opt. Lett. **18**(13), 1107-1109 (1993).

97. J. C. Hebden and R. A. Kruger, "Transillumination imaging performance: Spatial resolution simulation studies," Med. Phys. **17**(1), 41-47 (1990).

98. J. C. Hebden and R. A. Kruger, "Transillumination imaging performance: A time-of-flight imaging system," Med. Phys. **17**(3), 351-356 (1990).

99. J. A. Moon, R. Mahon, M. D. Duncan, and J. Reintjes, "Resolution limits for imaging through turbid media with diffuse light," Opt. Lett. **18**(19), 1591-1593 (1993).

100. A. H. Gandjbakhche, R. Nossal, and R. F. Bonner, "Resolution limits for optical transillumination of abnormalities deeply embedded in tissues," Med. Phys. **21**(2), 185-191 (1994).

101. M. A. Duguay and A. T. Mattick, "Ultrahigh Speed Photography of Picosecond Light Pulses and Echoes," Appl. Opt. **10**(9), 2162-2170 (1971).

102. J. L. Martin, Y. Lecarpentier, A. Antonetti, and G. Grillon, "Picosecond laser stereometry light scattering measurements of biological material," Med. & Bio. Eng. & Comput. **18**, 250-252 (1980).

103. L. Wang, P. P. Ho, C. Liu, G. Zhang, and R. R. Alfano, "Ballistic 2-D Imaging Through Scattering Walls Using an Ultrafast Optical Kerr Gate," Science **253**(5021), 769-771 (1991).

104. L. L. Kalpaxis, L. M. Wang, P. Galland, X. Liang, P. P. Ho, and R. R. Alfano, "Three-dimensional temporal image reconstruction of an object hidden in highly scattering media by time-gated optical tomography," Opt. Lett. **18**(20), 1691-1693 (1993).

105. X. Liang, L. Wang, P. P. Ho, and R. R. Alfano, "Two-dimensional Kerr-Fourier imaging of translucent phantoms in thick turbid media," Appl. Opt. **34**(18), 3463-3467 (1995).

106. R. Berg, O. Jarlman, and S. Svanberg, "Medical transillumination imaging using short-pulse diode lasers," Appl. Opt. **32**(4), 574-579 (1993).

107. S. Andersson-Engels, R. Berg, S. Svanberg, and O. Jarlman, "Time-resolved transillumination for medical diagnostics," Opt. Lett. **15**(21), 1179-1181 (1990).

108. D. A. Benaron and D. K. Stevenson, "Optical Time-of-Flight Absorbance Imaging of Biologic Media," Science **259**, 1463-1466 (1993).

109. D. A. Benaron, J. P. Van Houten, W.-F. Cheong, E. L. Kermit, and R. A. King, "Early clinical results of time-of-flight optical tomography in a neonatal intensive care unit," Optical Tomography, Photon Migration, and Spectroscopy of Tissue and Model Media: Theory, Human Studies, and Instrumentation, SPIE **2389**, 582-596 (1995).

110. J. C. Hebden, "Time-Resolved attenuation of transmitted laser pulses by a homogeneous scattering medium," Opt. Lett. **17**(6), 444-446 (1992).

111. J. C. Hebden, "Evaluating the spatial resolution performance of a time-resolved optical imaging system," Med. Phys. **19**(4), 1081-1087 (1992).

112. J. C. Hebden, R. A. Kruger, and K. S. Wong, "Time Resolved imaging through a highly scattering medium," Appl. Opt. **30**(7), 788-794 (1991).

113. J. C. Hebden, "Time-resolved imaging of opaque and transparent spheres embedded in a highly scattering medium," Appl. Opt. **32**(21), 3837-3841 (1993).

114. J. C. Hebden and K. S. Wong, "Time-resolved optical tomography," Appl. Opt. **32**(4), 372-380 (1993).

115. J. C. Hebden, D. J. Hall, and D. T. Delpy, "The spatial resolution performance of a time-resolved optical imaging system using temporal extrapolation," Med. Phys. **22**(2), 201-208 (1995).

116. J. C. Hebden, D. J. Hall, M. Firbank, and D. T. Delpy, "Time-resolved optical imaging of a solid tissue-equivalent phantom," Appl. Opt. **34**(34), 8038-8047 (1995).

117. J. C. Hebden and D. T. Delpy, "Enhanced time-resolved imaging with a diffusion model of photon transport," Opt. Lett. **19**(5), 311-313 (1994).

118. A. Duncan, T. L. Whitlock, M. Cope, and D. T. Delpy, "A multiwavelength, wideband, intensity modulated optical spectrometer for near infrared spectroscopy and imaging," Photon Migration and Imaging in Random Media and Tissues, SPIE **1888**, 248-257 (1993).

119. M. Maris, E. Gratton, J. Maier, W. Mantulin, and B. Chance, "Functional near-infrared imaging of deoxygenated hemoglobin during exercise of the finger extensor muscles using the frequency-domain technique," Bioimaging **2**, 174-183 (1994).

120. A. Duncan, J. H. Meek, M. Clemence, C. E. Elwell, L. Tyszczuk, M. Cope, and D. T. Delpy, "Optical pathlength measurements on adult head, calf and forearm and the head of the newborn infant using phase resolved optical spectroscopy," Phys. Med. Biol. **40**, 295-304 (1995).

121. E. Gratton, W. M. Mantulin, M. J. vandeVen, J. B. Fishkin, M. B. Maris, and B. Chance, "A novel approach to laser tomography," Bioimaging **1**, 40-46 (1993).

122. S. Fantini, M. A. Franceschini, G. Gaida, E. Gratton, H. Jess, W. M. Mantulin, T. Moesta, P. Schlag, and M. Kaschke, "Frequency-domain optical mammography: edge effect corrections," Med. Phys. **23**(1), 149-157 (1996).

123. M. Schweiger, S. R. Arridge, and D. T. Delpy, "Application of the Finite-Element Method for the Forward and Inverse Models in Optical Tomography," J. Math. Imag. Vis. **3**, 263-283 (1993).

124. M. Schweiger, S. R. Arridge, M. Hiraoka, M. Firbank, and D.T. Delpy, "Comparison of a finite element model with experimental phantom results: application to image reconstruction," Photon Migration and Imaging in Random Media and Tissues, SPIE **1888,** 179-190 (1993).

125. S. R. Arridge and M. Schweiger, "Direct calculation of the moments of the distribution of photon time of flight in tissue with a finite-element method," Appl. Opt. **34**(15), 2683-2687 (1995).

126. S. R. Arridge and M. Schweiger, "The use of Multiple Data Types in Time-Resolved Optical Absorption and Scattering Tomography (TOAST)," Mathematical Methods in Medical Imaging II, SPIE **2035**, 218-229 (1993).

127. S. R. Arridge, M. Hiraoka, and M. Schweiger, "Modelling of Noise Near-Infra Red Transillumination Imaging," Optical Tomography, Photon Migration, and Spectroscopy of Tissue and Model Media: Theory, Human Studies, and Instrumentation, SPIE **2389**, 389-399 (1995).

128. D. J. Hall, J. C. Hebden, and D. T. Delpy, "Time Resolved Imaging of a Solid Breast Phantom," Optical Tomography, Photon Migration, and Spectroscopy of Tissue and Model Media: Theory, Human Studies, and Instrumentation, SPIE **2389**, 182-189 (1995).

129. D. J. Hall, J. C. Hebden, and D. T. Delpy, "Evaluation of spatial resolution as a function of thickness for time resolved optical imaging of highly scattering media, " Med. Phys. (Submitted).

130. D. J. Hall, J. C. Hebden, and D. T. Delpy, "Time resolved optical imaging of very low contrast objects in highly scattering media," (In Preparation).

131. S. M. Bentzen, "Evaluation of the spatial resolution of a CT scanner by direct analysis of the edge response function," Med. Phys. **10**(5), 579-581 (1983).

132. M. Firbank and D. T. Delpy, "A design for a stable and reproducible phantom for use in near infra-red imaging and spectroscopy," Phys. Med. Biol. **38**(6), 847-853 (1993).

133. M. Firbank, M. Oda, and D. T. Delpy, "An improved design for a stable and reproducible phantom material for use in near-infrared spectroscopy and imaging," Phys. Med. Biol. **40**, 955-961 (1995).

134. G. Zaccanti and P. Donelli, "Attenuation of energy in time-gated transillumination imaging: numerical results," Appl. Opt. **33**(30), 7023-7030 (1994).

135. British Standard (BS EN 60825: 1992), "Radiation safety of laser products, equipment, classification, requirement and user's guide".

136. G. Mitic, J. Kolzer, J. Otto, E. Plies, G. Solkner, and W. Zinth, "Time-Resolved transillumination of turbid media," Quantification and Localisation using Diffuse Photons in a Highly Scattering Medium, SPIE **2082**, 26-32 (1994).

137. E. B. de Haller, C. Depeursinge, and C. Y. Genton, "Resolution of time-resolved breast transillumination: in vitro measurements compared with theoretical predictions," Opt. Eng. **34**(7), 2084-2091(1995).

138. J. A. Moon and J. Reintjes, "Image resolution by use of multiply scattered light," Opt. Lett. **19**(8), 521-523 (1994).

139. A. J. Joblin, "Method of calculating the image resolution of a near-infrared time-of-flight tissue-imaging system," Appl. Opt. **35**(4), 752-757 (1996).

140. J. C. Hebden and A. H. Gandjbakhche, "Experimental validation of an elementary formula for estimating spatial resolution for optical transillumination imaging," Med. Phys. **22**(8), 1271-1272 (1995).

141. S. Ertefai and A. E. Profio, "Spectral transmittance and contrast in breast diaphanography," Med. Phys. **12**(4), 393-400 (1985).

142. G. A. Navarro and A. E. Profio, "Contrast in diaphanography of the breast," Med. Phys. **15**(2), 181-187 (1988).

143. J. C. Hebden, "Time resolved image contrast of spheres embedded in highly scattering media," Photon Migration and Imaging in Random Media and Tissues, SPIE **1888**, 22-27 (1993).

144. R. Berg, S. Andersson-Engels, O. Jarlman, and S. Svanberg, "Time-gated viewing studies on tissuelike phantoms," Appl. Opt. **35**(19), 3432-3440 (1996).

145. J. C. Hebden and S. R. Arridge, "Imaging through scattering media using an analytical model of perturbation amplitudes in the time domain," Appl. Opt. (In Press).

146. J. C. Hebden and S. R. Arridge, "Time-Resolved Imaging of Solid Tissue Phantoms Using a Perturbation Model," OSA TOPS on Advances in Optical Imaging and Photon Migration **2**, 93-98 (1996).

147. M. M. Tziraki, "Reconstruction of optical images using the temporally extrapolated absorbance method (TEAM)," M.Sc. report, University of London, (1996).

148. Y. Yamada, Y. Hasegawa, and Y. Yamashita, "Simulation of fan-beam-type optical computed-tomography imaging of strongly scattering and weakly absorbing media," Appl. Opt. **32**(25), 4808-4814 (1993).

149. I. Oda, H. Eda, Y. Tsunazawa, M. Takada, Y. Yamada, G. Nishimura, and M. Tamura, "Optical tomography by the temporally extrapolated absorbance method," Appl. Opt. **35**(1), 169-175 (1996).

150. H. Heusmann, J. Kolzer, J. Otto, R. Puls, T. Freidrich, S. Heywang-Kobrunner, and W. Zinth, "Spectral transillumination of female breasts and breast tissue-like material," Photon Transport in Highly Scattering Tissue, SPIE **2326**, 370-382 (1994).

151. J. P. Van Houten, D. A. Benaron, S. Spilman, and D. K. Stevenson, "Imaging Brain Injury Using Time-Resolved Near Infrared Light Scanning," Pediatr. Res. **39**(3), 470-476 (1996).

152. Y. Yamashita, M. Oda, H. Naruse, and M. Tamaura, "In vivo Measurement of Reduced Scattering and Absorption Coefficients of Living Tissue using Time-Resolved Spectroscopy," OSA TOPS on Advances in Optical Imaging and Photon Migration **2**, 387-390 (1996).

153. H. Jess, H. Erdl, K. T. Moesta, S. Fantini, M. A. Franceschini, E. Gratton, and M. Kaschke, "Intensity Modulated Breast Imaging: Technology and Clinical Pilot Study Results," OSA TOPS on Advances in Optical Imaging and Photon Migration **2**, 126-129 (1996).